Doctor Thesis

Sub-Nanometer Scale Magnetism of Ultra-Thin Manganese Films on Fe(001) studied by means of Spin-Polarized Scanning Tunneling Microscopy/Spectroscopy

Toyo Kazu Yamada

Department of Physics
Gakushuin University
March 2004

Doctor Thesis

Sub-Nanometer Scale Magnetism of Ultra-Thin Manganese Films on Fe(001) studied by means of Spin-Polarized Scanning Tunneling Microscopy/Spectroscopy

Toyo Kazu Yamada

Department of Physics
Gakushuin University

March 2004

FIGURES

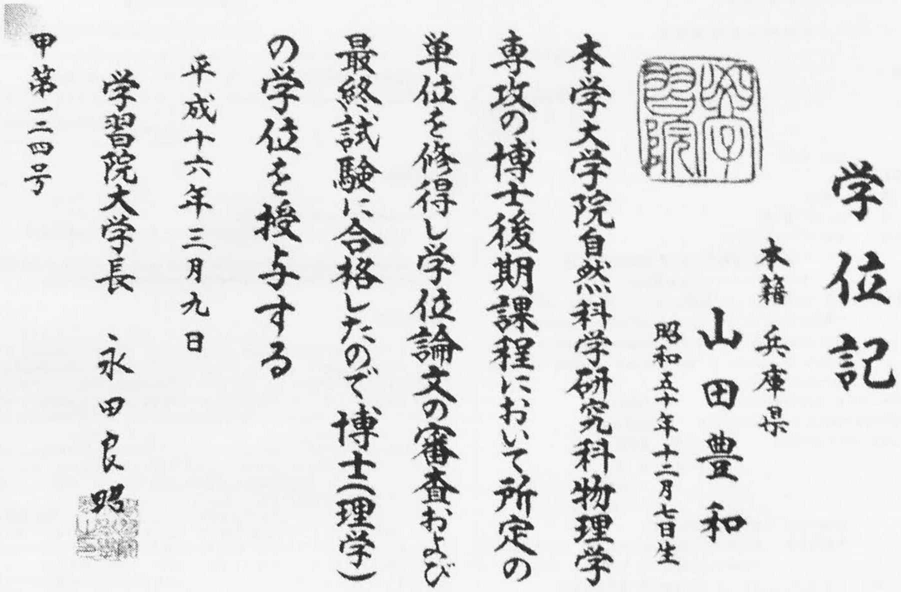

学位記

本籍 兵庫県

山田豊和

昭和五十年十二月七日生

本学大学院自然科学研究科物理学
専攻の博士後期課程において所定の
単位を修得し学位論文の審査および
最終試験に合格したので博士(理学)
の学位を授与する

平成十六年三月九日

学習院大学長 永田良昭

甲第一二四号

FIG. 1.

Name : Toyokazu Yamada
Date of Birth : 07 December 1975

Gakushuin University
Final examination for Ph.D.: 30 January 2004
Supervisor: Prof.Dr. Tadashi Mizoguchi, Faculty of Science, Gakushuin University
Referee: Prof.Dr. Sadamichi Maekawa, Institute for Materials Research, Tohoku University
Referee: Prof.Dr. Ichiro Arakawa, Faculty of Science, Gakushuin University
Referee: Prof.Dr. Takuya Hirano, Faculty of Science, Gakushuin University

Degree: Doctor of Science (Ph.D. in Physics), 09 March 2004

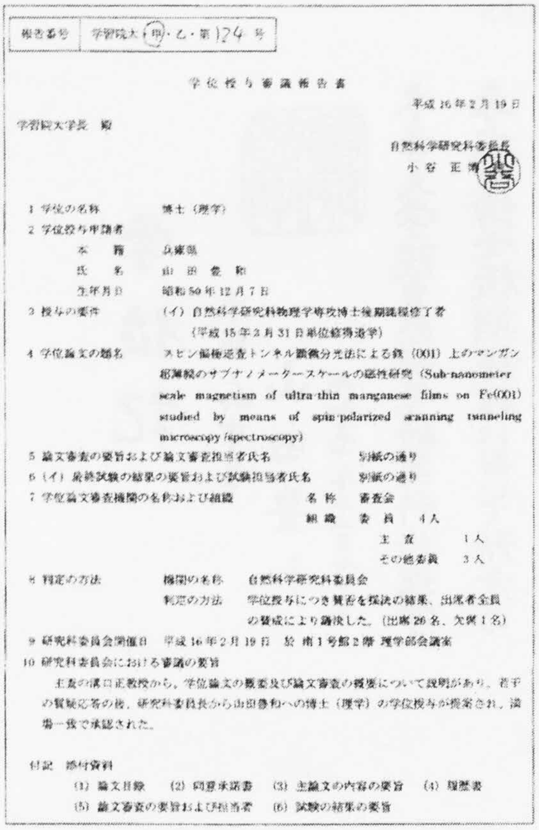

報告番号	学習院大・甲・乙・第 124 号

学位授与審議報告書

平成16年2月19日

学習院大学長 殿

自然科学研究科委員長
小谷 正博

1 学位の名称 博士（理学）
2 学位授与申請者
本籍 兵庫県
氏名 山田豊和
生年月日 昭和50年12月7日
3 授与の要件 （イ）自然科学研究科物理学専攻博士後期課程修了者
（平成15年3月31日単位修得退学）
4 学位論文の題名 スピン偏極走査トンネル顕微分光法による鉄（001）上のマンガン超薄膜のサブナノメータースケールの磁性研究（Sub-nanometer scale magnetism of ultra-thin manganese films on Fe(001) studied by means of spin-polarized scanning tunneling microscopy/spectroscopy）
5 論文審査の要旨および論文審査担当者氏名 別紙の通り
6（イ）最終試験の結果の要旨および試験担当者氏名 別紙の通り
7 学位論文審査機関の名称および組織 名称 審査会
組織 委員 4人
主査 1人
その他委員 3人
8 判定の方法 機関の名称 自然科学研究科委員会
判定の方法 学位授与につき賛否を採決の結果、出席者全員の賛成により議決した。（出席26名、欠席1名）
9 研究科委員会開催日 平成16年2月19日 於 南1号館2階 理学部会議室
10 研究科委員会における審議の要旨

主査の溝口正教授から、学位論文の概要及び論文審査の概要について説明があり、若干の質疑応答の後、研究科委員長から山田豊和への博士（理学）の学位授与が提案され、満場一致で承認された。

付記 添付資料
（1）論文目録 （2）同意承諾書 （3）主論文の内容の要旨 （4）履歴書
（5）論文審査の要旨および担当者 （6）試験の結果の要旨

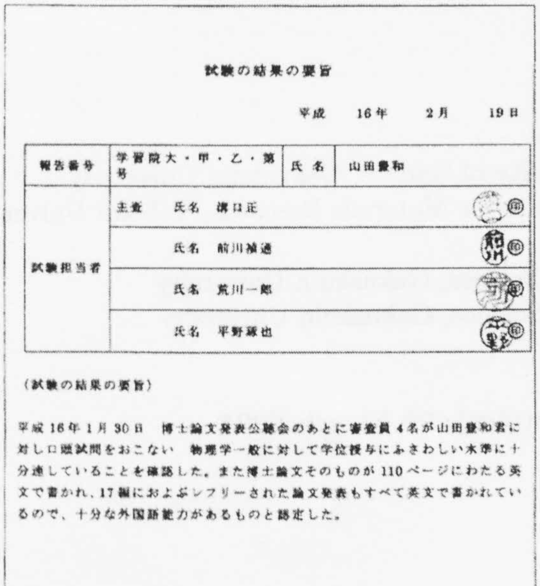

試験の結果の要旨

平成 16年 2月 19日

報告番号	学習院大・甲・乙・第 号	氏名	山田豊和
試験担当者	主査 氏名 溝口正 ㊞		
	氏名 前川禎通 ㊞		
	氏名 荒川一郎 ㊞		
	氏名 平野琢也 ㊞		

（試験の結果の要旨）

平成16年1月30日 博士論文発表公聴会のあとに審査員4名が山田豊和君に対し口頭試問をおこない 物理学一般に対して学位授与にふさわしい水準に十分達していることを確認した。また博士論文そのものが110ページにわたる英文で書かれ、17編におよぶレフリーされた論文発表もすべて英文で書かれているので、十分な外国語能力があるものと認定した。

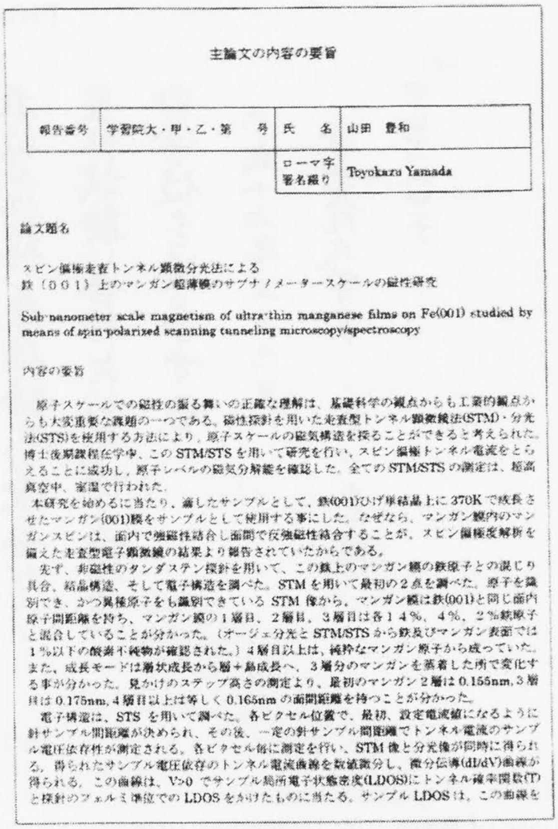

主論文の内容の要旨

報告番号	学習院大・甲・乙・第 号	氏名	山田 豊和
		ローマ字署名綴り	Toyokazu Yamada

論文題名

スピン偏極走査トンネル顕微分光法による
鉄（００１）上のマンガン超薄膜のサブナノメータースケールの磁性研究

Sub-nanometer scale magnetism of ultra-thin manganese films on Fe(001) studied by means of spin-polarized scanning tunneling microscopy/spectroscopy

内容の要旨

原子スケールでの磁性の振る舞いの正確な理解は、基礎科学の観点からも工業的観点からも大変重要な課題の一つである。磁性探針を用いた走査型トンネル顕微鏡法(STM)・分光法(STS)を採用する方法により、原子スケールの磁気構造を探ることができると考えられた。博士後期課程在学中、この STM/STS を用いて研究を行い、スピン偏極トンネル電流をとらえることに成功し、原子レベルの磁気分解能を確認した。全ての STM/STS の測定は、超高真空中、室温で行われた。

本研究を始めるに当たり、適したサンプルとして、鉄(001)ひげ単結晶上に 370K で成長させたマンガン(001)膜をサンプルとして使用する事にした。なぜなら、マンガン膜内のマンガンスピンは、面内で強磁性結合し面間で反強磁性結合することが、スピン偏極度解析を備えた走査型電子顕微鏡の結果より報告されていたからである。

先ず、非磁性のタングステン探針を用いて、この鉄上のマンガン膜の鉄原子との混じり具合、結晶構造、そして電子構造を調べた。STM を用いて最初の２点を調べた。原子を識別でき、かつ異種原子をも識別できている STM 像から、マンガン膜は鉄(001)と同じ面内原子間距離を持ち、マンガン膜の１層目、２層目、３層目は各１４％、４％、２％鉄原子と混合していることが分かった。（オージェ分光と STM/STS から鉄及びマンガン表面では１％以下の酸素不純物が確認された。）４層目以上は、純粋なマンガン原子から成っていた。また、成長モードは層状成長から層＋島成長へ、３層分のマンガンを蒸着した所で変化する事が分かった。見かけのステップ高さの測定より、最初のマンガン２層は 0.155nm, 3 層目は 0.175nm, 4 層目以上は等しく 0.165nm の面間距離を持つことが分かった。

電子構造は、STS を用いて調べた。各ピクセル位置で、最初、設定電流値になるように針サンプル間距離が決められ、その後、一定の針サンプル間距離でトンネル電流のサンプル電圧依存性が測定される。各ピクセル毎に測定を行い、STM 像と分光像が同時に得られる。得られたサンプル電圧依存のトンネル電流曲線を数値微分し、微分伝導(dI/dV)曲線が得られる。この曲線は、V>0 でサンプル局所電子状態密度(LDOS)にトンネル確率関数(T)と探針のフェルミ準位での LDOS をかけたものに当たる。サンプル LDOS は、この曲線を

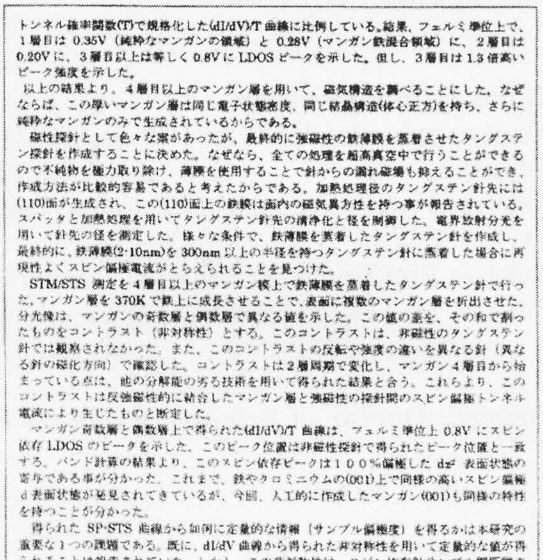

トンネル確率関数(T)で規格化した(dI/dV)/T 曲線に比例している。結果、フェルミ準位上で、1 層目は 0.35V（純粋なマンガンの領域）と 0.28V（マンガン鉄混合領域）に、2 層目は 0.20V に、3 層目以上は等しく 0.8V に LDOS ピークを示した。但し、3 層目は 1.3 倍高いピーク強度を示した。

以上の結果より、4 層目以上のマンガン層を用いて、磁気構造を調べることにした。なぜならば、この厚いマンガン層は同じ電子状態密度、同じ結晶構造(体心正方)を持ち、さらに純粋なマンガンのみで生成されているからである。

磁性探針として色々な案があったが、最終的に強磁性の鉄薄膜を蒸着させたタングステン探針を作成することに決めた。なぜなら、全ての処理を超高真空中で行うことができるので不純物を極力取り除け、薄膜を使用することで針からの漏れ磁場も抑えることができ、作成方法が比較的容易であると考えたからである。加熱処理後のタングステン針先には(110)面が生成され、この(110)面上の鉄膜は面内の磁気異方性を持つ事が報告されている。スパッタと加熱処理を用いてタングステン針先の清浄化と径を制御した。電界放射分光を用いて針先の径を測定した。様々な条件で、鉄薄膜を蒸着したタングステン針を作成し、最終的に、鉄薄膜(2-10nm)を 300nm 以上の半径を持つタングステン針に蒸着した場合に再現性よくスピン偏極電流がとらえられることを見つけた。

STM/STS 測定を 4 層目以上のマンガン膜上で鉄薄膜を蒸着したタングステン針で行った。マンガン層を 370K で鉄上に成長させることで、表面に複数のマンガン層を析出させた。分光像は、マンガンの奇数層と偶数層で異なる値を示した。この値の差を、その和で割ったものをコントラスト（非対称性）とする。このコントラストは、非磁性のタングステン針では観察されなかった。また、このコントラストの反転や強度の違いを異なる針（異なる針の磁化方向）で確認した。コントラストは 2 層周期で変化し、マンガン 4 層目から始まっている点は、他の分解能の劣る技術を用いて得られた結果と合う。これらより、このコントラストは反強磁性的に結合したマンガン層と強磁性の探針間のスピン偏極トンネル電流により生じたものと断定した。

マンガン奇数層と偶数層上で得られた(dI/dV)/T 曲線は、フェルミ準位上 0.8V にスピン依存 LDOS のピークを示した。このピーク位置は非磁性探針で得られたピーク位置と一致する。バンド計算の結果より、このスピン依存ピークは１００％偏極した dz^2 表面状態の寄与である事が分かった。これまで、鉄やクロミニウムの(001)上で同様の高いスピン偏極 d 表面状態が発見されてきているが、今回、人工的に作成したマンガン(001)も同様の特性を持つことが分かった。

得られた SP-STS 曲線から如何に定量的な情報（サンプル偏極度）を得るかは本研究の重要な１つの課題である。既に、dI/dV 曲線から得られた非対称性を用いて定量的な値が得られることは報告されていた。しかし、この非対称性は、スピン依存針サンプル間距離の影響を強く受けるため信頼できないことを見つけた。一方 LDOS を再現する(dI/dV)/T 曲線をから得られる非対称性は、V＞０で、直接、サンプル偏極度にフェルミ準位での針偏極度をかけたものであることを示す。この非対称性は、針サンプル間距離の影響を受けないことを実験より示した。さらに、実験より得られた(dI/dV)/T 曲線を用いてスピン分解 LDOS を得、これは、探針のフェルミ準位でのスピン偏極度を１８％と見積もった時、計算より得られたスピン分解 LDOS と合った。(dI/dV)/T の非対称性を用いた方法が定量的な値（サンプル偏極度）を得るのに最も信頼性のある方法と考えられる。

また、下地の鉄ステップの場所でマンガン膜の磁気コントラストが 0.4nm で反転している事を見つけた。この値が、スピン偏極 STS を用いて得られた最高磁気分解能である。

FIG. 2.

Contents

I. ACKNOWLEDGEMENTS

Spin-polarized scanning tunneling microscopy and spectroscopy works were supported by the Stichting voor Fundamenteel Onderzoek der Materie (FOM), which is funded by the Nederlandse Organisatie voor Wetenschappelijk Onderzoek (NWO), and the European Growth Project MAGNETUDE. I would like to thank Gakushuin University for a travel grant. Scanning electron microscopy with polarization analyzer (SEMPA) work was supported by the High Tech Research Center from the Ministry of Education Science, Sports and Culture.

I would like to thank to Prof.dr. Tadashi Mizoguchi for giving me an opportunity to study at the University of Nijmegen for two years. Also, I would like to thank Mrs. Mizoguchi for her hospitality. I acknowledge helpful discussions about SEMPA measurements with Dr. Jun Fujii. Also, I would like to thank my students at Gakushuin University: Mr. Y. Ishii, Mr. Y. Oshima, and Mr. M. Yoshida for helping me with the measurements and for all other kind of things.

During my stay in Nijmegen (The Netherlands) many people helped me. I would like to thank all of them. I am especially grateful to Prof. Herman van Kempen since he allowed me to study in University of Nijmegen. I also would like to thank his wife Thea. In University of Nijmegen I was lucky to meet Dr. M.M.J. Bischoff (Maarten). He taught me everything to survive in Nijmegen. He was my teacher and friend. I hope I continue to discuss with him about physics and others forever (!?). I was also happy to study with Prof.dr. A.L. Vazquez de Parga (Amadeo). You suddenly appeared from Madrid and gave me a lot of helpful discussions as well as nice Spanish meals. Also, thanks a lot to your girlfriend Cristina.

For technical problems Jan Hermsen always helped me. I would like to thank him for his kinds and funniment. Also, Jan Gerritsen, A. van Etteger, W. Szweryn and T. Toonen helped me with other problems. I would like to thank these technicians. I would like to thank Mr. G.M.M. Heijnen for his calculations. I would like to thank our secretaries: Riki and Marilou for taking care of me always. Dr. K. Takazawa and Mrs. M. Takazawa helped me a lot to survive in Nijmegen. Especially thanks to teach me how to cook Japanese meals. By talking with Japanese people in Nijmegen, Dr. A. Tsukamoto, Ms. Ms. Sadakata, and Mr. M. Fukushima helped me against homesick. I am grateful to Mr./Mrs. Kuroda, Mr./Mrs. Harada and other members of the Ouyuu-kai in Amsterdam: graduated people from Gakushuin University for encouraging and giving me frequently nice Japanese meals. I would like to thank officers of Gakushuin University: Ms. E. Orihara, Ms. K. Noda, Ms. Funase, and Ms. M. Terauchi for helping me during my PhD. I really enjoyed my PhD with my friends: Takano, Hosoya, Mr./Mrs. Takahashi, Kinoshita, Nishido, Saito, Dr.Tokii, Bas, Randy, Markus, Eric, Stephanie, Sergey, Ventsi, Cristelle, Muriel, Kimel, Gabor, Piotrek, Lous and her husband and all other people.

I am especially grateful to Dr. B. Heinrich and Dr. D.T. Pierce for supplying us with the Fe whiskers and to Prof.dr. A.I. Lichtenstein and Prof.dr. S. Speller for helpful discussions.

Finally, I would like to thank my grandmother, my sister, my mother and my father for everything.

FIG. 3. Here, I show some people's pictures whom I met during my PhD. 1. T.K.Yamada (24 years old) 2. Prof. T.Mizoguchi 3. Prof. H.van Kempen 4. Prof. A.L.Vazquez de Parga 5. Prof. S.Speller 6. Ing. J.Hermsen 7. Ing. A.van Etteger 8. Ing. J.Gerritsen 9. Dr. D.Pierce 10. Mrs. R.Gommers 11. Mrs. M.van Breemen 12. Ir. W.Szweryn 13. Mr. T.Toonen 14. Drs. M.Travaille(Markus) 15. Dr. A.Tsukamoto(Arata) 16. Mr. Y.Ishii 17. Mrs. Kuroda 18. Mr. Kuroda 19. Mrs. Takazawa 20. Dr. K.Takazawa 21. Dr. J.Fujii 22. Dr. M.M.J.Bischoff(Maarten) 23. Drs. R.de Kort(Randy) 24. Drs. B.Hulsken(Bas) 25. T.K.Yamada (27 years old).

II. INTRODUCTION

In 1673, Antony van Leeuwenhoek (Delft, the Netherlands) published the first microscopy results and opened the "microscopic" world, which showed bacteria, free-living and parasitic microscopic protists, sperm cells, blood cells and more with a magnification of 300 times [1] . About 300 years later, Gerd Binnig and Heinrich Rohrer developed a new type of microscope able to resolve the atomic structure of solid surfaces [1]. This extremely high magnification microscope technique was called scanning tunneling microscopy (STM) [1]. During the last two decades many developments were observed for STM and scanning tunneling spectroscopy (STS) techniques. The atomically resolved topographic images gave us a wealth of information, and their inventors received in 1986 the Nobel Prize in Physics.

In the last two decades computer technology developed extremely as well. The main reason was the development of epitaxial growth technologies. Using this technique people were able to make atomically flat ultrathin films with metals or semiconductors. Especially, ultrathin films made of magnetic metals were found to have unique magnetic properties, which do not exist in bulk. By using these properties many kinds of new devices have been fabricated. These are called spin electronic devices. An example is the giant magnetoresistance head, which is used inside computers. By using magnetic domains on magnetic thin films, information can be stored binary. Such small domains are called "bits". In order to get a higher areal storage density people have fabricated smaller and smaller bits. In 2003, the bit size is close to ~100 nm. Although according to Moore's law this size will be smaller soon (~10 nm in 2010) [2], the extremely rapid developments to minimize the bit size are facing problems such as super-paramagnetization or thermal stability. And, the magnetic properties of nano-magnets are not fully known.

To investigate the magnetic properties at the surface or interface of thin films, several methods were reported: spin-polarized (inverse) photoelectron spectroscopy, spin-polarized low-energy electron diffraction, X-ray magnetic circular dichroism, magneto-optical Kerr effect, magnetic second harmonic generation, and Lorentz microscopy. However, these techniques cannot resolve magnetic information at an atomic scale. To approach the atomic scale detectors in combination with scanning probe microscopies were fabricated. Magnetic force microscopy showed a magnetic resolution of 30 nm in ultra-high vacuum (UHV) in 2002 [3] and scanning electron microscopy with polarization analyzer (SEMPA) showed a magnetic resolution of 5 nm in UHV in 2001 [4]. However, these magnetic resolutions are still far from the atomic scale.

With STM/STS magnetic structures at an atomic scale can be studied when a magnetic tip is used. These techniques are called spin-polarized scanning tunneling microscopy (SP-STM) and spectroscopy (SP-STS). Also, from a scientific point of view, it is very important and interesting to study magnetism at the surface or interface of thin films at an atomic scale since the electronic, magnetic, geometric structures of the magnetic films

---

[1] Compound microscopes using more than one lens were invented around 1595 by Zacharias Janssen (Middleburg, the Netherlands). Also, Robert Hooke (England) published "*Micrographia*" in 1665.

are not fully known and the relation between SP-STM/SP-STS data can detect all this information at the same time.

SP-STM/SP-STS technique was carefully studied during my PhD. And, we succeeded to detect spin-polarized tunneling current. Until 2004, only a few laboratories in the world succeeded to detect magnetic information with SP-STM/SP-STS and our group is one of them [5–8].

Although an Fe-coated W tip was already used as a SP-STM/SP-STS tip [5,7], details of the preparation of the tip depend on each laboratory. Thus, first, we have to find the preparation method to make the Fe-coated W tip using our setup. Although it took a lot of efforts, finally we found our original method, i.e. tungsten tips with a radius larger than 200 nm coated by 2-10 nm iron films detect spin-polarized current at RT in UHV reproducibly without an application of external magnetic field [chapter III]. We prepared more than 50 different Fe-coated W tips and measured spin-dependency in SP-STS. In this thesis, the SP-STS data which show the highest magnetic contrast are used.

As an magnetic sample we chose manganese (001) films grown on Fe(001) at 370 K. The growth, intermixing, geometric, and electronic structure were studied (see chapter IV). On this sample surface, we found that the manganese (001) layers couples anti-ferromagnetically with the layers below and above. Also, the highest lateral magnetic resolution (~0.4 nm) in SP-STS was confirmed [chapter V]. A spin-dependent LDOS peak was observed above the Fermi energy. This peak was found to be contributed by two d_{z^2} surface states and one d_{z^2} surface resonance state [chapter VI].

Finally, using the tip described above and the sample, we show the most reliable and simple method to obtain quantitative information from experimentally obtained SP-STS. Although already several methods were reported to obtain quantitative values from SP-STS data, we show that these methods include an influence of the spin-dependent tip-sample separation. It is therefore complicated to extract quantitative data from these results. We show a new method to solve these problems. We represent how to recover spin-resolved sample surface LDOS. With this LDOS, a 18±5 % tip polarization at the Fermi energy is obtained. Thus, we experimentally obtained from SP-STS data that the Mn(001) surface has a 60±16 % polarization at the spin-dependent LDOS peak energy [chapter VII]. [2]

A. STM

According to the basic principle behind the quantum mechanical tunneling effect, electrons can tunnel through vacuum (~1 nm) between two electrodes (i.e., sample and tip). Experimentally, STM measurement is performed as follows. A conductive sample

---

[2] Other studies during my PhD are written in my PhD thesis for the University of Nijmegen (=Radboud University) (The Netherlands). Both theses can be downloaded from http://www.evsf2.sci.kun.nl/publications.htm

is applied a bias voltage [3] . A conductive tip (e.g. tungsten (W)) is approached to the sample and the tunneling current is detected. Then, the tip stops approaching to keep a constant current. The tip is scanned on the sample surface to keep the current constant. Thus, atomically resolved STM topographic images are obtained [1].

In 1961, Bardeen first proposed the basic theory for a tunnel junction using a many-body transition Hamiltonian [9]. Later several people developed this theory [10–12]. Using this transition Hamiltonian three-dimensional (3D) tunneling in the STM was studied by Tersoff and Hamann [13], Garcia *et al.* [14], and Lang [15]. In Tersoff and Hamann's theory, the solutions of the Schrödinger equation for a spherical potential of radius R were taken as tip wave functions, i.e. only the s-wave solution was assumed to be important. At low voltages, the tunneling current is proportional to the Fermi-level local density of states (LDOS) at the center of curvature of the tip $\vec{r}_o$.

$$I \propto \Sigma_{E_\mu=E_F-eV}^{E_F}|\psi_\mu(\vec{r}_o)|^2 = eV\rho_s(\vec{r}_o, E_F) \tag{1}$$

where ψ_μ denotes the wave function at the state μ, E_F the Fermi energy, and ρ_s the LDOS of the sample, which is defined as $\rho_s(z,E) \equiv \frac{1}{\epsilon}\Sigma_{E_\mu=E-\epsilon}^{E}|\psi_\mu(z)|^2$. Thus, in the s-wave model, a constant current STM image is a Fermi-level LDOS contour of the sample surface taken at the center of the curvature of the tip $\vec{r}_o$, i.e. the STM image reflects the property of the sample only [13]. In this model, the simple metal surfaces with fundamental periodicity a has the corrugation amplitude (Δz) of the Fermi level LDOS as a function of the tip-sample separation (z):

$$\Delta z \approx \frac{2}{\kappa} exp[-2z(\sqrt{\kappa^2+\pi^2/a^2}-\kappa)]. \tag{2}$$

where κ denotes the decay constant: $\kappa = \sqrt{2m\Phi}/\hbar$, m the electron mass, $\hbar$ the Plank constant, and Φ the averaged work function between tip and sample. Also, the lateral resolution (Δx) can be estimated as a function of the tip-sample separation (d) and s-wave tip radius of curvature (R):

$$\Delta x \approx \sqrt{(2\text{Å})(R+z)}. \tag{3}$$

Although the s-state tip model explains the contours of the superstructures on the Au(110) surface [13], it cannot explain the atomic resolution on low-Miller-index metal surfaces, i.e. the experimentally observed corrugation amplitude was more than one order of magnitude larger than the Fermi level LDOS corrugation. Baratoff proposed that the atomic resolution in STM is due to a single dangling bond protruding from the tip [16]. Especially, the d_{z^2} surface state on W(001) surface is located at the Fermi level. Also, Onishi and Tsukada made a first principles calculation of the electronic states for a number of W clusters, which showed that there is a d_{z^2}-like state protruding from the apex atom near the Fermi energy [17]. Only these d-type localized state on the tip apex is interpreted as a cause of the large corrugation.

---

[3] When a positive (negative) voltage is applied to the sample, electrons tunnel from a tip (sample) Fermi energy to sample (tip) unoccupied local density of states.

B. STS

The theory of STS was studied by Selloni *et al.* [18] and Lang [19] and it was concluded that, in the general case of 3D tunneling, the tunneling current cannot be calculated as a simple convolution of sample density of states (DOS) and tip DOS. The simple relation between sample DOS and tunneling current can be obtained in the one-dimensional (1D) and semi-classical Wentzel, Kramers, and Brillouin (WKB) approximation only [20]. Until now, theories of STS are limited in 1D only. Selloni *et al.* qualitatively generalized the model of Tersoff and Hamann and suggested that a convolution of sample DOS and tunneling transmission probability (T') is a crude estimation of the tunneling current [18].

The first experimental realization of STS was shown on graphite [18]. The results of differential conductivity (dI/dV) curves revealed not only the graphite DOS, but also the influence of the tip DOS and the T'. To solve this problem, Stroscio *et al.* suggested normalization of the dI/dV by the total conductivity (I/V), which can effectively remove the tip-sample separation dependence on the current [21]. They claimed that this normalization will exclude not only the tip-sample separation dependence but also the tip-sample voltage dependence in the T', and will show the sample DOS. This normalization technique was confirmed to be correct by simulations with metal-like DOS since the simulations showed a qualitatively agreement between the $(dI/dV)/(I/V)$ and the input sample DOS. However, there was still a clear influence of the tip DOS on the normalized results [20].

Then, it was realized that the theory of STS and the proposed normalization method to recover the DOS are still not good enough since all theory is based on 1D semi-classical WKB approximations. As concerning these theories, the most successful scheme to recover the DOS from the STS data was proposed by Ukraintsev in 1996. He showed that the $(dI/dV)/(I/V)$ method cannot completely remove the voltage dependence of the tunneling probability [20]. Although this theory still includes assumptions, this normalization technique was applied to our experimentally obtained STS and we found that this normalization is the best method to recover the sample DOS [8,22,23]. Therefore, in this thesis, Ukraintsev's theory was used to investigate the sample DOS and the spin-resolved sample DOS. Also, based on Ukraintsev's theory it will be shown how spin-dependent tunneling influences dI/dV.

In this thesis, DOS refers to the local DOS, i.e. the DOS at a position $\vec{r}$, since local probe techniques such as STM/STS detect local information instead of space-averaged information. Usually the position $\vec{r}$ is the tip position. The tip detects a convolution of all wave functions on the sample surface at the tip position: $DOS(E,\vec{r}) = lim_{\epsilon\to 0}\frac{1}{\epsilon}\sum_{E_\mu=E}^{E+\epsilon}|\psi_\mu(E_\mu,\vec{r})|^2$.

The tunneling current between two weakly bounded electrodes using first order perturbation theory (Bardeen's theory) is described as follows:

$$I(z,V) = \frac{2\pi e}{\hbar}\sum_{t,s}|M_{t,s}|^2\delta(E_t - E_s)[f(E_t - eV) - f(E_s)], \tag{4}$$

where e is the electron charge, $\hbar$ Plank's constant, V the sample bias voltage, z the tip-sample separation, $M_{t,s}$ the tunneling matrix element between the tip state ψ_t and the sample state ψ_s, $f(E)$ the Fermi-Dirac function, and E_t and E_s the energies of ψ_t and ψ_s, respectively [12,13]. The tunneling matrix is described as follows:

$$M_{t,s} = -\frac{\hbar^2}{2m}\int(\psi_t^*\nabla\psi_s - \psi_s^*\nabla\psi_t)dA, \tag{5}$$

where the integral is calculated over an arbitrary surface in the vacuum region between tip and the sample [9]. In the tunneling matrix, the electron transition between different states (s, p, d, and f-state) are included. Usually, the tip and the sample have several electronic states and each state has different decay factor. For example, a transition between an s-state ↔ p-state and an s-state ↔ d-state is different, i.e. $\exp(-(\kappa_s + \kappa_p)z)$ and $\exp(-(\kappa_s + \kappa_d)z)$, where κ denotes the decay length and z the tip-sample separation. However, using the 1D semi-classical WKB approximation, the density of the tunneling current between two planar electrodes can be described by assuming an equal decay length for all electron transitions:

$$J(z,V) \cong \frac{2\pi e}{\hbar}\Big(\frac{\hbar^2}{2m}\Big)^2\int_{-\infty}^{\infty} T'(z,V,E)[f(E-eV)-f(E)]\rho_s(E)\rho_t(E-eV)dE, \tag{6}$$

where T' is the tunneling transmission probability function, $\rho_s(E)$ and $\rho_t(E)$ are the sample DOS at the tip position and tip local DOS at the tip position, respectively [12,13]. The tunneling probability for a trapezoidal barrier can be estimated in the WKB approximation as

$$T'(z,V,E) \cong exp\Big[-2z\Big(\frac{2m}{\hbar^2}[\bar{\Phi} + \frac{eV}{2} - (E - E_{\|})]\Big)^{1/2}\Big], \tag{7}$$

where $\bar{\Phi}$ is the average of the sample and the tip barrier heights, $E_{\|} = \hbar^2 k_{\|}^2/2m$ is the component of electron energy parallel to the tip and the sample surface. $k_{\|}$ is the corresponding electron momentum [24]. Since the DOS at the Γ point in the k-space mainly contributes to the tunneling, $E_{\|} \approx 0$ [20]. Furthermore, tunneling at low temperatures is assumed, which changes the Fermi-Dirac function to a step function [20]. Then,

$$J(z,V) \cong \frac{2\pi e}{\hbar}\Big(\frac{\hbar^2}{2m}\Big)^2\int_{0}^{eV} T'(z,V,E)\rho_s(E)\rho_t(E-eV)dE. \tag{8}$$

The tip-sample separation z is included only inside the tunneling probability function. The z dependence is not included inside the sample and the tip DOS. When z is 0, the tip and the sample are connected [see Fig. 4(a)]. Then, when z increases to d, only the exponential term changes [see Fig. 4(b)].

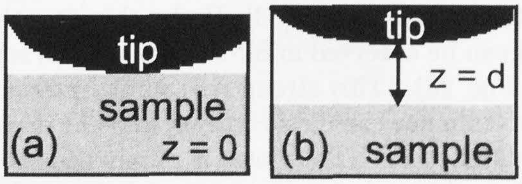

FIG. 4. (a,b) Situations of the tip and the sample, when the tip-sample separation is $z = 0$ (a) and $z = d$ (b).

C. SP-STM / SP-STS

Magnetic imaging with STM was first proposed by Wiesendanger in 1990. He showed an effort of spin-polarized tunneling in the topographic image recorded with a half metallic CrO_2 tip [25]. Since the species at the tip apex cannot be precisely controlled for a half metallic tip as well as the tip spin-polarization, recently Prof. Wiesendanger's group used W tips covered by thin magnetic films and published many publications and reported many developments of SP-STM/SP-STS ([5] and refs. therein). An atomically-resolved magnetic image in SP-STM and a magnetic resolution of 1-2 nm in SP-STS were reported. These magnetic-film-coated W tips can be prepared in ultra-high vacuum and the magnetic and the geometric structures can be controlled at an atomic layer scale. Also, STM with optically pumped GaAs tips was reported by van Kempen *et al.* [26] and Suzuki *et al.* [27]. They detect spin-polarized electrons from the magnetic sample with the GaAs tip. A use of photo-excited electrons to detect magnetic information of the sample surface is ideally the best way to obtain precise spin-resolved sample LDOS since the tip does not influence the specimen surface magnetism. However, the preparation and the control of the GaAs tip take a lot of effort compared to the other methods. Soft magnetic material tips, e.g. Ni or amorphous FeCoB, were used by Wulfhekel *et al.* to detect sample magnetic information by switching the tip magnetization with a coil surrounding the tip [28]. Recently, a magnetic resolution of ~1 nm was reported with this technique.

As far as I know three kinds of STM magnetic imaging were reported.
The first one is the so-called SP-STM. SP-STM gets a constant current topographic image, i.e., during the measurement the feedback is closed and sustains a constant tunneling current. In 2000, Heintz *et al.* published an atomically resolved SP-STM image, which was recorded on a sample of 1 ML Mn on W(110) [29]. A non-magnetic W tip detected a p(1×1) structure, whereas an Fe-coated W tip detected a c(2×2) structure. In the case of 1 ML Mn on W(110), the SP-STM result can be trusted to detect magnetic structures since this system is close to an ideal system, i.e., the Mn layer does not include any intermixing and disordered structures. Even using this ideal sample, still calculations were needed to prove whether magnetic information was obtained. A theory of SP-STM was described by Heintz and Blügel [29,30], in which Tersoff and Hamann's model was modified by modeling an s-state tip by a spin-polarized tip, whereas practically the tip DOS is unknown since the tip DOS depends on the tip shape, volume, and comprises both s, p, d, and f states [31–33].

The weak point of SP-STM is that this method can extract not only magnetic information, but also other effects. Usually to obtain the atomically resolved images, a metal tip is brought close to a metal sample surface [33]. Under this situation, a strong tip-sample interaction occurs, which can be observed in SP-STM images as scratched line-noise along the scan direction (e.g. Fig. 20). This strong tip-sample interaction is known to cause tip-changes and is used to enhance chemical contrast in STM images. Therefore, it is difficult to prove that the obtained SP-STM image is purely caused by magnetic structures of the sample surface. Thus, this technique is not straightforward to investigate magnetic structures.

The second method, which is called SP-STS, was also introduced by Wiesendanger *et* *al.* [34]. During the SP-STS measurements the feedback loop is closed. This technique obtains dI/dV values by modulating the sample bias voltage ($\sim \pm 20$ mV) at the set point voltage with a lockin-amplifier with a higher frequency than the feedback frequency. Simultaneously, SP-STM images are also obtained. By choosing the voltage (current) set point high (low) enough one can exclude the tip-sample interaction and only the electronic and the magnetic structure of the sample is detected. To prove the reliability of this technique, good samples are needed: atomically flat ordered magnetic layers with homogeneous electronic structure and no intermixing. Also, since the STS measures the sample DOS (as well as the tip DOS and the tunneling probability), samples with highly spin-polarized d surface states were used, e.g. Cr(001) [34], Fe films on W(110) [5], Co(0001) [28], and Mn films on Fe(001) [8]. However, to obtain quantitative information from SP-STS results, we found that use of the second method is not possible (see chapter VII). To obtain quantitative information, such as sample polarization, we have to measure the full $I(V)$ curve as a function of sample bias voltage by opening the feedback. Then, the full dI/dV curves are obtained by a numerically differentiation. Using dI/dV curves normalized by tunneling probability functions quantitative information can be obtained. This is the third method. Since the dI/dV includes the dependence of the spin-dependent tip-sample separation, the obtained values from the dI/dV do not show correct spin-dependent values. In order to obtain quantitative information (e.g. sample polarization as well as spin-resolved sample LDOS), the third method is the best since this method can remove the influence of the spin-dependent tip-sample separation. The second method can be useful to obtain well resolved magnetic images (qualitative information). In this thesis, since the emphasis is not on highly-resolved imaging but mainly on understanding the origin of the magnetic contrast as well as extracting quantitative information about the sample polarization, I use only the third method.

Figure 5 shows a simple model to understand STS measurements on magnetic sample surfaces. Here, no spin-flip during tunneling is assumed. The sample surface is assumed to have in-plane magnetization and the magnetizations between different terraces couple antiferromagnetically. (Each terrace has the same total (spin-up + spin-down) DOS. But the majority-spin below the Fermi energy changes from spin-up to spin-down or vice versa.) Since a non-magnetic tip is used, the tip has the same DOS for spin-up and spin-down states at the Fermi level. When a positive bias voltage is applied to the sample, the spin-up and spin-down electrons of the tip DOS at the Fermi level tunnel into the spin-up and spin-down DOS of the unoccupied sample DOS. Thus, the obtained STS results show the total DOS of the sample, i.e., there is no difference in STS obtained on different terraces [4] .

---

[4] It was reported that even a W tip could detect a spin-orbit coupling in SP-STS results around a magnetic domain boundary on Fe films grown on W(110) [35]. In our model we do not take this effect into account.

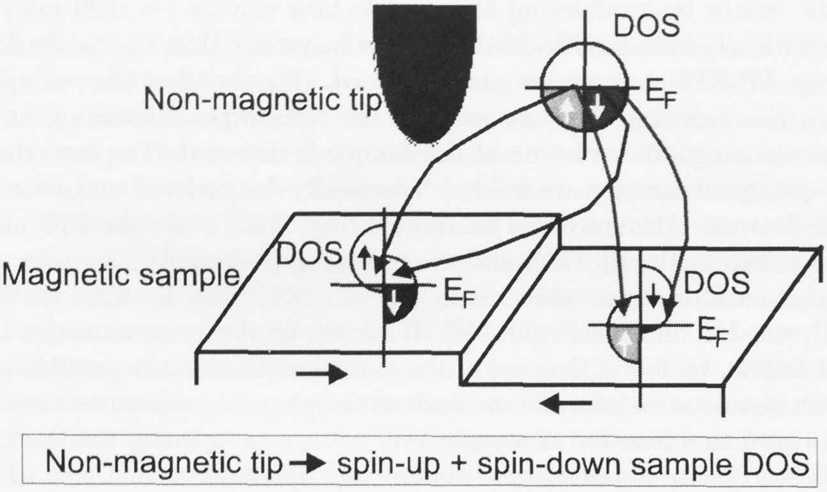

FIG. 5. Scheme of the tunneling process from a non-magnetic tip to a magnetic sample. Different sample terraces are assumed to have opposite in-plane magnetizations. "E_F" denotes the Fermi energy. "↑" and "↓" denote spin-up and spin-down electrons, respectively. "→" and "←" denote sample magnetizations.

When the non-magnetic tip is changed to a magnetic tip, SP-STS can be measured, which model is shown in Fig. 6. The DOS of the magnetic tip is assumed to have only spin-up electrons at the Fermi level, i.e., the tip is 100 % polarized. When a positive bias voltage is applied to the sample, spin-up electrons at the Fermi level tunnel from the tip to the unoccupied spin-up sample DOS. Therefore, the obtained SP-STS results show only the spin-up DOS of the sample and magnetic information can be obtained.

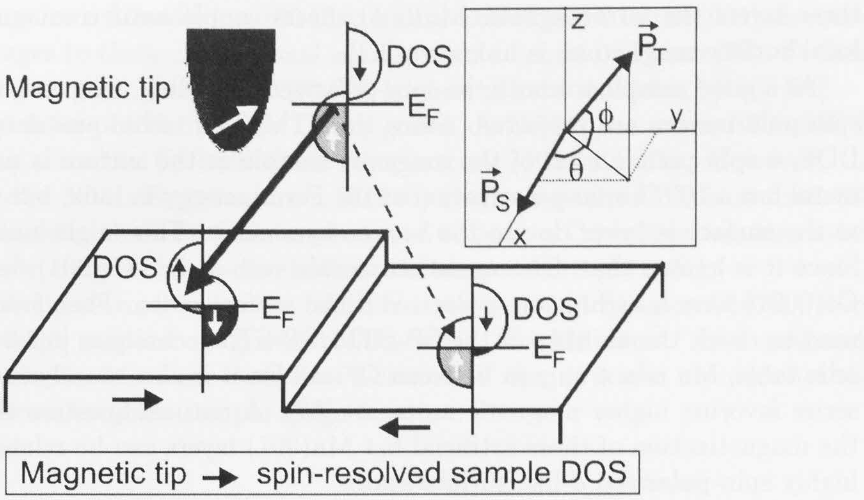

FIG. 6. Scheme of the tunneling process from a magnetic (a 100 % polarized) tip to a magnetic sample. Different sample terraces are assumed to have opposite in-plane magnetizations. "E_F" denotes the Fermi energy. "↑" and "↓" denote spin-up and spin-down electrons, respectively. The right-top inset shows the coordinate axis. $\vec{P}_T$ and $\vec{P}_S$ denote polarization vectors of the tip and the sample, respectively.

D. Mn films on Fe(001)-whisker

The development of epitaxial growth techniques has led to considerable practical applications such as metallic-multilayer-devices. Especially, ultrathin magnetic films evaporated on magnetic substrates show enormous different magnetic and electronic properties compared to the bulk caused by their lower dimensions ([36] and refs. therein). Regarding the novel magnetic and electronic properties at the surface and the interface, particularly, the system of Mn films on Fe(001) is remarkable since recent calculations [37–48] and experiments [49–62] show conflicting results indicating the complicated relation between growth condition, electronic structure, and magnetic coupling. Previous results showed that body-centered tetragonal (bct) (001) surfaces can be stabilized by thin film growth at Fe(001) surfaces [23,60,63], whereas Mn does not exist in a bulk bcc phase at room temperature (RT) [5] . And, recent SEMPA results suggested that for films thicker than

---

[5] Manganese (Mn) is the strangest of the $3d$ metals and has many features that are not well understood. Mn has four allotropes in bulk: a cubic α phase with 58 atoms/cell (RT ~ 997 K); a cubic β phase with 20 atoms/cell (997 K ~1368 K); a face-centered cubic γ phase (1368 ~ 1406 K); a body-centered cubic δ phase (1406 ~ the melting point 1517 K). α-Mn shows antiferromagnetic properties with a Néel temperature of 95 K. β-Mn shows antiferromagnetic properties with a Néel temperature of <1 K. γ-Mn shows antiferromagnetic properties with a Néel temperature of 540 K. The artificial bct-Mn shows antiferromagnetic properties with a Néel

three layers the ferromagnetic Mn(001) sheets couple antiferromagnetically whereas the local surface magnetism is unknown [52].

As a good sample to check the spin-polarized tunneling, magnetic materials with a high spin-polarization are preferred. Since the STM/STS techniques detect sample "surface" DOS, a spin-polarization of the magnetic sample at the surface is necessary (e.g. a half-metal has a 100 % spin-polarization at the Fermi energy in bulk, but the spin-polarization at the surface is lower due to the broken symmetry. This might not a good candidate.). Since it is known that, 3*d*-transistion metals such as bcc-Cr(001), bcc-Fe(001), and hcp-Co(0001) have a highly spin-polarized *d*-like surface state. Therefore, these samples were used to check the abilities of the SP-STM/SP-STS techniques [6,7,34,65,66]. In the periodic table, Mn is not only in between Cr and Fe, it is also exactly in the middle of the 3*d* series favoring higher magnetic moments [67]. A natural question that arises is whether the magnetization of these artificial bct Mn(001) layers can be related to the existence of highly spin-polarized *d*-like surface states.

Furthermore, the study with local magnetic microscopy with sub-nanometer resolution of a system consisting of an antiferromagnet on top of a ferromagnet is of utmost importance for fundamental understanding of nanomagnetism and possible applications such as spin electronics devices.

These motivations make me to decide to choose Mn films grown on Fe(001) as an ideal sample for the study of SP-STM/SP-STS.

BCC Fe(001) whiskers were used as a substrate since the Fe-whisker has close magnetic domains with a single domain size of ~500 μm [68].

E. Magnetic STM/STS tips

Fe-coated W tips were used as spin-polarized tips in this thesis. As described before several kinds of spin-polarized tips were reported: GaAs tips [26,27], bulk soft-magnetic tips [28], and magnetic thin films-coated W tips [5,69]. The last one seemed to be easier to prepare than others. Also, Wiesendanger *et al.* reported that the Fe-coated W tips detect in-plane magnetization [5,69]. The growth and magnetic structures of the Fe film on the W tip can be compared to the results of Fe on W(110) single crystals since the annealed W tip is known to exposes a (110) surface at the apex due to a low surface energy [70–73]. The (110) surface could be confirmed by the field emission spectroscopy image (see Fig. 15), while several grains with the (110) surface likely point to different directions. The Fe films grow layer-by-layer at room temperature (RT), while the second layer shows an onset of misfit dislocations. The thicker (>2 nm) Fe films grown at RT show a high density of atomic steps along [001] [74]. The Fe films show a pronounced tendency for Stranski-Krastanov (three-dimensional) growth at higher temperature (500-800 K). Studies of Fe films grown on W(001) show similar characteristics [75].

Fe(110) with a thickness of 3 nm grown on W(110) at RT shows two-dimensional growth (with dislocation network) and in-plane magnetization with easy axis along $[\bar{1}10]$

---

temperature of >520 K [49,52,64].

[73]. When the 3 nm film is annealed at 700 K, the easy axis changes to the [001] direction and the Fe film changes to three-dimensional islands with a height of 17 nm [73]. Fe films thicker than 10 nm grown on W(110) at 300-600 K show a hard axis along $[\bar{1}10]$ [74].

The Curie temperature of Fe films (<1 ML) grown on W(110) is around 200-250 K which is much lower than the Fe bulk Curie temperature (1044 K) [76]. However, the Curie temperature of 1.3 ML Fe grown on a W(110) single crystal at RT is around 380 K (> RT) [77]. Therefore, thick Fe films are believed to have a Curie temperature much higher than RT, likely comparable to the bulk Curie temperature (1044 K).

The Fe-coated W tip seemed to be the best for a study of Mn films on Fe(001) since SEMPA results showed in-plane magnetic contrasts for the Mn films. If a magnetic contrast is obtained on the Mn films with the Fe-coated W tips, it is also a proof that the Fe-coated W tip detects in-plane sample magnetization.

REFERENCES

[1] G. Binnig, H. Rohrer, Ch. Gerber, and E. Weibel, Phys. Rev. Lett. **49** (1982) 57.
[2] Gordon E. Moore, Electronics, **38** (1965) No.8.
[3] G.N. Philips, M. Siekman, L. Abelmann, and J.C. Lodder, Appl. Phys. Lett. **81** (2002) 865.
[4] T. Kohashi and K. Koike, Jpn. J. Appl. Phys. **40** (2001) L1264.
[5] M. Bode, Rep. Prog. Phys, **66** (2003) 523.
[6] H.F. Ding, W. Wulfhekel, J. Henk, P. Bruno, and J. Kirschner, Phys. Rev. Lett. **90** (2003) 116603.
[7] S.N. Okuno, T. Kishi, and K. Tanaka, Phys. Rev. Lett. **88** (2002) 066803.
[8] T.K. Yamada, M.M.J. Bischoff, G.M.M. Heijnen, T. Mizoguchi, and H. van Kempen, Phys. Rev. Lett. **90** (2003) 056803.
[9] J. Bardeen, Phys. Rev. Lett. **6** (1961) 57.
[10] M.H. Cohen, L.M. Falicov, and J.C. Phillips, Phys. Rev. Lett. **8** (1962) 316.
[11] C.B. Duke, S.D. Silverstein, and A.J. Bennett, Phys. Rev. Lett. **19** (1967) 312.
[12] J.A. Appelbaum and W.F. Brinkman, Phys. Rev. **186** (1969) 464.
[13] J. Tersoff and D.R. Hamann, Phys. Rev. Lett. **50** (1983) 1998; Phys. Rev. B **31** (1985) 805.
[14] N. Garcia, C. Ocal, and F. Flores, Phys. Rev. Lett. **50** (1983) 2002.
[15] N.D. Lang, Phys. Rev. Lett. **55** (1985) 230; **55** (1985) 2925; **56** (1986) 1164.
[16] A. Baratoff, Physica **127B** (1984) 143.
[17] S. Ohnishi and M. Tsukada, Solid State Commu. **71** (1989) 391.
[18] A. Selloni, P. Carnevali, E. Tosatti, and C.D. Chen, Phys. Rev. B **31** (1985) 2602.
[19] N.D. Lang, Phys. Rev. B **34** (1986) 5947.
[20] V.A. Ukraintsev, Phys. Rev. B **53** (1996) 11176.
[21] J.A. Stroscio, R.M. Feenstra, and A.P. Fein, Phys. Rev. Lett. **57** (1986) 2579.
[22] M.M.J. Bischoff, T. Yamada, A.J. Quinn, and H. van Kempen, Surf. Sci. **501** (2002) 155.
[23] T.K. Yamada, M.M.J. Bischoff, T. Mizoguchi, and H. van Kempen, Surf. Sci. **516** (2002) 179.
[24] R. Wiesendanger, *Scanning Probe Microscopy, Methods and Applications*, (Cambridge University Press, Cambridge, U.K., 1994).
[25] R. Wiesendanger, H.J. Güntherodt, G. Güntherodt, R.J. Gambino, and R. Ruf, Phys. Rev. Lett. **65** (1990) 247.
[26] M.W.J. Prins, R. Jansen, R.H.M. Groeneveld, A.P. van Gelder, and H. van Kempen, Phys. Rev. B **53** (1996) 8090; Phys. Rev. B **53** (1996) 8105; R. Jansen, M.W.J. Prins, and H. van Kempen, Phys. Rev. B **57** (1998) 4033; R. Jansen, R. Schad, and H. van Kempen, J. Magn. Magn. Mater. **198-199** (1999) 668.
[27] Y. Suzuki W. Nabhan, R. Shinohara, K. Yamaguchi, and T. Katayama, J. Magn. Magn. Mater. **198-199** (1999) 540.
[28] W. Wulfhekel and J. Kirschner, Appl. Phys. Lett. **75** (1999) 1944; W. Wulfhekel, H.F. Ding, and J. Kirschner, Appl. Phys. A **87** (2000) 6475; W. Wulfhekel, H.F. Ding, W. Lutzke, G. Steierl, M. Vázquez, P. Marín, A. Hernando, and J. Kirschner, J. Appl. Phys. **72** (2001) 463.

[29] S. Heinze, M. Bode, A. Kubetzka, O. Pietzsch, X. Nie, S. Blügel, and R. Wiesendanger, Science **288** (2000) 1805.

[30] S. Heinze, Ph.D. thesis, University of Hamburg, (2000).

[31] S. Watanabe, M. Aono, M. Tsukada, Appl. Surf. Sci. **60** (1992) 437.

[32] W.A. Hofer and A.J. Fisher, Surf. Sci. **515** (2002) L487.

[33] C.J. Chen, *Introduction to scanning tunneling microscopy*, (Oxford University Press, Oxford, U.K., 1993).

[34] M. Kleiber, M. Bode, R. Ravlić, and R. Wiesendanger, Phys. Rev. Lett. **85** (2000) 4606.

[35] M. Bode, S. Heinze, A. Kubetzka, O. Pietzsch, X. Nie, G. Bihlmayer, S. Blügel, and R. Wiesendanger, Phys. Rev. Lett. **89** (2002) 237205.

[36] H. Dreyssé and C. Demangeat, Surf. Sci. Rep. **28** (1997) 65.

[37] N. Papanikolaou, B. Nonas, S. Heinze, R. Zeller, and P.H. Dederichs, Phys. Rev. B **62** (2000) 11118.

[38] B. Nonas, K. Wildberger, R. Zeller, and P.H. Dederichs, Phys. Rev. Lett. **80** (1998) 4574.

[39] B. Nonas, K. Wildberger, R. Zeller, and P.H. Dederichs, J. Magn. Magn. Mater. **165** (1997) 137.

[40] M. Taguchi, O. Elmouhssine, C. Demangeat, and J.C. Parlebas, Phys. Rev. B **60** (1999) 6273.

[41] R. Wu and A.J. Freeman, J. Magn. Magn. Mater. **161** (1996) 89.

[42] S. Handschuh and S. Blügel, Solid State Commun. **105** (1998) 633.

[43] O. Elmouhssine, G. Moraïtis, C. Demangeat, and J.C. Parledas, Phys. Rev. B **55** (1997) R7410.

[44] S. Mirbt, O. Eriksson, and B. Johansson, Phys. Rev. B **52** (1995) 15070.

[45] R. Wu and A.J. Freeman, Phys. Rev. B **51** (1995) 17131.

[46] A. Vega, S. Bouarab, H. Dreyssé, and C. Demangeat, Thin Solid Films **275** (1996) 103.

[47] P. Krüger, O. Elmouhssine, C. Demangeat, and J.C. Parlebas, Phys. Rev. B **54** (1996) 6393.

[48] S. Bouarab, H. Nait-Laziz, M.A. Khan, C. Demangeat, and H. Dreyssé, Phys. Rev. B **52** (1995) 10127.

[49] D.T. Pierce, A.D. Davies, J.A. Stroscio, D.A. Tulchinsky, J. Unguris, and R.J. Celotta, J. Magn. Magn. Mater. **222** (2000) 13.

[50] R. Pfandzelter, T. Igel, and H. Winter, Surf. Sci. **389** (1997) 317.

[51] T. Igel, R. Pfandzelter, and H. Winter, Surf. Sci. **405** (1998) 182.

[52] D.A. Tulchinsky, D.T. Pierce, A.D. Davies, J.A. Stroscio, J. Unguris, and R.J. Celotta, J. Magn. Magn. Mater. **212** (2000) 91.

[53] O. Rader, W. Gudat, D. Schmitz, C. Carbone, and W. Eberhardt, Phys. Rev. B **56** (1997) 5053.

[54] Ch. Roth, Th. Kleeman, F.U. Hillebrecht, and E. Kisler, Phys. Rev. B **52** (1995) R15691.

[55] T.G. Walker and H. Hopster, Phys. Rev. B **48** (1993) 3563.

[56] S. Andrieu, M. Finazzi, F. Yubero, H.M. Fischer, Ph. Arcade, F. Chevrier, L. Hennet, K. Hricovini, G. Krill, and M. Piecuch, Europhys. Lett. **38** (1997) 459.

[57] J. Dresselhaus, D. Spanke, F.U. Hillebrecht, and E. Kisker, Phys. Rev. B **56** (1997) 5461.

[58] S. Andrieu, M. Finazzi, F. Yubero, H. Fischer, P. Arcade, F. Chevrier, K. Hrincovini, G. Krill, and M. Piecuch, J. Magn. Magn. Mater. **165** (1997) 191.

[59] S.K. Kim, Y. Tian, M. Montesano, F. Jona, and P.M. Marcus, Phys. Rev. B **54** (1996) 5081.

[60] S. Andrieu, M. Finazzi, Ph. Bauer, H. Fischer, P. Lefevre, A. Traverse, K. Hricovini, G. Krill, and M. Piecuch, Phys. Rev. B **57** (1998) 1985.

[61] S.T. Purcell, M.T. Johnson, N.W.E. McGee, R. Coehoorn, and W. Hoving, Phys. Rev. B **45** (1992) 13064.

[62] S. Andrieu, E. Foy, H. Fischer, M. Alnot, F. Chevrier, G. Krill, and M. Piecuch, Phys. Rev. B **58** (1998) 8210.

[63] V.L. Moruzzi and P.M. Marcus, Solid State Commu. **71** (1989) 203.

[64] http://www.agschatz.physik.uni-konstanz.de/treubel/Pt-Mn.htm.

[65] J.A. Stroscio, D.T. Pierce, A. Davies, R.J. Celotta, and M. Weinert, Phys. Rev. Lett. **75** (1995) 2960.

[66] O.Yu. Kolesnychenko, R. de Kort, M.I. Katsnelson, A.I. Lichtenstein and H. van Kempen, Nature **415** (2002) 507.

[67] B. Heinrich, A. S. Arrott, C. Liu, and S. T. Purcell, J. Vac. Sci and Technol. A **5** (1987) 1935.

[68] R. Schäfer, R. Urdan, D. Ullmann, H.L. Meyerheim, B. Heinrich, L. Schultz, and J. Kirschner, Phys. Rev. B **65** (2002) 144405.

[69] R. Wiesendanger, M. Bode, and M. Getzlaff, Appl. Phys. Lett. **75** (1999) 124.

[70] M.F.H. van Tol, F.A. Hondsmerk, J.W. Bakker, and B.E. Nieuwenhuys, Surf. Sci. **266** (1992) 529.

[71] X.-L. Zhou, C. Yoon, and J.M. White, Surf. Sci. **203** (1988) 53.

[72] H. Bethge, D. Heuer, Ch. Jensen, K. Reshöft, and U. Köhler, Surf. Sci. **331-333** (1995) 878.

[73] D. Sander, A. Enders, C. Schmidthals, D. Reuter, and J. Kirschner, Surf. Sci. **402-404** (1998) 351.

[74] H.J. Elmers and U. Gradmann, Appl. Phys. A **51** (1990) 255.

[75] P.J. Berlowitz and D.W. Goodman, J. Vac. Sci. Tech. A **6** (1988) 634.

[76] H.J. Elmers, J. Hauschild, H. Höche, U. Gradmann, H. Bethge, D. Heuer, and U. Köhler, Phys. Rev. Lett. **73** (1994) 898.

[77] W. Weber, D. Kerkmann, D. Pescia, D.A. Wesner, and G. Güntherodt, Phys. Rev. Lett. **65** (1990) 2058.

III. EXPERIMENTAL DETAILS

A. UHV setup

Figure 7 shows a picture of our UHV system (The University of Nijmegen, the Netherlands). This UHV system consists of a fast entry chamber, a preparation chamber and an STM chamber. These chambers are put on steel frames. The frame is designed as stiff as possible. It consists of hollow box-sections which are filled with sand to make them acoustically dead. Four pneumatic air dampers (Fill and Forget, Laminar Flow Isolator PL2000 series, Newport) are set below the system to reduce the coupling of vibrations from the floor (above 2 Hz). This floor has a very low vibration level, about 20 times less than the other basement floors in the building. (We use the former atomic shelter.) The preparation and the STM chambers are separated by a gate valve. The preparation chamber is pumped by a turbo molecular pump (Balzers 170 l/s) which is backed by a two stage rotary pomp (Edwards 5 m^3/hr). The STM chamber is pumped by an ion pump (Varian, Noble Diode 150 l/s). Also, both chambers contain titanium sublimation pumps (Varian). Using these pumps, after baking and degassing the system, the base pressure achieves 1×10^{-10} mbar for the preparation chamber and 5×10^{-11} mbar for the STM chamber. The partial pressures of residual gases were checked with a mass-spectrometer (AccuQuad 100D Kurt J. Lesker). When the pressure of the preparation chamber was 4.6×10^{-10} mbar as measured with the ionization gauge, it showed 124×10^{-11} mbar for H_2, 0.77×10^{-11} mbar for N_2, 2.0×10^{-11} mbar for CH_4, 7.2×10^{-11} mbar for H_2O, 4.7×10^{-11} mbar for CO or N_2, 0.09×10^{-11} mbar for O_2, and 2.3×10^{-11} mbar for CO_2, i.e. the main residual gas was H_2.

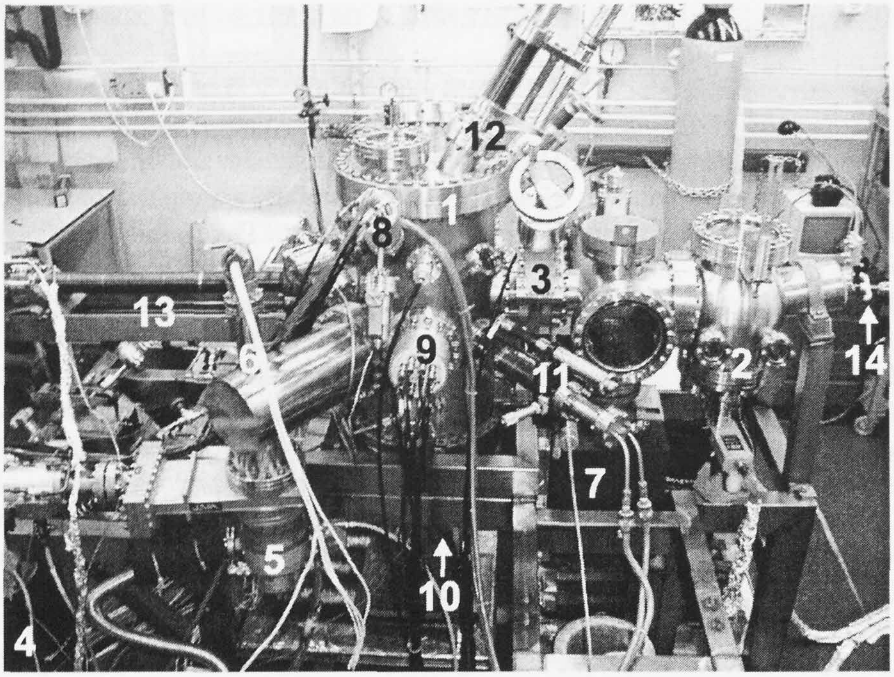

FIG. 7. Front view of our UHV system. The system comprises a preparation chamber and an STM chamber. Tips and samples are moved between both chambers by a transfer-rod. A wobble stick is used to move tips and samples from the rod to the STM head. The whole system is carried by four air dampers. 1: preparation chamber, 2: STM chamber, 3: gate valve, 4: air damper, 5: turbo molecular pump, 6: titanium sublimation pump, 7: ion pump, 8: ion sputter gun, 9: Auger electron analyzer, 10: Knudsen-cells, 11: quartz microbalance, 12: linear feedthrough with three filaments for tip heating and with field emission spectroscopy system, 13: transfer-rod with a goniometer, 14: wobble stick.

B. Preparation chamber

Except for STM/STS measurements all measurements and preparations were performed in the preparation chamber. The preparation chamber includes a transfer-rod with a goniometer (VG HPLT 50 DH) which can move about 50 cm, i.e. the sample or tip can move between the two chambers without breaking UHV. Using this transfer-rod our samples or tips were moved to the STM chamber and put into the STM head with a wobble stick.

The samples and tips were sputtered frequently by Ar^+ with a sputter ion gun (Perkin Elmer). The diameter of the ion beam was about 2 mm. The ion beam was rastered over a 10×10 mm^2 area. Roughly speaking, a sputtering rate of ~0.2 nm/min is estimated for an Fe sample using a 1 kV Ar^+ ion beam and a sputtering current of 3 μA [1]. In combination with the heating system of the manipulator the sample was sputtered at various temperatures. Usually, Ar gas (purity 99.9999 %) was introduced in the preparation chamber up to 3-5$\times 10^{-5}$ mbar. Ar gas was introduced from the bottle through a steel pipe and a variable leak valve (Varian) into the preparation chamber. Usually the pipe was pumped by another turbo-pump (Varian, 45 l/s for H_2) which is backed by a rotary pump (Vacuum Research Corporation 84 l/min). Before sputtering, pumping in the pipe was stopped and immediately the pipe was filled with Ar. The Ar pressure in the pipe was kept higher than 1.5 bar. During the sputtering mass spectroscopy detected a slight increase of the partial pressure of residual gases: 220×10^{-11} mbar for H_2, 1.3×10^{-11} mbar for N_2, 3.3×10^{-11} mbar for CH_4, 6.9×10^{-11} mbar for CO or N_2, 0.18×10^{-11} mbar for O_2, and 3.2×10^{-11} mbar for CO_2.

Auger spectroscopy (Perkin Elmer, Cylindrical Auger Electron Optics, PHI model 10-155) was used to identify different chemical species on the sample surface. A primary electron beam (2 kV, 20 μA) with a diameter of 0.1 mm was used. The typical electronic noise level is lower than 1 % of the Fe 703 eV peak in the differential mode Auger signal.

In this thesis Mn and Fe were evaporated on the sample and the tip from Knudsen cells. The evaporation sources are surrounded by a liquid nitrogen baffle which keeps the pressure during growth in the low 10^{-10} mbar range after enough degassing of the cells. For evaporating Mn and Fe we heated the K-cells up to 740°C and 1440°C, respectively. The evaporation rate was estimated by a quartz crystal microbalance (Leybold inficon): 0.07 nm/min for Mn and 0.6 nm/min for Fe. After calibrating the evaporation rate the microbalance is moved back and an Fe-whisker or a W tip is put in front of the shutter of the K-cells. By opening the shutter during a certain time a precise amount of Fe or Mn was deposited.

C. UHV-STM/STS system

All STM/STS measurements were performed at room temperature. The STM chamber includes a commercial STM (Omicron UHV STM-1), a wobble stick, and sample-carousel (eight holders can be stored.) To minimize electronic noise, the tunneling current amplifier is integrated in the STM. We use a hybrid IV converter H1 which has an input protection against voltage peaks up to ±500 V (Δt<0.1 ms) instead of the regular IV converter. It is characterized by a large bandwidth (>30 kHz) and low current noise (0.8 pA rms at 200 Hz). Furthermore, the tunneling current from the IV converter goes through a filter circuit before it is detected by the controller. A push-pull motion drive can lock the STM stage including the piezo sliders. When the STM stage is unlocked it hangs freely on four springs. These springs act as a low pass filter with resonance frequency lower than 2 Hz. Additional damping is provided by eddy current damping. Copper plates move between the permanent CoSm magnets when the STM stage is unlocked. This damping is needed to reduce the response at the resonance of the spring system. The stray field of the permanent magnets is lower than 1 Gauss at 70 mm apart from the magnets, i.e., at the tip or the sample position in the STM the stray field is lower than 1 Gauss. In our setup the electronic noise is lower than 4 pA. In this study we choose the z-gain of 1.6 pm for 1 bit. All STM/STS measurements are controlled by the commercial Omicron STM controller with the SCALA system (SPARC SUN4m) using the SPM software version V2.2.0.3. The STM piezo is used with a calibration provided by the company (Omicron), which has a sensitivity of 5.5 nm/V for x-axis, 5.9 nm/V for y-axis and 7.3 nm/V for z-axis. Figure 8 shows images viewed from the top (a) and the side (b). Figure 8(c) shows a tip and a Ta sample holder with an Fe whisker, which was obtained from the top with a CCD camera.

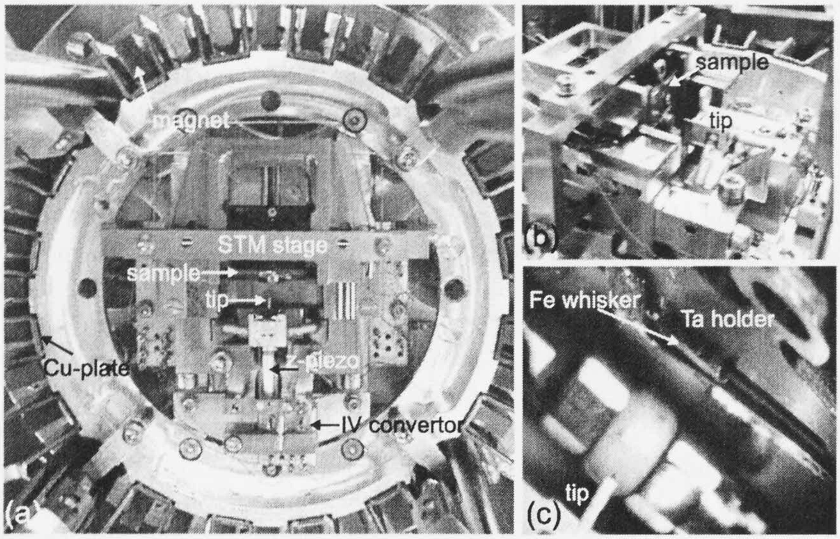

FIG. 8. Top (a) and side view (b) of the UHV-STM (Omicron 1). (c) Top view obtained by a CCD camera. An Fe-whisker is mounted on the Ta holder. The tip is also observed. The tip diameter is 0.5 mm.

D. Sample preparation

All sample preparation was performed on the manipulator. This manipulator can accept the commercial Omicron Ta plate holder by clamping it with Mo leaf springs (Fig. 9(a)). The Ta plate holder was modified to mount the Fe-whisker. This holder can be indirectly radiatively heated by a thoria-coated tungsten filament (VG), which is 1 mm behind the holder. Since the holder and the filament are isolated, −900 V can be applied to the filament while the holder is grounded. This high voltage is needed to accelerate the electrons to reach a higher temperature. In this way, the holder can be heated higher in temperature by direct electron bombardment. The temperature is detected by two Pt-10%PtRh thermocouples (arrows in Fig. 9(a)). Since the thermocouples are not directly contacted to the holder, the temperature on the holder was calibrated by a pyrometer (IRCON RADIATION THERMOMETER Series 300c). Figure 10(a) shows temperatures detected by the thermo couples (black curve) and by the pyrometer focused at the center of the sample (grey curve) when the sample was heated radiatively (without applying the high voltage). At nine minutes, the heating was switched off, then the temperature starts to decrease. The temperature at the center of the sample is about 1.5 times higher than at the thermo-couple position. The temperature of the thermocouple (far from the center) follows the temperature of the pyrometer (at the center). In this thesis, during sample preparations, the sample temperature was detected by the thermo-couples. Figure 10(b) shows the sample temperature measured by the pyrometer as a function of the sample temperature measured by the thermocouples. The triangles were obtained when the sample was heated radiatively. The black and grey dots were obtained when the sample was heated by electron-bombardment (applying the high voltage). The grey dot was obtained with another pyrometer (Minolta Cyclops 52). The radiative heating can increase the sample temperature only up to 550 K. Using the electron-bombardment heating the Fe-whisker sample can be heated up to 1020 K. During the cleaning of the Fe-whisker with Ar sputtering, the whisker was heated at 1020 K. The limitation of this temperature is the martensitic-austentitic phase transition in the Fe-C phase diagram, which occurs at 996 K for a carbon weight concentration of 0.8 % but increases to 1183 K for zero carbon concentration. Above this phase transition α-Fe (which has a bcc structure) transforms to γ-Fe (which has a fcc structure).

To obtain a clean and flat substrate surface, an Fe(001)-whisker was used in this study [2]. Using Ar sputtering (750 eV) cycles between RT and 1020 K, the Fe(001)-whisker, with dimensions $7 \times 0.5 \times 0.5$ mm^3, was cleaned until the concentration of surface contaminants became lower than 1% as measured by Auger spectroscopy and atomically resolved STM images. From the Auger spectroscopy the contaminant was identified as oxygen.

Figure 9 shows our sample holder for the Fe whisker. The Fe whisker is fixed by a Ta leaf spring as shown in Figs. 9(b) and 9(c). The first version sample holder fixed both sides of the Fe whisker (Fig. 9(b)). The spring was fixed by a screw. Then, after several heating treatments, the Fe whisker was deformed and many scratches were observed (Fig. 9(d)). Then, we made the second version sample holder (Fig. 9(c)). A channel (0.5 mm wide and 0.3 mm deep) was made on the Ta sample holder. This channel fitted to the Fe whisker. The Fe whisker was fixed only at one side and the spring was spot-welded to the Ta holder. The Fe whisker was able to expand during the heating along the long axis of the Fe whisker. We observed a drift in STM measurements along the long axis (0.1 nm/min at 12 hours after the preparation of the Fe whisker).

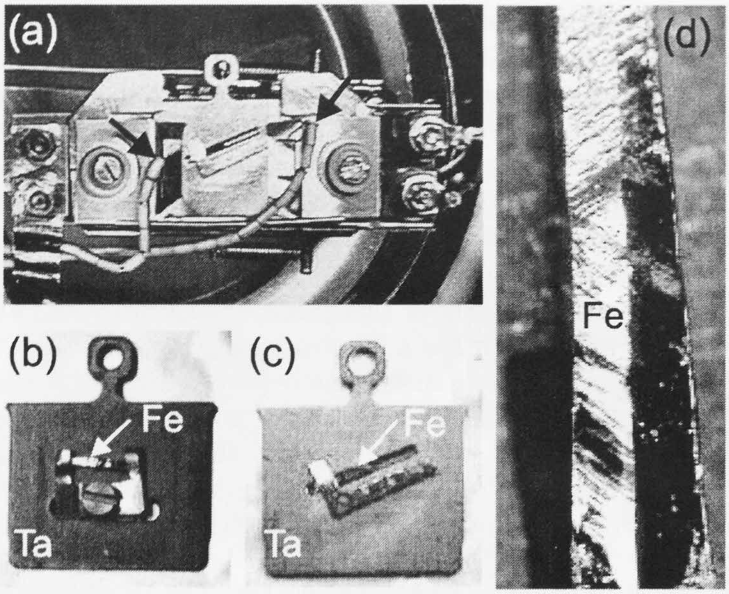

FIG. 9. (a) shows the manipulator head holding the Ta sample holder with an Fe whisker. Arrows mark the two thermocouples. (b) First version of sample holder. An Fe-whisker was fixed at both sides by Ta strips. (c) Second version of sample holder. An Fe whisker was put in the channel and was fixed at only one side by a Ta strip. (d) Fe whisker, which was used in (b). By repeated heating and cooling the Fe-whisker surface was deformed.

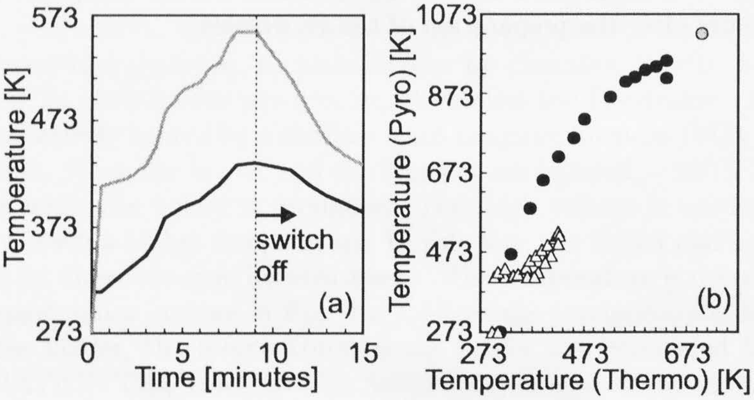

FIG. 10. (a) Variation of the temperature of the Ta sample holder as a function of time as measured by the pyrometer (grey curve) and the thermocouple (black curve). Since the thermo-couple is not directly in contact with the holder, about an 1.5 times difference is observed between them. (b) The temperature measured by the pyrometers as a function of the temperature measured by the thermocouples. The triangles were obtained when the sample was heated radiatively (without high voltage). The black and grey dots were obtained when the sample was heated by electron-bombardment heating (applying high voltage).

Mn (purity 99.999 %) was sublimated from a Knudsen cell at a deposition rate of ~0.3 ML/min as estimated by a quartz crystal oscillator. Here, one ML is defined as one Mn atom per Fe atom on the (001) surface. In the present thesis, the local Mn coverage is obtained from a Gaussian fit to the distribution of exposed layers (see Fig. 19(a)). During the growth, the pressure was always around 4×10^{-10} mbar. The substrate was radiatively heated to 370 K. Growth at this temperature is believed to lead to reasonable flat films [3] and low intermixing [4].

E. Tip preparation for STM/STS

To observe atomically resolved topographic images, it is common to use a sharp W tip since a sharper tip can increase the lateral resolution. A rough estimation of the lateral resolution can be described as follows [5]: $\Delta x = \sqrt{2(R+d)}$, where R is the radius of the tip apex, d is the tip-sample distance. When d = 10 Å and R = 100 Å, Δx = ~15 Å is obtained. When d = 10 Å and R = 10 Å, Δx = ~6 Å is obtained [6] .

In chapter IV of this thesis sharp W tips are used. For getting a sharp STM tip, a W polycrystalline wire with a diameter of 0.5 mm (purity 99.99 %) was etched with a 5M KOH solution and subsequently rinsed with ethanol in air. In UHV, the tip was heated up to 1000 K. The tip was heated by a direct contact of the filament to the tip (Fig. 11(a)). The tip was self-sputtered with Ar (or Ne) in order to clean the tip and to decrease the tip radius [6]. The self-sputtering was performed as follows. The tip was brought about 5 mm under the metal ball. Around 1×10^{-4} mbar Ar gas was introduced into the preparation chamber. We applied positive voltages to the ball (the tip was grounded). The voltage was modified to keep the Ar^+ sputter current at 10 μA. Since the density of the electric field is higher near the tip apex, ions focus to hit the tip apex which sharpens the tip apex. A sketch of the self-sputtering is shown in Fig. 11(b). A lower voltage is needed to sustain a constant current of 10 μA. Since the Ar ions sputter effectively the sides of the tip apex, a neck is formed. Finally the tip apex drops off. By recording the voltage variation we can see a sudden drop of the voltage caused by the drop of the tip apex. At this moment we immediately stop the self-sputtering. After the self-sputtering the tip radius is below 10 nm as verified by field-emission spectroscopy. The field emission spectroscopy was measured with the same setup as the self-sputtering. The field emission current was detected by a home-made IV converter (1 nA/V). The sketch of the setup is shown in Fig. 12(a). The field emission current was measured by gradually applying a positive voltage to the metal ball from 0 V to 3000 V (typically 10 V/sec). The field emission current increases at a particular voltage as shown in Fig. 12(b), which is mainly

---

[6] If the Heisenberg's uncertainty principle predicts an uncertainty in position which is larger than atomic scale, we cannot get an atomic scale resolution in the STM/STS. In the tunneling regime, the momentum is given by $p = \sqrt{2m(V_o - E)}$, where V_o and E denote the vacuum level and the energy of the electron, respectively. If the uncertainty of momentum (Δp) is larger than $\sqrt{2m(V_o - E)}$, electrons tunnel. Then, $\Delta x \sim \hbar/2/\sqrt{2m(V_o - E)}$. If $(V_o - E)$ (=work function) is 4 eV, Δx is 0.5 Å.

determined by the tip-radius (the noise level was ±0.1 nA). When we varied the tip-ball distance ±2 mm the onset voltage was shifted about 200 V. This shift is much smaller than the shift caused by different tip radii, i.e. ~300 V at 1 nA for a tip with a radius of 10 nm and >3 kV for a tip with a radius of 300 nm. By using a fit of the field emission current formula [7] to the experimentally obtained curve, I can estimate the tip radius [6].

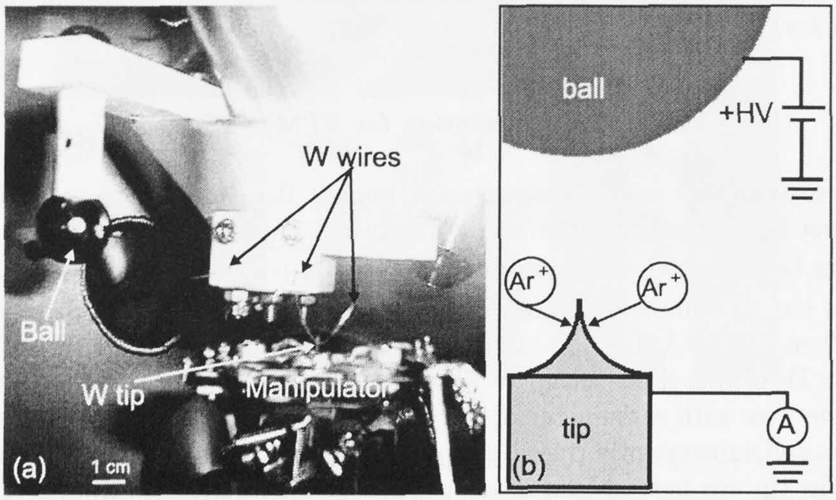

FIG. 11. (a) shows the field emission spectroscopy setup in our preparation chamber. By contacting a W wire to the tip on the manipulator, the tip can be radiatively heated. (b) shows the scheme for self-sputtering. Using the setup in Fig. 11, positive high voltages (+HV) are applied to the ball. By introducing Ar$^+$, the tip apex is sputtered. During the self-sputtering the sputtering current is monitored and kept at 10 μA by a constant current power supply. By monitoring the variation of the high voltage, the self-sputter is stopped when a sudden drop of the voltage is observed. At that time, the tip apex breaks off at a "neck" position and a clean and sharp tip apex is fabricated.

---

[7]

$$\begin{aligned} J &= 1.537 \times 10^{14} \frac{E^2}{\Phi t^2} exp\Big[-\frac{0.683\Phi^{3/2}}{E}x\Big], \\ x &= 1.0029 - 0.1177y + 1.1396y^2 - 0.2561y^3, \\ t &= 0.9967 + 0.0716y + 0.0444y^2, \\ y &= 3.79\sqrt{E}/\Phi, \\ E &= 0.368 \frac{V(1 + 0.00425\alpha - 0.137\alpha^2)}{r^{0.9}(R^{0.1} - 0.75r^{0.1})}, \end{aligned}$$

where V is the applied voltage, J the density of the field emission current, α the angle from the tip axis, r the tip radius, R the tip-sample distance and Φ the average work function. By integrating J over the entire frontal hemisphere of the tip the total field emission current is obtained.

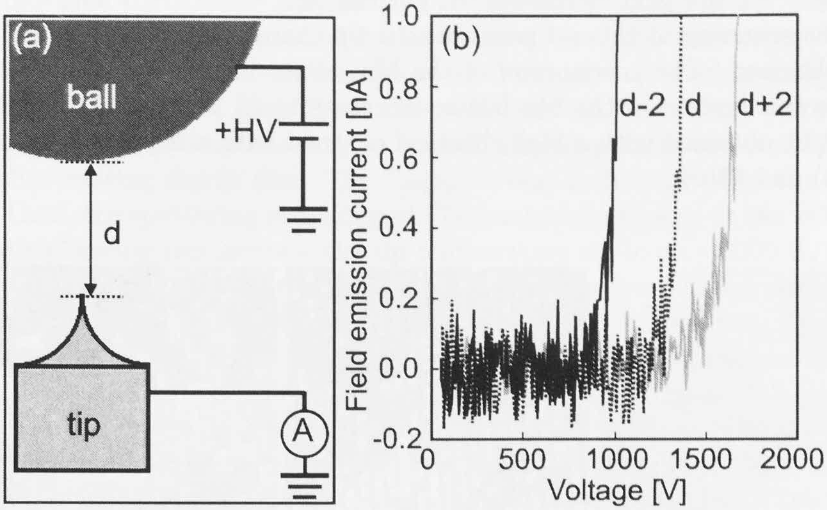

FIG. 12. (a) shows the scheme of a field emission spectroscopy measurement. "d" denotes the tip-ball separation. Positive bias voltages are applied to the metal ball while the tip is grounded. (b) shows the field emission current as a function of positive bias voltage for three different tip-ball distances. These measurements were performed with the same setup as (a) but without introducing Ar. The current depends on the tip-ball separation. When the separation becomes smaller, the onset voltage of the current shifts toward lower voltage.

When the W tip comes close to the sample (resistance $< 10^6\ \Omega$) atomic corrugation can be observed. The atomic corrugation becomes higher when the tip is brought closer to the sample since the atomic corrugation can be described as $\Delta z \sim (2/\kappa)exp[-2(\sqrt{\kappa^2 + (\pi^2/a^2)} - \kappa)z]$ where κ is the inverse decay length, a the sample lattice constants, z the tip-sample separation [7]. With a normal tip condition [8] the corrugation of the lattice atoms is about 1-5 pm. Consequently, the atoms can hardly be observed in the topographic image. Fortunately, occasionally special tip conditions could be obtained during STM measurements, e.g., the corrugation of the Fe atoms increases to more than 10 pm, which is likely caused by strong tip-sample interaction (or strong force between tip and sample [8,9]). With special tip conditions a high chemical contrast can be achieved which is utilized in determining the intermixing behavior. As an example, several atomically and chemically resolved STM images are shown in Fig 13, which were observed at the same area on 1 ML Mn surface grown on Fe(001) at 370 K. The three images were obtained with the same W tip. The first Mn layer follows the p(1×1) structure of the substrate and includes intermixed Fe atoms with a concentration of 14 % (contaminants with a concentration lower than 1 % are also included.). To increase the atomic corrugation, the tip was brought closer to the sample by decreasing the bias

---

[8] Normal refers to the higher chance of having this kind of tip compared to a tip leading to chemical contrast.

voltage to $V_S = -2$ mV and increasing the current to $I = 2.6$ nA. First, Fig. 13(a) was obtained. The scanning at this set point caused tip-changes and images Figs. 13(b) and 13(c) were obtained. The corrugation of the Mn lattice in Fig. 13(a) is about 1-5 pm. However, the corrugation of the Mn lattice increases to 35 pm and atomically resolved images could be obtained with a high chemical contrast with a depth of 60 pm as shown in Figs. 13(b) and 13(c).

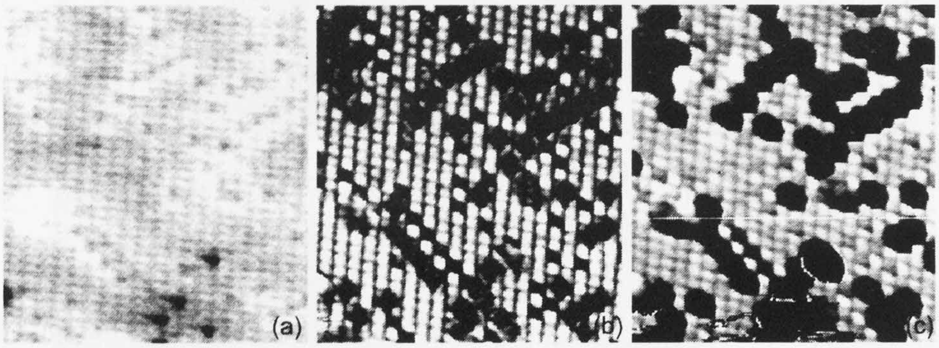

FIG. 13. Atomically and chemically resolved STM images. Images were obtained with the same W tip at exactly the same sample surface area on the 1 ML Mn grown on Fe(001) at 370 K (6.5×7.0 nm^2, $V_S = -2$ mV, $I = 2.6$ nA). Different observations between the images of (a)-(c) are caused by tip changes (a strong tip-sample interaction).

F. Tip preparation for SP-STM/SP-STS

Although there were several candidates for a magnetic tip, finally, it was decided to make a ferromagnetic Fe-coated W tip. Since all preparation was performed in UHV, the tip includes a low concentration of contaminants (<1%). Also, the tip coated by the thin film has a much smaller stray field compared to tips made of magnetic-material rods.

First, we made a clean and sharp W tip with heating and self-sputtering. Second, a 2-10 nm Fe film was deposited on the W tip at RT in UHV (below 2×10^{-10} mbar, 0.6 nm/min) without applying external magnetic field. Although we prepared the Fe-coated W tips in this way, we never detected spin-polarized tunneling current after the first approach. We changed the thickness of the Fe film and the evaporation rate, but the spin-polarized current was not detected. Annealing up to 600 K after Fe was deposited did not help.

After many trials we thought the problem of our tip is as seen in Fig. 14(a), i.e. the magnetization direction of our tip is not parallel to the sample magnetization direction. After heating, the W tip apex exposes a (110) plane. The Fe films grown on the W(110) were reported to have an in-plane anisotropy. Then, we decided to change the sharp W tip with a radius of 5-50 nm to a blunter tip. The tip radius was measured with field emission spectroscopy. Using Ar$^+$ sputtering and heating, the W tip apex was cleaned and the tip radius was controlled. To make a clean and blunt W tip, in UHV, the tip was sputtered with the sputter ion-gun (1 kV) instead of using the Ar^+ self-sputtering setup and was subsequently heated. Usually we monitored the sputtering current when sputtering. The following behavior was observed. First, the sputtering current gradually decreases [from 3.3 μA to 1.7 μA]. Then, after ~45 minutes, it suddenly increases again [3 μA] (see Fig. 14(c)). (The tip showing no "jump" also frequently detected spin-polarized tunneling after coating the Fe film. The "jump" seems to be related to the shape of the tip apex.) Then, the sputtering was stopped. This might be similar to the self-sputtering. Since radiative heating can increase the tip temperature up to only 1000 K, which is not enough to make the tip blunter, the tip was heated by electron-bombardment. Although the same W wire shown in Fig. 11(a) was used, instead of direct contact to the tip, the wire was put about 5 mm above the W tip apex and the tip was applied high voltages. Then, the tip was heated for 2-5 minutes by electron bombardment (42 W). After this heating, the radius of the W tip increased by more than 200 nm, which was estimated by field emission spectroscopy. Even macroscopically the difference could be seen (inset image in Fig. 14(c)). Finally, a W tip with a tip radius of more than 200 nm coated by 2-10 nm Fe at RT was found to detect the spin-polarized tunneling reproducibly without applying external magnetic field, i.e. the tip magnetization direction is believed to be parallel to the sample magnetization direction as shown in Fig. 14(b) [10]. During the Fe evaporation the pressure remained below 2×10^{-10} mbar. The evaporation rate was 0.6 nm/min. Furthermore, no voltage pulses were applied during these SP-STS measurements [11]. The tip was carefully approached to the sample to exclude any mass transport between tip and sample. Since the magnetic contrast depends on the factor $\cos\theta$, where θ is the angle between the in-plane magnetization directions of the Fe-coated W tip and the Mn layers, the magnetic contrast is always observed except for the case that the tip magnetization is exactly orthogonal to the sample magnetization. The tip magnetization direction is randomly orientated with respect to the magnetization direction of the Mn layers and is different from tip to tip. When SP-STS shows the highest magnetic contrast, the magnetizations of the tip and the sample are believed to be nearly (anti)parallel. We prepared more than 50 different Fe-coated W tips and measured spin-dependency in SP-STS. In this thesis, the SP-STS data which show the highest magnetic contrast are used.

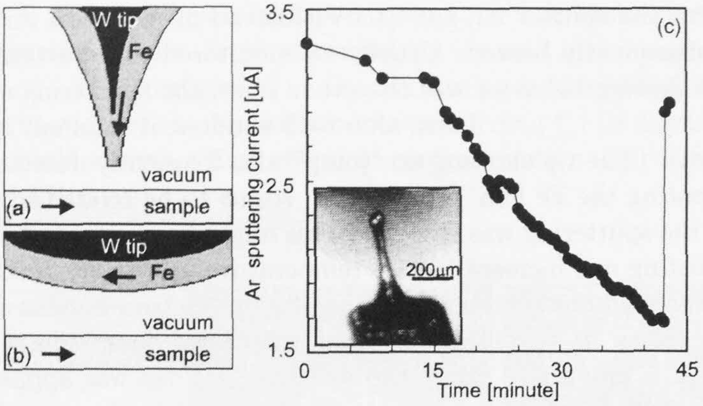

FIG. 14. (a) and (b) show sketches of the magnetization of the Fe films on the sharp and the blunt W tips, respectively. Arrows denote the magnetization directions. (c)The Ar^+ sputtering current was recorded during the time in which a W tip was sputtered (1 kV, 3.5×10^{-5} mbar). The inset image obtained by a CCD camera shows the tip apex of a sputtered and electron-bombarded W tip.

Figure 15 shows field emission microscopy (FEM) measurements, which were performed in another UHV chamber at room temperature (Gakushuin University, Japan). The base pressure of the chamber is lower than 4×10^{-9} mbar. (Unfortunately, due to the limit of the equipped ion-gauge, the pressure lower than 4×10^{-9} mbar could not be measured.) The field emission current was typically detected up to 100 μA (3 kV) to get FEM images. The FEM image was observed on a fluorescent screen, which was recorded by a CCD camera. Our FEM setup shows a magnification of about 10^6 [9] . During the FEM measurements the tip pointed to the screen. For getting an STM tip a W polycrystalline wire with a diameter of 0.3 mm (purity 99.99 %) was etched with a 2N NaOH solution and subsequently rinsed with ethanol and 2 % HF in air. Subsequently, in UHV, the W tip was heated up to ~2000 K and cooled down to room temperature. Then, Fe (purity 99.98 %) was sublimated on the W tip at RT from an Fe powder by electron bombardment (4 kV) at a deposition rate of 0.7 nm/min as estimated by a quartz crystal oscillator. During Fe deposition the pressure was lower than the detectable limit of the ion-gauge and the W tip pointed to the Fe K-cell.

Figure 15(a) shows our FEM setup. The picture shows the inside of the chamber. Figure 15(b) shows FEM images. A typical image obtained from the annealed W tip shows four bright spots on the screen, where one spot is almost out of the screen. The dark square inside the bright spots corresponds to the W(110) and the bright spots indicate (111) and (100) or (130) faces as shown in Fig. 15(b-1), which were identified from the shape of different faces [14]. With the magnification of 10^6 and the size of the W(110) area on the screen (1x1 cm^2), the area of the (110) face on the tip apex is estimated around

---

[9] The tip-screen separation (d) was 10 cm. If the tip has a 100 nm radius (r), the magnification can be obtained by r/d, i.e. 10^6 [13].

10x10 nm^2. The work functions of (110), (100), and (111) are 5.25 eV, 4.63 eV, and 4.47 eV, respectively [15]. Figures 15(b-2) and 15(b-3) are FEM images of one of the (111) face spots before and after depositing 7 nm Fe, respectively. The sharp spots became blunter after the deposition, which indicates that the Fe film does not have ordered structures (it might be an amorphous-like disordered structure). Figure 15(c) shows the intensity of the bright spots as a function of the voltage. The results obtained at two different (111) spots on the screen are shown as black and grey dots, which shows that the intensity start to increase around 2000 V, while the intensity of the (100) spot starts to increase around 2200 V (triangles). This is caused by different work functions.

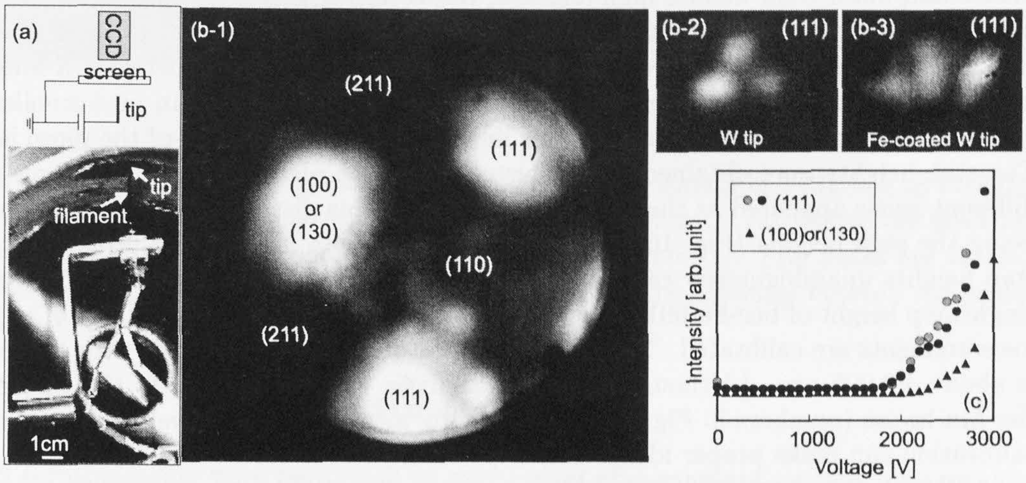

FIG. 15. (a) shows our FEM setup. The picture shows the inside of the chamber. (b-1) FEM image obtained from a W tip. (b-2),(b-3) FEM images around the (111) face before and after depositing Fe. (c) shows the intensity of the spots in the FEM image as a function of the voltage. Black and grey dots are obtained at spots of a different (111) face. Triangles are obtained at the (100) face.

G. STM measurement

Before STM/STS measurements, the turbo pumps (and rotary pumps) were switched off to reduce vibrations. The tip was approached to the sample in two steps. The first step is a course approach. Since our Fe whisker sample is small (maximum width is 1 mm), it is difficult to bring the tip exactly on the Fe whisker. Thus, the tip is brought closer until the reflection of the tip was observed on the Fe whisker surface by monitoring with a CCD camera with magnifier. Although the noise current was usually lower than 4 pA, the tip sometimes detected a leakage current (5-100 pA) due to the mechanical contact between the sample holder and the STM stage. This problem was solved by moving the sample holder properly. The second step is an auto-approach controlled by the STM controller and software. The set point during the auto-approach was typically $V_S = -1$ V and $I =$ 0.05 nA. Then, the tip was moved towards the sample by superimposing a linear ramp to the z-piezo. The speed of this ramp can be selected by the controller. When a tunneling current was detected, the auto-approach is stopped. At this position we started to scan and checked whether drops or crashes occurred during the approach.

The tip can be moved on the surface by x- and y-axis piezo scanners. The tip-sample separation is varied by a feedback loop to keep a constant current. By detecting the variation of the z-piezo from pixel to pixel a map is displayed on the computer screen. This image is called STM topographic image. The experimentally obtained STM topographic image includes a drift since the sample surface is not completely parallel to x,y scan directions. Usually the distortion in the image was removed by a plane-fitting as shown in Fig. 16(a). In this thesis grey scale reveals a height difference on the sample surface. White and black color denote high and low, respectively. When the sample surface has a homogeneous electronic structure, this STM topographic image shows the real geometric structure of the sample surface. To obtain the interlayer distance between a lower and a higher layer, step heights were measured with clean W tips. A scan area smaller than 100×100 nm^2 was used since only for this limited area the sensitivity of the piezo is valid. The step heights were obtained from a histogram of the plane-fitted STM images, where different levels appeared as sharp Gaussian peaks in this distribution with their spacings being the step heights (Fig. 16(b)). Only sharp Gaussian distribution profiles for which step heights unambiguously can be defined were included in the analysis. Using the Fe single step height of bcc-Fe(001) which is 0.143 nm, the apparent step heights of our STM measurements are calibrated. The accuracy of the step heights obtained with this process is about ±0.005 nm. (Although from this analysis we cannot identify the thickness of the Mn layers (numbers in Fig. 16), spectroscopy measurements as well as quartz crystal calibration can make proper identification possible.)

Although the apparent step heights were not influenced by the set point current, the heights in the topographic images obtained at different set point voltages show differences when a lower and a higher layer have a different DOS or a different work function. To exclude these electronic influences the apparent step heights obtained at set point voltages below the Fermi energy are used to extract the interlayer distance since at negative voltage the electronic structure of the tip dominates (see Chapter II) and is the same on different sample terraces. The experimentally obtained results are shown and discussed in chapter IV. If the step height measurements as a function of the sample bias voltage obtained with Fe-coated W tips show differences from those obtained by clean W tips, this must be caused by spin-polarized tunneling.

Typically, when we obtain STM topographic images of more than 30×30 nm^2 we chose a tunneling resistance higher than 10^9 Ω, e.g., $V_S = -0.5$ V and $I = 0.5$ nA to avoid a contact or a strong interaction between tip and sample. When we want to obtain atomically resolved STM images we choose the area smaller than 30×30 nm^2 and bring the tip closer to the sample by decreasing the tunneling resistance down to 5×10^7 Ω, e.g., $V_S = -2$ mV and $I = 25$ nA. Two orders of magnitude difference in the resistance only varies the tip sample distance by about 0.2 nm.

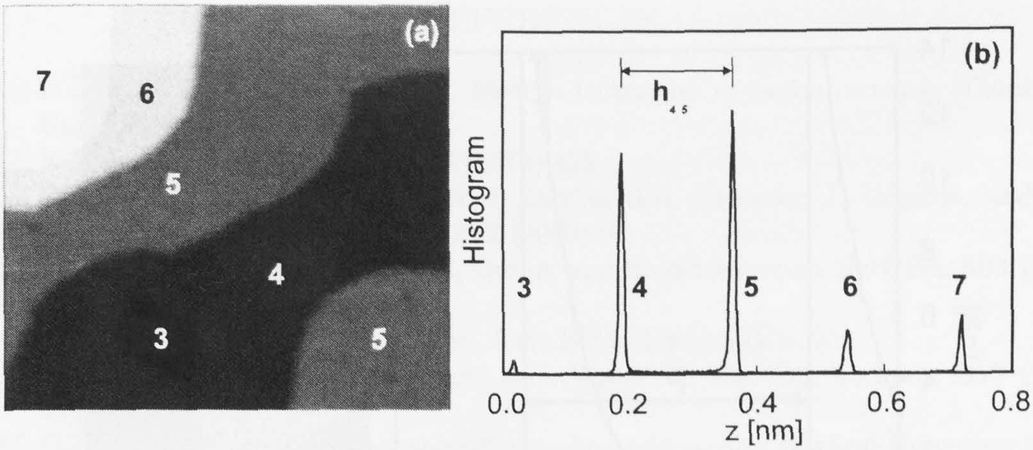

FIG. 16. (a) is an STM topographic image obtained on the surface of 5 ML Mn on Fe(001) at 370 K. $V_S = -0.5$ V and $I = 0.5$ nA, 39×35 nm^2. Numbers in (a) denote the stacking numbers of the Mn layers. (b) shows a histogram obtained from (a). Five peaks are visible, which represent the different Mn layers in (a). By measuring the distances between the peaks the apparent step heights between Mn layers can be obtained.

H. STS measurement

STS measurements were performed at every pixel of a constant current topographic image by opening the STM feedback loop at a typical set point of $V_S = -0.5$ V, $I = 0.5$ nA since this set point is believed to avoid a tip crash or strong tip-sample interaction. In this study an $I(V)$ curve was recorded at each pixel within a voltage range, typically, from -1 V to $+1$ V with a voltage step of more than 25 mV, which value corresponds to k_BT at RT (k_B and T denote the Boltzmann constant and the temperature, respectively). dI/dV curves were obtained by numerical differentiation of the $I(V)$ curves. Figure 17 shows a typical example of our STS measurement, where we choose 100×100 pixels (1 nm/pixel) and obtain the tunneling current (I) from -1 V to $+2.5$ V with a 25 mV voltage step (i.e., 140 points). Figure 17(a) shows the variation of the tunneling current monitored with an oscilloscope as a function of time during the STS measurement. During the period "P" (about 100 ms) the tip stays at one pixel position. During the period "A_1" (around 20 ms) the feedback is working and the tip approaches or retracts to keep the constant current, then topographic information is recorded. After period "A_1" the feedback is opened and the tunneling current as a function of sample bias voltage is measured (period "B_1": around 80 ms). Then, the feedback is switched on again and the tip moves to the next pixel position and during "A_2" topographic information is obtained. The same process is repeated for 100×100 pixels (typically it takes 10-20 minutes). Therefore, we can get a topographic image (Fig. 17(b)) and a spectroscopic image (Fig. 17(c): a dI/dV map at $+0.2$ V) at the same time.

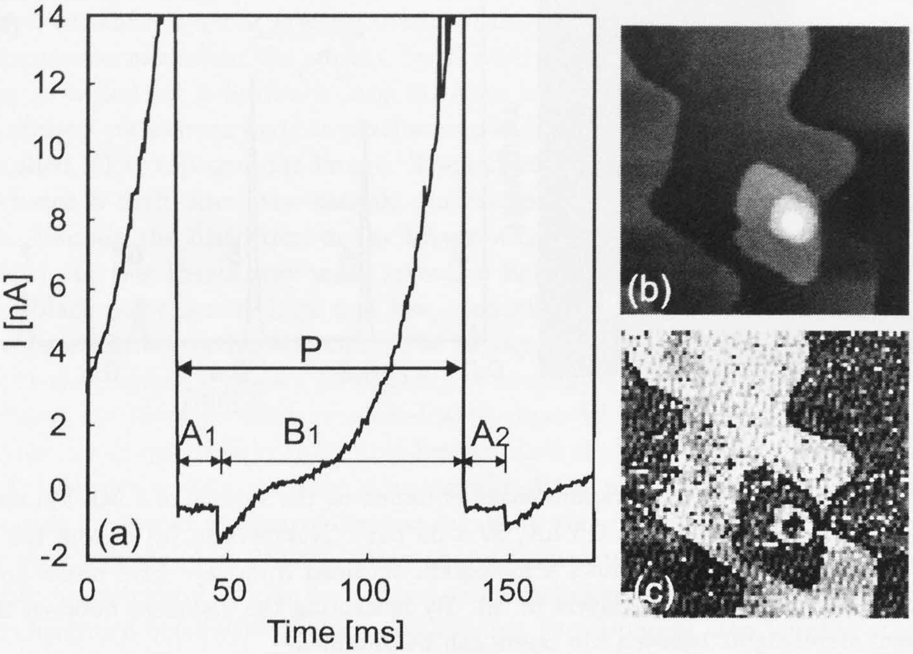

FIG. 17. (a) shows the tunneling current as a function of time obtained from -1 V to $+2.5$ V at a set point of $V_S = -0.6$ V, $I = 0.4$ nA. A tip stops at one pixel position during "P". During "A_1" the tunneling current is kept constant by closing the feedback loop to store topographic information. Then, during "B_1" the feedback loop is opened. The tunneling current is measured as a function of the sample bias voltage, i.e. spectroscopic information is obtained. After this information is obtained, the feedback loop is closed again and the tip moves to the next pixel position. In this way I obtained STM and STS information at the same time. As an example, an STM (70×70 nm^2, -0.5 V, 0.5 nA) and an STS image (a dI/dV map at $+0.1$ V) shown in (b) and (c), respectively, were obtained at the same time on the surface of 6 ML Mn on Fe(001) with an Fe-coated W tip.

REFERENCES

[1] D.P. Woodruff and T.A. Delcher, *Modern techniques of surface science*, (Cambridge University Press, U.K., 1986).
[2] R.N. Gardner, J. Crys. Grow. **43** (1978) 425.
[3] D.A. Tulchinsky, D.T. Pierce, A.D. Davies, J.A. Stroscio, J. Unguris, and R.J. Celotta, J. Magn. Magn. Mater. **212** (2000) 91.
[4] M.M.J. Bischoff, T. Yamada, A.J. Quinn, and H. van Kempen, Surf. Sci. **501** (2002) 155.
[5] J. Tersoff and D.R. Hamann, Phys. Rev. B **31** (1985) 805.
[6] G.J. de Raad, P.M. Koenraad, and J.H. Wolter, J. Vac. Sci. Technol. **B17** (1999) 1946.
[7] C.J. Chen, Introduction to scanning tunneling microscopy, (Oxford University Press, Oxford, U.K., 1993).
[8] J.M. Soler, A.M. Baro, N. Garcia, and H. Rohrer, Phys. Rev. Lett. **57** (1986) 444.
[9] M. Salmeron, D.F. Ogletree, C. Ocal, H.-C. Wang, G. Neubauer, W. Kolbe, and G. Meyers, J. Vac. Sci. Technol. B **9** (1991) 1347.
[10] R. Wiesendanger and M. Bode, Solid State Commu. **119** (2001) 341.
[11] In order to reshape or clean the tip voltage pulses (±10V) were sometimes applied between the tip and the sample. These pulses likely lead to mass transport from the sample to the tip [12].
[12] T.K. Yamada, M.M.J. Bischoff, T. Mizoguchi, and H. van Kempen, Appl. Phys. Lett. **82** (2003) 1437.
[13] R. Gomer, Surf. Sci. **70** (1978) 19.
[14] M.F.H. van Tol, F.A. Hondsmerk, J.W. Bakker and B.E. Nieuwenhuys, Surf.Sci. **266** (1992) 529.
[15] J. Hölzl, F.K. Schulte, and H. Wagner, *Workfunction of metals*, (Springer-Verlag, Berlin, 1979).

IV. INTERMIXING, GEOMETRIC AND ELECTRONIC STRUCTURES ON MN/FE(001)

In this study Mn films grown on Fe(001)-whiskers were used. To extract and study magnetic properties of the Mn films by SP-STM/SP-STS, it is very important to know the intermixing behavior of Fe into the Mn films, the geometric structure, and the electronic structure of the Mn films. Without knowledge of the geometric and the electronic structures of the Mn layers the obtained features cannot be uniquely ascribed to magnetic properties.

Already many experiments were performed for Mn layers grown on Fe(001). With reflective high energy electron diffraction, quantitative low energy electron diffraction (LEED), and extended x-ray absorption spectroscopy (EXAFS), it has been shown that Mn layers grow layer-by-layer on Fe(001) up to more than 10 monolayers. The in-plane lattice constant is 0.287 nm and interlayer spacings of 0.130 [1] or 0.148 nm [2] for 1 ML, 0.152 nm [2] for 2 ML, and 0.161 nm [1] or 0.164 nm [3] for 14-25 ML are reported, i.e., the structure is body-centered-tetragonal (bct). These results have been reported for Mn growth on an Fe(001)-single-crystal at RT [1], on Fe(001)-films/MgO(001) at RT [2], and on an Fe(001) whisker at 320 K [3]. Auger electron spectroscopy and grazing ion-surface scattering measurements showed that a layer-by-layer Mn film changes to a layer-plus-island Mn film when a 13 ML thick Mn film, which is deposited at RT on an Fe(001)-single-crystal, is annealed at 420 K [4]. Nonas *et al.* showed with a Korringa, Kohn, and Rostoker Green's function method calculation that for Mn atoms on Fe(001) it is energetically favorable to place exchange with the Fe surface atoms [5,6]. Bischoff *et al.* showed with chemically resolved STM and STS images the formation of a surface alloy for sub-ML Mn films grown on Fe(001) at substrate temperatures above 370 K [7]. Grazing ion-scattering experiments showed that Fe atoms intermix with Mn adlayers up to a coverage of 3 ML at a substrate temperature of 420 K [8].

Regarding these results, Mn films were decided to grow at 370 K for the following reasons: (1) A surface which exposes several Mn layers is needed to investigate whether each Mn layer has an in-plane magnetization and couples antiferromagnetically with Mn layers below and above. The film will grow in layer-plus-island mode at 370 K. (2) Pure Mn layers are needed to study the magnetic properties of the Mn films since intermixed Fe atoms strongly influence the magnetic properties of Mn. A temperature of 370 K will restrict intermixing to the first few layers.

In this chapter, the degree of intermixing, and the geometric and the electronic structures of Mn layers on the Fe(001) whisker are studied by means of STM/STS studies with clean W tips.

A. The growth of Mn layers on Fe(001)

Monoatomic steps can be observed with an interval of about 200 nm on the clean Fe(001) whisker (Fig. 18(a)). When 1.5 ML Mn is deposited at a substrate temperature of 370 K, Mn grows layer-by-layer. This follows from Fig. 18(b) in which it can be seen that the second layer islands have started to grow after the first layer has been completed. At a coverage of 3 ML, the second, the third, and the fourth layer are observed as trenches, terrace, and islands, respectively (Fig. 18(c)). Before the second layer has been completely covered by Mn, the fourth layer has started to grow which means that the growth mode is not layer-by-layer anymore. At coverages above 3 ML, the appearance of the surface changes drastically and many levels are exposed on the surface (Fig. 18(d)). Whereas, up to a coverage of 6.5 ML Mn, hidden Fe steps are clearly observed on the Mn(001) surface as about 0.02 nm high steps, the Fe step height of 0.143 nm is never observed, which means that the overlaying Mn film tends to make the surface flat. Three dimensional (3D) islands ($\sim$5 nm high) are observed at the position of hidden Fe steps and defects marked by the white arrow in Fig. 18(e). Figure 18(e), which is displayed in the differential mode, shows that the islands have pyramid-like shapes (see also Fig. 19(c)) which corresponds to the results reported by Pfandzelter *et al.* [4].

Pierce *et al.* found that the distribution of the exposed layers can be approximated by a Gaussian. The center of the Gaussian gives the average coverage, and the deviation σ the root-mean-square height variation or roughness [9,10]. Thus, σ can be obtained from our STM images (Fig. 19(a)). σ is 0.40$\pm$0.05 ML and 0.7$\pm$0.1 ML for coverages below and above 3 ML Mn, respectively. If the layer-by-layer growth continued for coverages above 3 ML, we do not expect an increase of σ. However, σ drastically increases by a factor of two at coverages above 3 ML in our experiments, which is a clear indication that the growth mode changes. Furthermore, starting from around a coverage of 3 ML Mn, the number of 3D islands strongly increases as can be observed in Fig. 19(b). The density of the 3D islands at a coverage of around 5 ML Mn ($\sim 10^{10}$ cm^{-2}) corresponds with the results reported by Pfandzelter *et al.* [4]. Based upon both the increase of σ and the appearance of 3D islands, the critical coverage where the growth mode changes from layer-by-layer to layer-plus-island is estimated to occur around 3 ML.

The layer-plus-island growth can be understood by equilibrium thermodynamics [4,11,12] which state for the Mn/Fe system that if $\Delta\gamma = \gamma_{\mathrm{Mn}} + \gamma_{\mathrm{in}} + \gamma_{\mathrm{s}} - \gamma_{\mathrm{Fe}}$ is negative (positive), the layers grow layer-by-layer (layer-plus-island). γ_{Mn} and γ_{Fe} are surface energies of Mn and Fe, respectively. γ_{in} is the interface energy and γ_{s} is the strain energy. The Fe surface energy ($\sim$ 2.6 J/m^2) is higher than the Mn surface energy ($\sim$ 1.6 J/m^2) [13] and the interfacial energy is assumed to be much smaller than the surface energy [4]. The strain energy is caused by the lattice mismatch. The lattice mismatch between Fe and Mn is difficult to determine since a stable bulk bcc or fcc structure does not exist at RT and consequently lattice parameters for the bcc and fcc structures must be extrapolated from either high temperature phases or alloyed phases [1]. Kim *et al.* showed that the observed bct structure of Mn films might be a distortion of either a fcc or a bcc phase. Based upon their analysis the in-plane lattice mismatches are estimated -8 % and $+4$ % for fcc and bcc, respectively [1]. Due to this high lattice mismatch the strain energy plays a key role for the change of the growth mode. In our case, due to an increase of the strain energy, the total energy $\Delta\gamma$ is likely to change from negative to positive at a coverage of 3 ML and consequently layer-plus-island growth sets in.

Our STM topographic results differ from the results reported by Tulchinsky *et al.* which showed that for comparable growth rate and temperature the layer-by-layer growth continues up to 10 ML without any 3D islands [9,14]. The Fe whisker used in this study is not of the high flatness (see Fig. 18(a)) as the ones used by Tulchinsky *et al.* [14], i.e., our Fe whisker has a higher Fe step density. Furthermore, various defects can be observed on the Fe(001) surface [15], e.g., “Ar bubble-like” defects [16,17], holes (~5 nm deep) caused by the sputtering, and screw dislocations. Since this non-ideal surface morphology is expected to lead to an increase of the interface energy, an influence on the growth process is likely. Therefore, the onset seems to depend strongly on the quality of the Fe(001) whisker although it may depend on the growth rate and temperature as well.

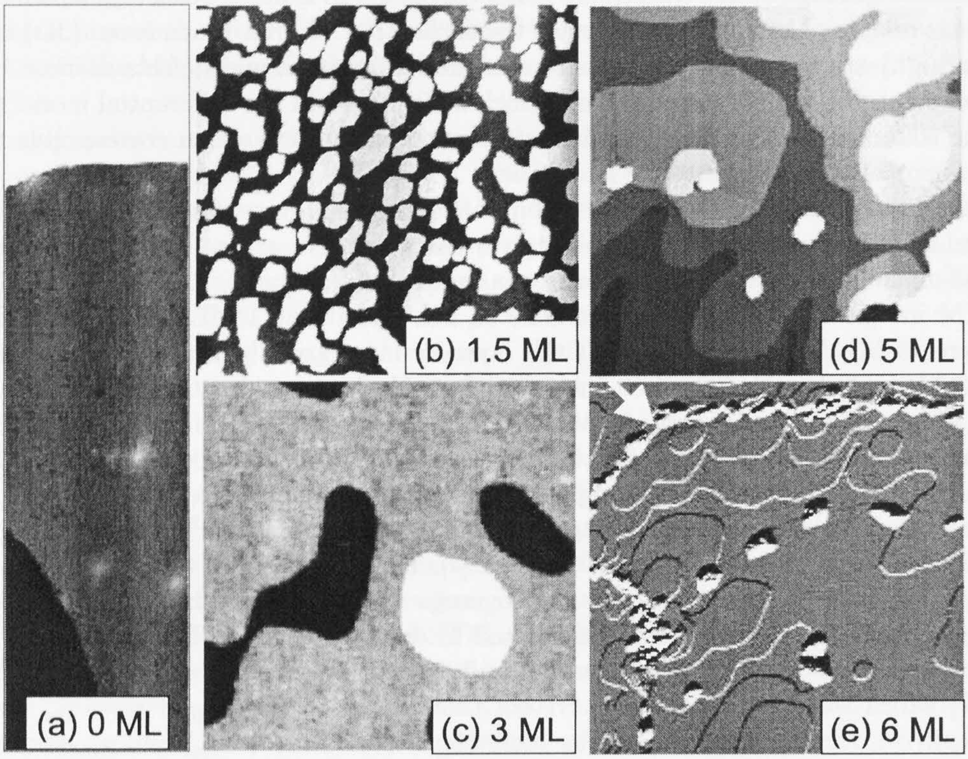

FIG. 18. STM topographic images of Mn layers grown on the Fe(001) whisker at 370 K. (a) the bare whisker, 310 × 80 nm^2, $V_S = -1.00$ V, $I = 0.06$ nA. (b) 1.5 ML, 165 × 157 nm^2, $V_S = -0.38$ V, $I = 0.05$ nA. (c) 3 ML, 100 × 100 nm^2, $V_S = -0.34$ V, $I = 2.00$ nA. The second, third, and fourth layer are visible. (d) 5 ML, 200 × 200 nm^2, $V_S = -1.00$ V, $I = 0.05$ nA. (e) 6 ML, 300 × 300 nm^2, $V_S = -1.00$ V, $I = 0.05$ nA. (e) shows the data in the differential mode in which the grey scale is proportional to the gradient of the height variation along each scan line. In (e) the white arrow denotes the defect and the hidden Fe step.

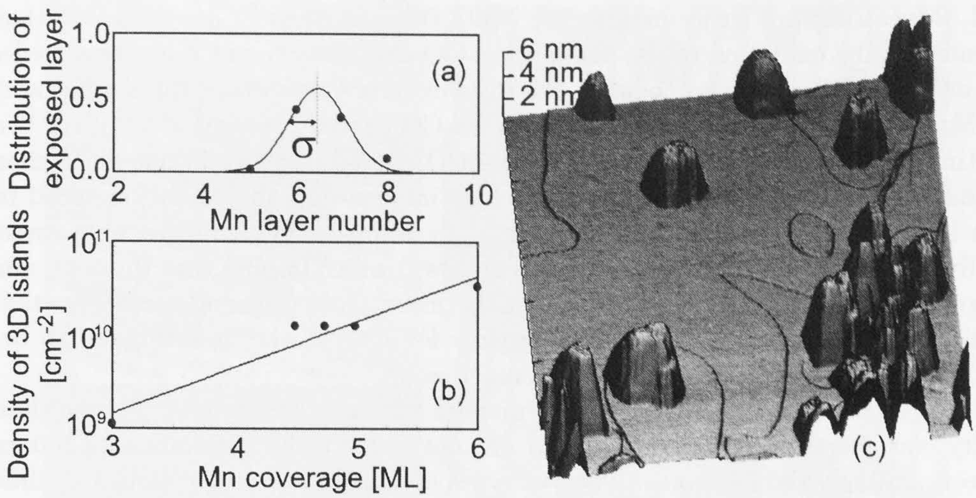

FIG. 19. (a) Distribution of exposed Mn layer at a coverage of 6.5 ML Mn. Average Mn coverage and its deviation, σ, are obtained from a Gaussian fit. (b) The dependence of the 3D islands density on Mn coverage. The 3D islands appear at a coverage of 3 ML and their density increases with the coverage. The solid line is a guide to the eye. (c) shows a 3D image of the 3D islands, which shows that these islands have a "pyramid-like" shape (300×300 nm^2, $V_S = -1.20$ V, $I = 0.05$ nA).

B. Atomically and chemically resolved STM topographic images

Figure 20 shows atomically resolved STM topographic images obtained on the Fe(001) substrate (a), the first (b), and the fifth (c) Mn adlayer, respectively. Atomically resolved images could be observed on all Mn adlayers studied (i.e., up to the seventh Mn layer). The STM images include a slight distortion due to thermal drift (~0.3 nm/min) resulting in a deviation from 90° of the angle between the close-packed lattice directions (which are indicated in Fig. 20(a)) [7]. From the atomically resolved STM images it can be concluded that for all the Mn adlayers the in-plane lattice constant equals the Fe(001) lattice constant within the accuracy of STM, which corresponds with the results of quantitative LEED [1]. Furthermore, since there is no indication for an in-plane relaxation such as dislocation networks, the Mn adlayer must follow the Fe substrate lattice.

With special tip conditions atomically and chemically resolved images were obtained (Fig. 20), e.g. Fe(001) lattice atoms with a corrugation of 10 pm (Fig. 20(a)) and Mn(001) lattice atoms with a corrugation of 35 pm (Fig. 20(b)).

The chemically resolved image obtained on the first Mn layer shows three kinds of depressions (Fig. 20(b)). The depressions marked "1" (~60 pm deep) and marked "2" (~60 pm deep) are observed at lattice sites and hollow sites, respectively. The concentration of both depressions is the same, i.e., 7±1 %. In Fig. 20(b), depressions marked "3" are observed as well. Their concentration is much lower (~1 %) and their contrast is much weaker (~25 pm deep).

To identify these three kinds of depressions, the possibility of oxidation must be considered. Mn atoms are easily oxidized to MnO [18]. Andrieu *et al.* proposed that the main cause of the oxidation of the Mn layer is CO dissociation which is already effective at RT on Mn ([18] and refs. therein). In their experimental setup, the oxidation speed of the Mn layer was 0.03 ML/hour from which a CO partial pressure of 3.3×10^{-11} mbar was estimated. Using mass spectrometry, the CO partial pressure in our STM chamber is estimated to be about 10 times better, which implies that the oxidation speed in our system is below 0.003 ML/hour. Our atomically resolved STM images were measured about five hours after the Mn layers had been grown, which implies that the total amount of oxygen contamination is below 1.5 %. Furthermore, with Auger spectroscopy, the concentration of impurities (mainly oxygen) on my Fe(001) whisker is estimated to be 1 % which is about the detection limit of our Auger setup.

Since the concentration of the atoms marked "1" and "2" is much higher than the impurity concentration, these depressions are not likely to be contaminants but rather the effect of intermixed Fe atoms. The two types of depressions are explained by different local environments of the Fe atoms: i.e., having 4 Fe nearest neighbors or 3 Fe and 1 Mn nearest neighbors in the layer below. Calculations and experiments with other techniques are needed to verify this assumption. On the other hand, the similar concentration and appearance in STM images obtained with normal tip conditions on Fe(001) with and without Mn deposition make us to identify the depressions "3" as oxygen impurities.

The effect of intermixed Fe is observed until the fourth Mn layer but decreases with layer thickness (see Fig. 21). On the fourth layer the concentration of these features equals the impurity concentration. Therefore, pure Mn layers are formed above the fourth layer. This is in agreement with the results of grazing ion-scattering measurements [8].

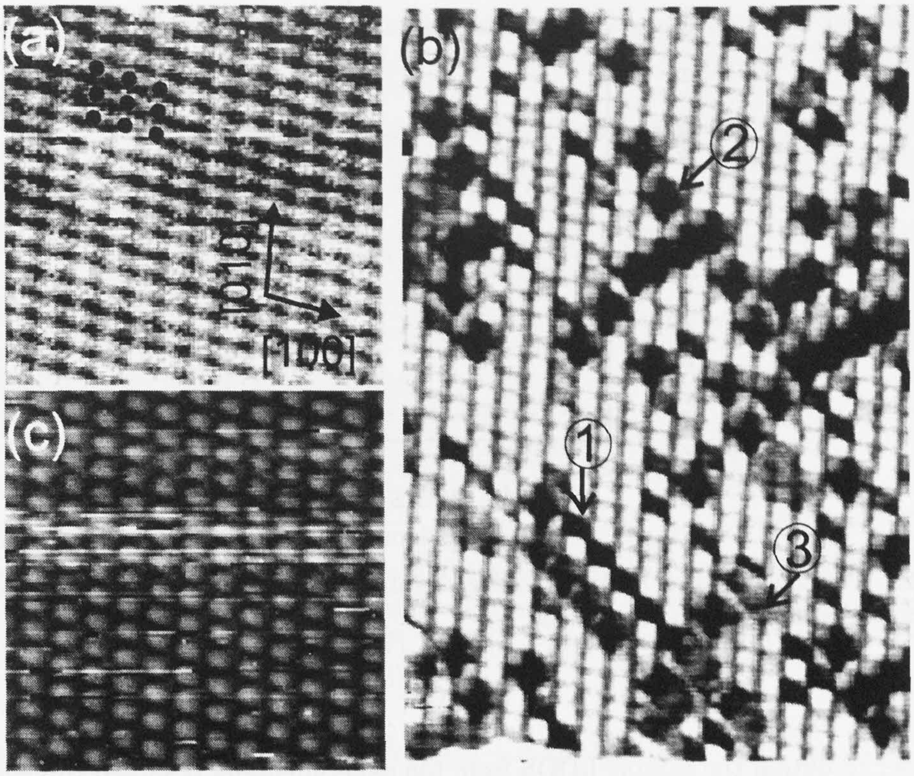

FIG. 20. Atomically and chemically resolved STM images of (a) the Fe(001) substrate (3.5×3.5 nm^2, $V_S = -2$ mV, $I = 2.3$ nA), (b) the first (6×9 nm^2, $V_S = -2$ mV, $I = 2.6$ nA), and (c) the fifth Mn layer (3.5×3.5 nm^2, $V_S = -7$ mV, $I = 2.6$ nA), respectively. The black dots in (a) indicate the positions of the atoms. The close-packed directions are shown in (a). Numbers in (b) denote three kinds of depressions on the surface (see text). The images are slightly distorted by thermal drift (~0.3 nm/min). The in-plane lattice constant along the [100] and [010] directions in the Mn layer is the same as the lattice constant of Fe(001).

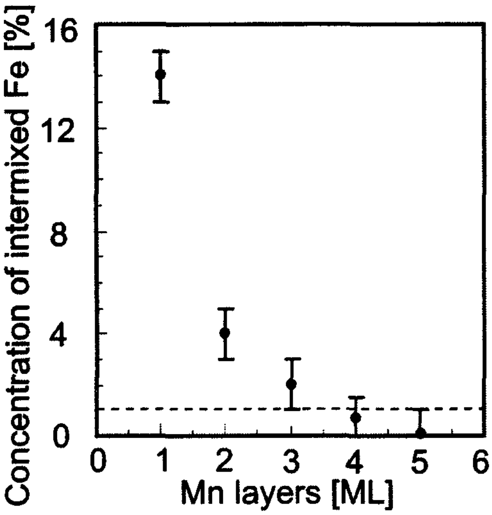

FIG. 21. The concentration of the intermixed Fe atoms in the various Mn layers. The dashed line indicates the impurity concentration.

C. STS

In order to obtain the sample LDOS from the experimentally obtained tunneling current as a function of the sample bias voltage ($I(V)$ curve), the $I(V)$ curve is numerically differentiated. The differentiated dI/dV curve reflects not only the sample surface LDOS, but also the tip surface LDOS and the tunneling probability (=exponential background). We checked that the energy position of the sample LDOS peak in the dI/dV curve is strongly influenced by the exponential background [15,19]. Also, in the dI/dV curve normalized by I/V, the sample LDOS peak shifts due to the imperfect normalization of the exponential background [15,19]. Then, we normalized the dI/dV curve by the tunneling probability function (T) and found that this normalization recover the sample LDOS peak in an accuracy of ±10 mV near the Fermi energy [15,19]. This normalization was theoretically shown by Ukraintsev in 1996 [20].

Using Eqs. 7 and 8 in chapter II, Ukraintsev described dI/dV as follows:

$$\begin{aligned} dI(z,V)/dV \cong A\Big[&eT'(z,V,E)\rho_s(E)\rho_t(E-eV)|_{E=eV} \\ &+ \int_0^{eV} T'(z,V,E)\rho_s(E)\frac{d\rho_t(E-eV)}{dV}dE \\ &+ \int_0^{eV} \frac{dT'(z,V,E)}{dV}\rho_s(E)\rho_t(E-eV)dE\Big], \end{aligned} \tag{9}$$

where A is a proportionality coefficient related to the effective tip-sample contact area [20]. Ukraintsev neglected the second and the third terms by assuming a constant tip DOS and negligible variation of T' within small sample bias voltages and claimed that these simplifications help to explain the basic principle of tunneling spectroscopy, but may lead to qualitatively wrong conclusions. To illustrate this statement, one may express the

dI/dV in a form symmetric with respect to the tip and the sample DOS by substituting $\xi = (E - eV/2)$ in Eq. 9.

$$\begin{aligned} dI(z,V)/dV \cong \frac{Ae}{2}\Big[&T''(z,\xi)\rho_s(\xi + eV/2)\rho_t(\xi - eV/2)\,|_{\xi=eV/2} \\ &+ T''(z,\xi)\rho_s(\xi + eV/2)\rho_t(\xi - eV/2)\,|_{\xi=-eV/2} \\ &+ \int_{eV/2}^{eV/2} T''(z,\xi)\frac{d\rho_s(\xi + eV/2)}{d\xi}\rho_t(\xi - eV/2)d\xi \\ &- \int_{eV/2}^{-eV/2} T''(z,\xi)\rho_s(\xi + eV/2)\frac{d\rho_t(\xi - eV/2)}{d\xi}d\xi\Big], \end{aligned} \tag{10}$$

where

$$T''(z,\xi) \equiv T'(z,V,E) = exp\Big[-2z\Big(\frac{2m}{\hbar^2}(\bar{\Phi} - \xi)\Big)^{1/2}\Big] \tag{11}$$

is the appropriate description of the tunneling probability function. $T''(z, eV/2)$ is the tunneling probability from the tip Fermi level to the sample unoccupied states. $T''(z, -eV/2)$ is the tunneling probability from the sample Fermi level to the tip unoccupied states [20].

At positive bias voltage, $T''(z, eV/2) \gg T''(z, -eV/2)$, the second term in Eq. 10 can be neglected. The dI/dV can be described as

$$dI(z,V)/dV \cong \frac{Ae}{2}T''(z, eV/2)[\rho_s(eV)\rho_t(0) + \Delta\rho_s(eV)\rho_t(0) - \rho_s(eV)\Delta\rho_t(0)], \tag{12}$$

where $\Delta\rho_s(eV)$ and $\Delta\rho_t(0)$ are effective changes in the sample and the tip DOS, respectively, in the proximity of $\xi = eV/2$, where the $T''(z,\xi)$ is close to its maximum value $T''(z, eV/2)$. In the same way, at negative bias voltage, $T''(z, -eV/2) \gg T''(z, eV/2)$, the dI/dV can described as

$$dI(z,V)/dV \cong \frac{Ae}{2}T''(z, -eV/2)[\rho_s(0)\rho_t(-eV) + \Delta\rho_s(0)\rho_t(-eV) - \rho_s(0)\Delta\rho_t(-eV)]. \tag{13}$$

Then, with T'''s below and above the Fermi energy, the tunneling probability function (T) can be described as follows:

$$T = a_t\ exp\Big[-2z\Big(\frac{2m}{\hbar^2}(\bar{\Phi} - eV/2)\Big)^{1/2}\Big] + a_s\ exp\Big[-2z\Big(\frac{2m}{\hbar^2}(\bar{\Phi} + eV/2)\Big)^{1/2}\Big]. \tag{14}$$

The first (second) term of T describes tunneling from the tip (sample) Fermi level to unoccupied sample (tip) states. a_t and a_s are proportionality coefficients related to the tip-surface effective contact area and are proportional to the tip and the sample DOS at the Fermi level, respectively. Thus, dI/dV normalized by T represents $\rho_s(eV) \cdot \rho_t(0)$ above and $\rho_t(eV) \cdot \rho_s(0)$ below the Fermi level.

$$\begin{aligned} (dI/dV)/T &\cong \rho_s(eV) \cdot \rho_t(0) \quad for \quad V > 0, \\ (dI/dV)/T &\cong \rho_s(0) \cdot \rho_t(eV) \quad for \quad V < 0. \end{aligned} \tag{15}$$

Although the second and the third term in Eqs. 12 and 13 cannot be neglected, only the normalization with T sufficiently recovers the sample DOS for V>0 for real data

[7,21,22]. Also, in Ukraintsev's simulations, input DOS were modeled to have some peaks with a constant amplitude [20]. The $(dI/dV)/T$ curves showed peaks at the same energy positions, but the peak amplitude slightly increases with the sample voltage. These effects are likely caused by the second and the third terms in Eqs. 12 and 13. However, these effects are small and the sample (tip) DOS above (below) the Fermi level were successfully recovered [7,21,22]. Although, the recovering method of sample DOS proposed by Ukraintsev is theoretically not perfect, at the moment this is the best method to recover the sample DOS from the experimentally obtained dI/dV curves. For example, peak energies can be recovered with an accuracy of 10 mV near the Fermi energy [7,21,22].

Although the $(dI/dV)/T$ curve recovers the sample DOS, one problem still remains. It is not clear if the recovered DOS corresponds to the DOS at the surface or to the DOS somewhere in the vacuum. By following the basic theory of STM (e.g Eq.6 and Fig. 4(a,b)), the obtained LDOS is the DOS at the tip-sample contact position ($z = 0$). If the normalization of dI/dV by T can remove all decay factors completely, the $(dI/dV)/T$ curve always shows the sample and the tip surface DOS. However, in this normalization only one decay factor was used (Eq.6). This causes the difficulty to find the z position of the LDOS obtained by $(dI/dV)/T$. One example is shown. dI/dV shows the tip and the sample LDOS with $z \neq 0$. Stroscio *et al.* and Bischoff *et al.* showed how the observations of the body-centered cubic (bcc) d-state Fe(001) peak in the dI/dV curves vary as a function the tip-sample separation [19,23]. When the tip-sample separation increases, the Fe(001) peak amplitude becomes smaller and smaller. And, when the tip is far enough from the Fe surface, dI/dV detects no peak. Then, the $(dI/dV)/T$ curve cannot recover the peak anymore. This indicates that the $(dI/dV)/T$ still includes the tip-sample separation dependence. (s, p, and d states have different decay factors (near the surface d-state dominates and far from the surface sp-state dominates.) Strictly speaking it is difficult to recover the density of all states using one T. Therefore, only when the tip and the sample have only one state contributing to the tunnel current, the obtained $(dI/dV)/T$ shows the LDOS exactly at the surface ($z = 0$).

Although Ukraintsev showed that normalizing dI/dV with its fitted tunneling probability function leads to the best recovery of the sample DOS, the recovery procedure is not very practical since it needs dI/dV data over a larger voltage range ($> 1.5V$) compared to usual dI/dV measurements ($< 1.5V$) (e.g., Fig. 22(c)). When there is not a large voltage range available, a fit by a quadratic function might work. The quadratic function is an approximation of the tunneling probability function for small V (see Eq. 14), i.e.

$$\begin{aligned}
T(V) &= a_t \cdot \underbrace{exp[-b(\bar{\phi} - \frac{V}{2})]}_{f(V)} + a_s \cdot \underbrace{exp[-b(\bar{\phi} + \frac{V}{2})]}_{g(V)} \\
&= a_t \cdot (f(0) + \frac{f'(0)}{1!}V + \frac{f''(0)}{2!}V^2 + \cdots) + a_s \cdot (g(0) + \frac{g'(0)}{1!}V + \frac{g''(0)}{2!}V^2 + \cdots) \\
&\approx [a_t f(0) + a_s g(0)] + [a_t f'(0) + a_s g'(0)]V + [a_t \frac{f''(0)}{2} + a_s \frac{g''(0)}{2}]V^2. \qquad (16)
\end{aligned}$$

$f'(V) = +\frac{b}{2}\exp(-b\exp(\bar{\phi} - \frac{V}{2}))$ and $g'(V) = -\frac{b}{2}\exp(-b\exp(\bar{\phi} + \frac{V}{2}))$, then $f'(0) = +\frac{b}{2}\exp(-b\exp(\bar{\phi}))$ and $g'(0) = -\frac{b}{2}\exp(-b\exp(\bar{\phi}))$. If $a_t \cong a_s$, $a_t f'(0) + a_s g'(0) \cong 0$. This quadratic function fitting was shown experimentally to recover successfully the DOS peak near the Fermi energy and a precise DOS peak energy (±0.01 V) is obtained [7].

The electronic structures of the Mn(001) layers were studied by STS with non-magnetic W tips.

STS was measured such that, first, at each pixel position the tip-sample separation was fixed by the current set point. Second, the tunneling current as a function of the sample bias voltage ($I(V)$) was measured at the same tip-sample separation. In this way, the spectroscopy map was obtained. A differential conductivity (dI/dV) curve was numerically obtained from the $I(V)$ curve. The dI/dV above the Fermi energy corresponds to the sample local density of states (LDOS) multiplied by the tip LDOS at the Fermi energy and the tunneling probability function (T). The sample LDOS is obtained by a normalization of the dI/dV by T.

Figure 22(a) shows an STM topographic image of Fe(001) covered with 1 ML Mn at a substrate temperature of 370 K. In Fig. 22(a), three layers are observed: the Fe substrate layer (marked "0"), the first (marked "1a + 1b"), and the second Mn adlayer (marked "2"). Less than 1 % of the substrate is still exposed. $I(V)$ curves are measured at 75×75 pixels at the area within the square indicated in Fig. 22(a). The dI/dV map at the bias voltage of +0.8 V is shown in Fig. 22(b). Based upon this dI/dV map, four kinds of dI/dV curves can be distinguished. Averages of typical 10 neighboring pixels are shown in Fig. 22(c). In Fig. 22(c), the averaged dI/dV curve from the Fe substrate shows a peak at 0.22 eV above the Fermi energy, which is attributed to a minority spin state of d_{z^2} symmetry [23,24]. On the first Mn layer, both depressed (cf. "1a") and bright ("1b") areas can be observed in the dI/dV map (Fig. 22(b)). The concentration of the depressions in Fig. 22(b) is ~7 % [10] , which corresponds to the concentration of one kind of depressions observed in Fig. 20(b). The equal concentration of the depressions implies that the depressed areas in the dI/dV map of Fig. 22(b) (i.e., those marked "1a") correspond to one type of Fe atoms which have been incorporated in the first Mn adlayer. The averaged dI/dV curve measured at the depressions shows a peak at 0.43 eV above the Fermi level (Fig. 22(c)). The averaged dI/dV curve of the bright areas "1b" does not show a peak, but it is clear that at positive voltages there is an additional contribution on top of the background (Fig. 22(c)). The averaged dI/dV curve obtained on the second Mn layer shows a strong shoulder around 0.3 eV above the Fermi level. The different dI/dV curves obtained on the first and the second layer must be related to the different coordination of the Mn atoms in the first and the second layer: Mn atoms in the first layer have an Fe layer underneath, while Mn atoms in the second layer cover a Mn layer.

The accurate energies of the peaks in the sample DOS are difficult to estimate from the dI/dV curve since the apparent energies may shift due to the voltage dependence of the tunneling probability in the dI/dV curve. To obtain the peak energy position of the sample DOS the dI/dV curves were fitted with quadratic functions since the dI/dV was measured within a small voltage range: −1 V ~ +1.5 V (see chapter II).

---

[10] Due to the high tunneling resistance (V_S=−0.5 V, I=0.5 nA), atomic resolution cannot be obtained in the spectroscopy measurement. If one spherical depression in Fig. 22(b) (i.e., one marked by circle) is related to a single atom, the concentration of the depressions is roughly estimated to be ~7 %.

The Fe(001) dI/dV curve in Fig. 22(c) has been fitted on the high positive voltage side to a quadratic function. Normalizing dI/dV by this fit shifts the peak from +0.22 eV in the dI/dV curve to +0.17 eV in the normalized curve (Fig. 22(d)) in agreement with the reported energy of the Fe(001) surface state [23].

Using the quadratic function fit, the sample DOS of the first and second layer are recovered (Fig. 22(d)). By analyzing many normalized dI/dV curves, it is found that this method finds the DOS peaks with an accuracy of ±0.02 V. Although band structure calculations are needed to reveal the nature of these peaks, it seems reasonable to interpret them as Mn(001) surface states. On the first layer, the bright and depressed areas in Fig. 22(b) show a peak at 0.35 eV and 0.28 eV above the Fermi energy, respectively. The peak energies at the bright and depressed areas in Fig. 22(b) correspond to the peak energies observed on the pure Mn p(1 × 1) and the alloyed FeMn c(2 × 2) structure obtained for submonolayer Mn growth at 420 K [7]. Therefore, the bright and depressed areas in Fig. 22(b) can be identified as pure Mn and alloyed FeMn areas. The second layer shows a peak at 0.20 V above the Fermi energy after normalization.

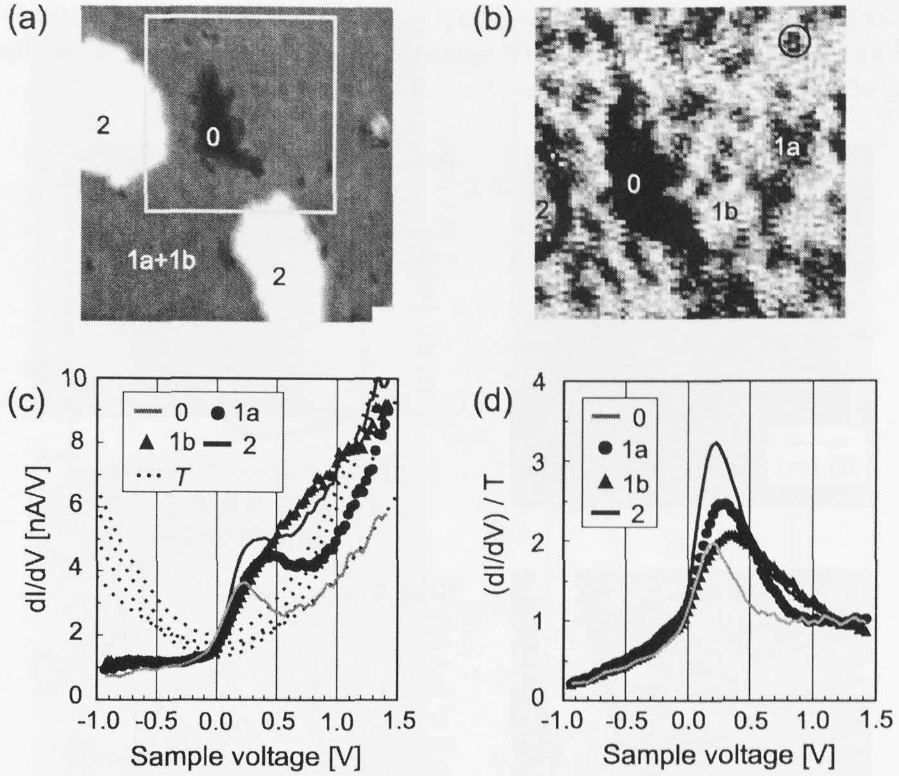

FIG. 22. STS measurement on Fe(001) covered with 1 ML Mn at 370 K. (a) is a topographic image obtained at a set point of $V_S = -17$ mV, $I = 0.5$ nA. Scan size is 15×15 nm^2. The Fe(001) surface, the first, and the second Mn layer are observed as the black (marked "0"), the grey (marked "1a + 1b"), and the white areas (marked "2"), respectively. (b) dI/dV map at +0.8 V measured at the area within the grey square in (a). Depressed (cf. "1a") and bright ("1b") areas are visible on the first Mn layer. One spherical depression is marked by a black circle. Scan size is 10×10 nm^2. (c) dI/dV curves representative of the areas indicated in (b). Curves are typically averages of 10 neighboring pixels. The quadratic functions fitted to the dI/dV curves are shown as dashed curves ("T"). (d) dI/dV curves of (c) normalized by quadratic background fits. Labels in (a) and (b) correspond to the ones in (c) and (d).

At a coverage of 2.8 ML Mn, three levels are exposed as shown in Fig. 23(a). At this area, dI/dV curves were obtained at 75×75 pixels and averages of typically 10 curves representative of the various layers are shown in Fig. 23(b). Since the dI/dV curve obtained on the lowest level of Fig. 23(a) is similar to the curve obtained on the second layer of Fig. 22, this level can be identified as the second Mn layer. The averaged dI/dV curve of the third Mn layer (Fig. 23(b)) shows a different behavior compared to the second layer. The dI/dV curve of the third layer steadily increases above the Fermi level without showing a peak or a shoulder. Whereas the averaged dI/dV curve of the fourth layer (Fig. 23(b)) shows a steady increase above the Fermi energy as well, the dI/dV values are lower compared to the third layer. Figure 23(c) shows the dI/dV map at +0.6 V measured at the same area as Fig. 23(a). Figure 23(d) shows the line profile along the white line in Fig. 23(c). This line profile reveals sharp dips at the steps since the dI/dV curves measured at the steps show lower dI/dV values (Fig. 23(b)), which might be related to a quenching of the surface states at steps [7].

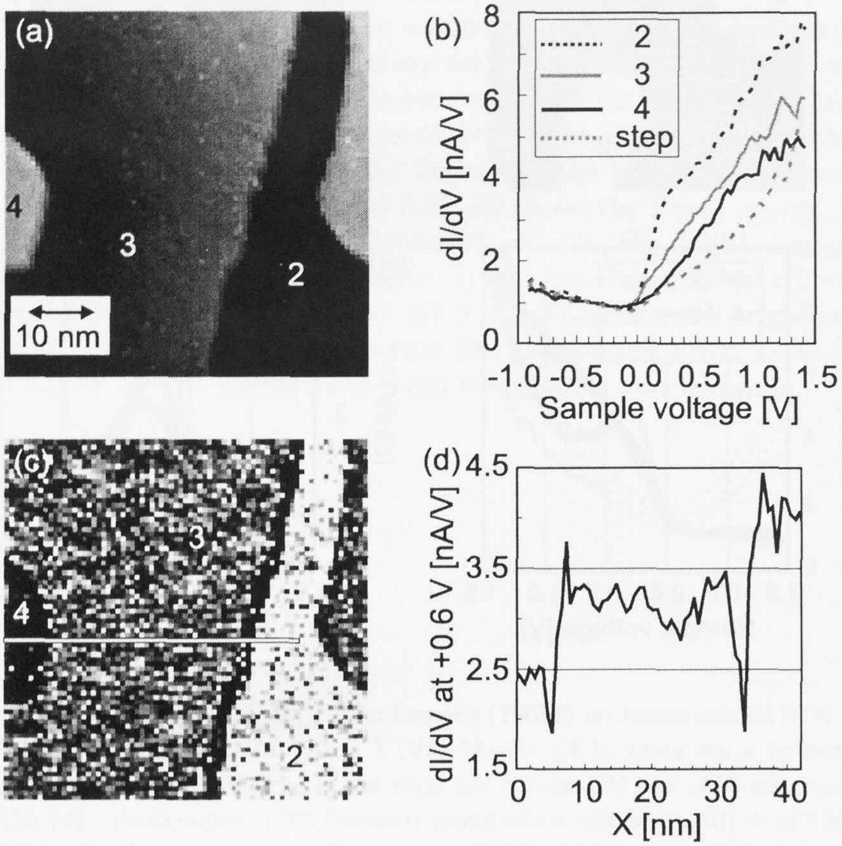

FIG. 23. STS measurement on Fe(001) covered with 2.8 ML Mn at 370 K. (a) is a topographic image obtained at a set point of $V_S = -0.54$ V, $I = 0.40$ nA. Scan size is 50×50 nm^2. Three different levels are exposed on the surface. (b) shows the dI/dV curves representative of each level. These curves are averages of typically 10 single curves. Since the dI/dV curve measured on the lowest level is similar to the one measured on the second layer, which is shown in Fig. 22(c), this layer is identified as the second layer. (c) shows the dI/dV map at +0.6 V measured at the same area as (a). Numbers in (a) and (c) denote the stacking number of the Mn layers. (d)The line profile along the white line in (c) shows sharp dips at the steps.

The STM/STS measurements on Mn films thicker than four layers are shown in Fig. 24. Figure 24(a) shows an STM topographic image obtained on the Fe(001) covered by 7.2 ML Mn, where five layers are exposed. At each pixel position in Fig. 24(a), STS measurements were performed and averaged dI/dV curves are shown in Fig. 24(b). dI/dV curves obtained on Mn films thicker than four layers are similar. Therefore, the dI/dV map at +0.2 V shows no contrast between Mn layers (Fig. 24(c)). A step height measurement at a horizontal white line in Fig. 24(a) shows no difference between different levels.

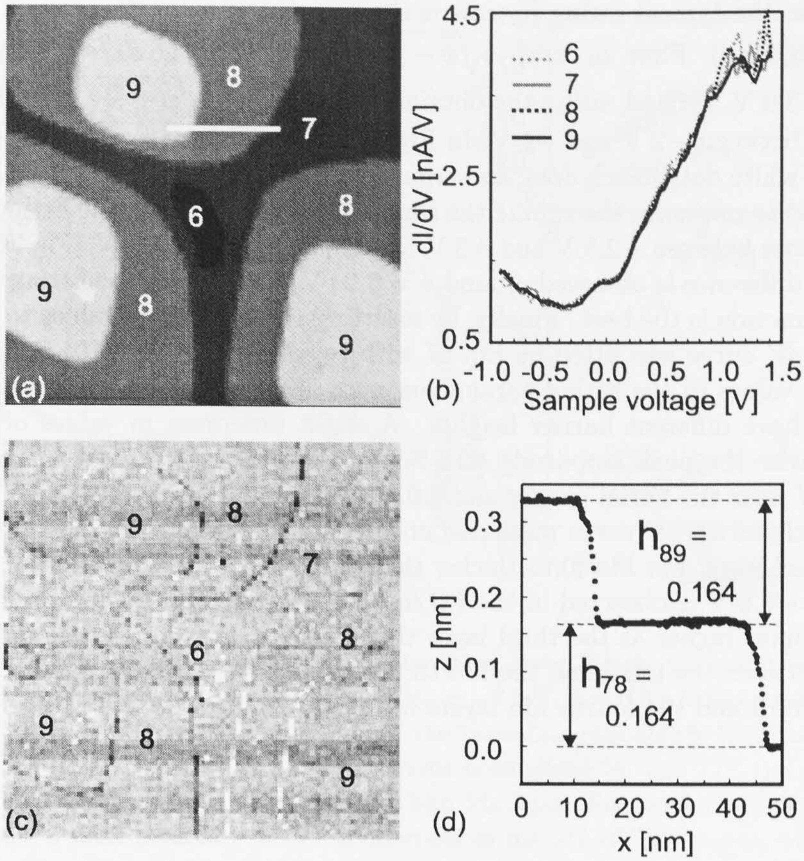

FIG. 24. STS measurement on Fe(001) covered with 7.2 ML Mn at 370 K. (a) is a topographic image obtained at a set point of $V_S = -0.5$ V, $I = 0.5$ nA. Scan size is 150×150 nm^2. Four different levels are exposed on the surface. (b) shows the dI/dV curves representative of each level. These curves are averages of typically 10 single curves. (c) shows the dI/dV map at +0.2 V measured at the same area as (a). Numbers in (a) and (c) denote the stacking number of the Mn layers.

For dI/dV curves measured on Mn films thicker than two layers, the quadratic function fit should also allow for an accurate evaluation of the DOS. However, the dI/dV curves show a linear-like increase up to +1.5 V. Therefore, it is impossible to fit this background to a quadratic function. For Mn films thicker than two layers, dI/dV measurements were performed within a large voltage range from −2 V to +3 V (Fig. 25(a)). T was obtained from a fit to the dI/dV curves above +2 V and below −1 V, since here the dI/dV curve increases exponentially. T is given by (c.f. Eq. 14):

$$T = a_t \cdot exp[-b\sqrt{\bar{\phi} - \frac{eV}{2}}] + a_s \cdot exp[-b\sqrt{\bar{\phi} + \frac{eV}{2}}], \qquad (17)$$

where $b = 2(2m/\hbar^2)^{1/2}z \simeq 1.02z$ and the dimension of z is Å. $\bar{\phi}$ was varied from 2 eV to 6 eV step by step and the three parameters (a_t, a_s, b) were obtained by a least-square fit.

As an example, the typical fitting process is shown using the dI/dV curve of the fourth Mn layer in Fig 25(a). First, $a_t \cdot exp[-b\sqrt{\bar{\phi} - \frac{eV}{2}}]$ was fitted to the dI/dV values between +2.5 V and +3.0 V. Second, using the obtained b, $a_s \cdot exp[-b\sqrt{\bar{\phi} + \frac{eV}{2}}]$ was fitted by the dI/dV values between −2 V and −1 V. In Fig 25(b) The obtained values of b, a_t, and a_s are plotted as white dots, black dots, and triangles, respectively. By varying $\bar{\phi}$ we tried to find the best fit to minimize the sum of the squared residues between the fitting curve and the dI/dV values between +2.5 V and +3 V as well as −2 V and −1 V (Fig 25(c)). Since the minimum difference is observed around $\bar{\phi} = 3.2$ eV, we believed the fitting parameters at this work function is the best. Finally, by inserting these obtained values to Eq. 17, the full-range dI/dV curve was fitted by Eq. 17 with two Gaussian peaks to find the energy position. The values in the fitting parameters were different between different tips since different tips have different barrier heights. A slight difference in values of the fitting parameters varies the peak amplitude ±15 % and the width ±5 %, but the peak energy only ±0.01 eV near the Fermi energy and ±0.1 eV around 1 V.

The normalized dI/dV curve measured on the third layer shows a peak around 0.8 V above the Fermi level. For Mn films thicker than three layers, besides this +0.8 V peak a weak peak at −0.6 V is observed in the $(dI/dV)/T$ curves. The +0.8 V peak amplitude is about 1.3 times higher at the third layer than at thicker layers. These different peak amplitudes between the third and the fourth layer cause the differences in dI/dV curves between the third and the fourth Mn layers in Fig. 23(b).

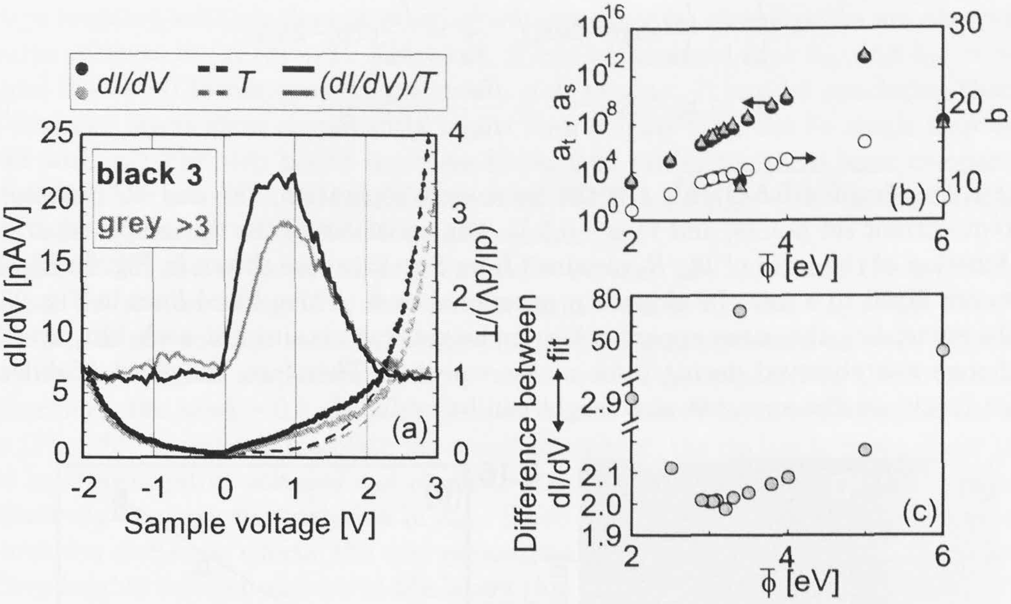

FIG. 25. (a)dI/dV curves measured at the third layer (black dots) and layers above the third layer (grey dots). The same set point of $V_S = -0.5$ V, $I = 0.5$ nA was used and curves are averages of typically 20 single curves. Fits of the tunneling probability function to the dI/dV curves are also shown ("T"). The dI/dV curves normalized by this "T", i.e., "$(dI/dV)/T$", reveal a strong peak around +0.8 eV for the third Mn layer. For thicker Mn films, besides this +0.8 eV peak, a weak peak at −0.6 eV is observed in the $(dI/dV)/T$ curves. (b) Values of the fitting parameters (b, a_t, and a_s) of T to the dI/dV of the fourth Mn layer in (a) are shown as a function of $\bar{\phi}$. (c) The sum of the squared residues between the dI/dV curve of the fourth Mn layer in (a) and the fitting curve for the energy range of +2.5∼+3 V and −2∼−1 V is shown as a function of $\bar{\phi}$.

D. The step height

Since variation in the apparent barrier heights may lead to different apparent step heights [25,26], apparent barrier heights were estimated from a measurement of the dependence of the tip-sample separation on the current (voltage was kept constant). In constant current mode the current set point was varied from 0.01 nA to 1 nA during the scanning, while the same voltage set point was used. Figure 26(a) shows an STM image obtained on the surface of 5 ML Mn film grown on the Fe-whisker. The fourth ("4"), fifth ("5") and the sixth ("6") Mn layers are exposed. During the scanning the current set point was varied, which explains the different grey scales on the same Mn terrace. The variation of the tip-sample separation was obtained from the height differences between "A"-"D". The height differences were obtained by measuring distances between Gaussian peaks in the histogram of Fig. 26(a). From the experimentally obtained height differences, the barrier heights of the Mn layers are deduced as follows:

$$\frac{I_a}{V_0} = \frac{I_{a0}}{V_0} exp[-2\kappa z_a], \quad \frac{I_b}{V_0} = \frac{I_{b0}}{V_0} exp[-2\kappa z_b]$$

$$\Delta z \equiv z_a - z_b = \frac{1}{2\kappa} \ln \frac{R_a}{R_b} - \frac{1}{2\kappa} \ln \frac{R_{a0}}{R_{b0}} \tag{18}$$

where κ is $\sqrt{2m(\bar{\Phi} + 0.5/2)/\hbar^2}$, z is the tip-sample separation, "a" and "b" denote the different current set points, and V_0 is -0.5 V. The variations of the tip-sample separation as a function of the ratio of R_a/R_b obtained from Fig. 26(a) are shown in Fig. 26(b). The points are fitted to a line. Its slope is proportional to $\bar{\Phi}$. Three fitted lines in Fig. 26(b) are the same, i.e. the same apparent barrier height was obtained at each Mn layer (no tip change was observed during these measurements). Therefore, the effect of different barrier height on the apparent step height can be excluded.

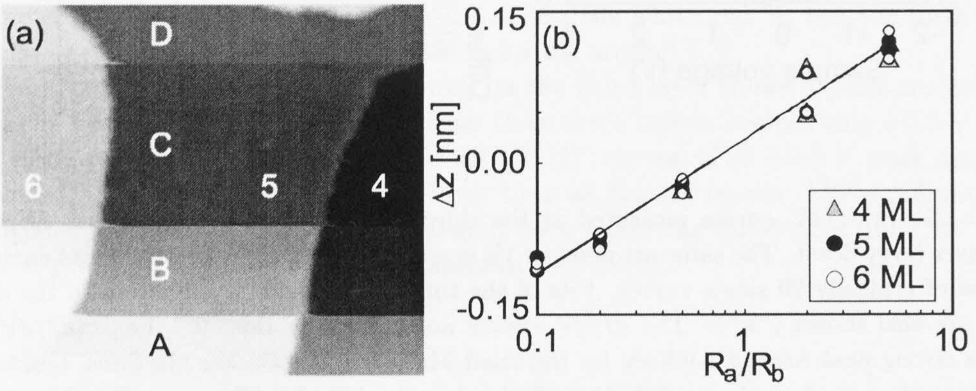

FIG. 26. (a) shows an STM image obtained on the surface of a 5 ML Mn film grown on the Fe(001)-whisker (44×39, V_S = −0.5 V, I = 0.01-1 nA). Between "A-D" the current set point was varied. Numbers denote the stacking numbers of the Mn layers. (b) shows variations of the tip-sample distance obtained from (a) as a function of the resistance ratio. From the slope the averaged barrier height is obtained. All Mn layers show the same slope.

Figure 27 shows that the apparent step heights of the Mn layers strongly depend on the sample voltage. Since the heights are independent of the current, which was confirmed for a range from 0.1 nA to 2 nA at a constant voltage, the results of Fig. 27 are obtained from STM topographic images recorded within this current range. h_{ij} indicates the apparent step height between level i and level j. h_{01}, h_{12}, and h_{23} show a considerable voltage dependence.

Since the Fe(001) substrate layer, the first, the second, and the third Mn layer reveal peaks at different energies above the Fermi level in $(dI/dV)/T$ (see Figs. 22(d) and 25), h_{01}, h_{12}, and h_{23} are influenced by the electronic structure (Figs. 27(a)-(c)). Since $(dI/dV)/T$ curves measured at the substrate, the first, the second, and the third layer are not completely the same at and below the Fermi level, electronic effects cannot be fully excluded from the step height measurements at large negative voltages, for which the tunneling current is dominated by sample states at the Fermi level [20]. Nevertheless, the influence of the electronic structure on the step heights is expected to be much lower at large negative voltages than at positive voltages since no strong peaks are observed at negative voltages in $(dI/dV)/T$. Therefore, it can be assumed that h_{01} and h_{12} = ~0.16 nm and h_{23} = ~0.18 nm give the geometric step heights. It can be concluded that: (i) The first two layers show significantly higher step heights than the Fe single step height (0.143 nm). (ii) The step height increases about 0.02 nm at the third layer compared to the first and the second layer, i.e., Mn layers on Fe(001) strongly relax at the third layer, which is in agreement with EXAFS measurements [2].

Figure 27(d) shows the apparent step height between the third and the fourth layer. Whereas the scatter in h_{34} is of the same order as that in h_{45} and h_{56} (Figs. 27(e) and 27(f)), h_{34} might contain some influence of the electronic structure as well. The third layer reveals a higher amplitude of the peak at +0.8 eV compared to the fourth layer. Furthermore, the weak −0.6 eV peak present on the fourth layer is absent on the third layer (Fig. 25). In order to maintain the constant current, the tip has to move closer to the third layer at negative voltages and closer to the fourth layer at positive voltages, which qualitatively explains the variation in h_{34}. Since at both negative and positive voltages h_{34} includes electronic effects, the real geometrical step height is difficult to disentangle.

Step heights between successive Mn layers (h_{45}, h_{56}, etc) show the same values (~0.165 nm) as shown in Figs. 27(e) and 27(f). These step heights (h_{45} and h_{56}) are almost independent of bias voltage, which can be explained by the equal dI/dV and $(dI/dV)/T$ curves measured at the fourth and subsequent layers. Therefore, it can be concluded that the apparent step height is similar for Mn films thicker than 3 ML in agreement with previous results [9]. The apparent step heights between the various layers, which are obtained at large negative voltages and are believed to be the most reliable values, are shown in Fig. 27(g).

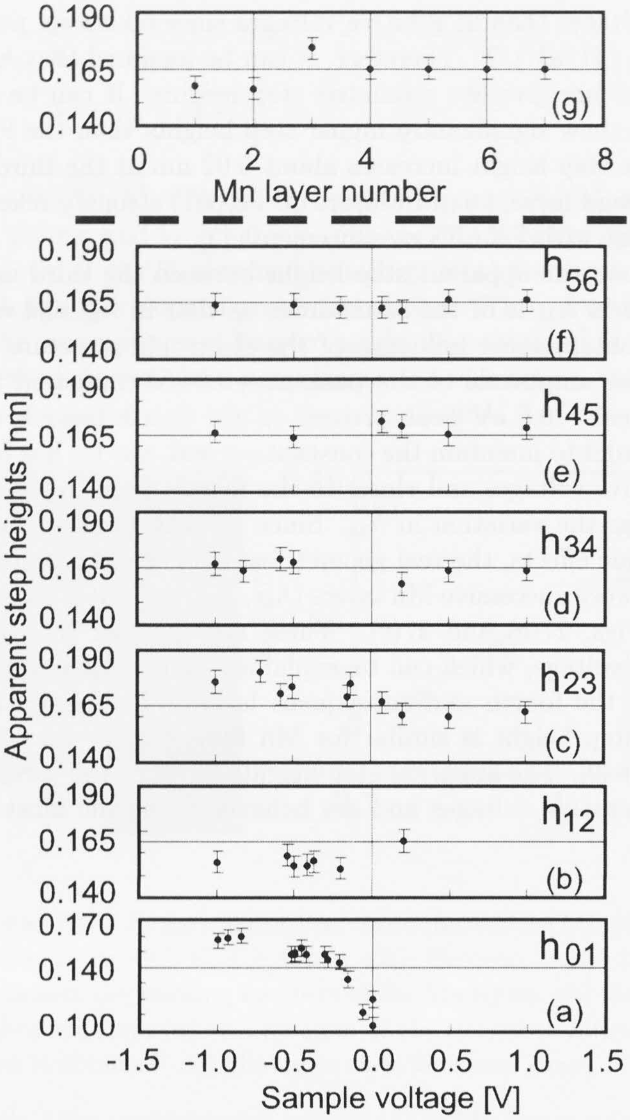

FIG. 27. Apparent step heights of the Mn layers as a function of the sample bias voltage. h_{ij} indicates the step height between level i and j. Since the heights are independent of the current, the height at each voltage is obtained from STM topographic images measured at current set points between 0.1 nA and 2 nA. The strong variation in h_{01} around the Fermi level is due to the Fe surface state. (g) shows the interlayer distances obtained at large negative voltages, which is believed to reflect the real geometric step heights.

E. Conclusion

For this project a suitable sample had to be selected. Then, a Mn(001) film grown on an Fe(001)-whisker at 370 K was chosen as a sample. This Mn film was shown by SEMPA to have Mn spins that couple ferromagnetically in the same sheet and that couple antiferromagnetically with Mn spins in sheets below and above.

Before studying the magnetic structure, the intermixing, geometric and electronic structures of the Mn film had to be studied since without knowledge of these it would be difficult to make firm conclusions about the SP-STS results. The intermixing and geometric structure of the Mn film were studied by STM with non-magnetic W tips. Atomically and chemically resolved STM images show that the Mn film grows with the same in-plane lattice constant as Fe(001) and that Fe atoms intermix with the first three layers: 14%, 4%, and 2% for the first, the second, and the third Mn layer, respectively. (Auger spectroscopy and STM/STS showed oxygen impurities with a concentration of less than 1 % on the Mn surface.) Starting from the fourth layer, the film consists of pure Mn. Furthermore, STM shows that the growth mode changes from layer-by-layer to layer-plus-island at a coverage of 3 ML Mn.

The electronic structures of the Mn(001) layers were studied by STS with non-magnetic W tips. As a result, the first Mn layer shows LDOS peaks at +0.35 V on pure Mn areas and at +0.28 V at mixed MnFe areas. The second layer shows a peak at +0.20 V. The Mn films thicker than two layers shows a peak at +0.8 V, while the peak amplitude obtained on Mn films thicker than three layers is about 1.3 times lower than that on the third Mn layer. Therefore, the Mn film thicker than four layers can be used to investigate the magnetic structures since these layers have the same DOS, the same geometric (bct) structure and consist of pure Mn, whereas the first three layers cannot be used due to the intermixing and different DOS for each layer.

Based upon our apparent step height measurements, we conclude that the first two Mn overlayers show significant higher step heights than the Fe single step height and that the Mn film relaxes by about 0.02 nm at the third layer. From the fourth layer the interlayer spacings are geometrically the same (about 0.165 nm).

Therefore, the Mn film thicker than four layers can be used to investigate the magnetic structures since these layers have the same DOS and consist of pure Mn, whereas the first three layers cannot be used due to the intermixing and different DOS for each layer.

REFERENCES

[1] S.K. Kim, Y. Tian, M. Montesano, F. Jona, and P.M. Marcus, Phys. Rev. B **54** (1996) 5081.

[2] S. Andrieu, M. Finazzi, Ph. Bauer, H. Fischer, P. Lefevre, A. Traverse, K. Hricovini, G. Krill, and M. Piecuch, Phys. Rev. B **57** (1998) 1985.

[3] S.T. Purcell, M.T. Johnson, N.W.E. McGee, R. Coehoorn, and W. Hoving, Phys. Rev. B **45** (1992) 13064.

[4] R. Pfandzelter, T. Igel, and H. Winter, Surf. Sci. **389** (1997) 317.

[5] B. Nonas, K. Wildberger, R. Zeller, and P.H. Dederichs, Phys. Rev. Lett. **80** (1998) 4574.

[6] B. Nonas, K. Wildberger, R. Zeller, and P.H. Dederichs, J. Magn. Magn. Mater. **165** (1997) 137.

[7] M.M.J. Bischoff, T. Yamada, A.J. Quinn, and H. van Kempen, Surf. Sci. **501** (2002) 155.

[8] T. Igel, R. Pfandzelter, and H. Winter, Surf. Sci. **405** (1998) 182.

[9] D.T. Pierce, A.D. Davies, J.A. Stroscio, D.A. Tulchinsky, J. Unguris, and R.J. Celotta, J. Magn. Magn. Mater. **222** (2000) 13.

[10] D.T. Pierce, J.A. Stroscio, J. Unguris, and R.J. Celotta, Phys. Rev. B **49** (1994) 14564.

[11] H. Brune and K. Kern, in: D.A. King and D.P. Woodruff (Eds.), *Growth and Properties of Ultrathin Epitaxial Layers, Chapter 5*, (Elsevier Science, Amsterdam, 1997).

[12] E. Bauer and J.H. van der Merwe, Phys. Rev. B **33** (1986) 3657.

[13] M. Aldén, H.L. Skriver, S. Mirbt, and B. Johansson, Phys. Rev. Lett. **69** (1992) 2296.

[14] D.A. Tulchinsky, D.T. Pierce, A.D. Davies, J.A. Stroscio, J. Unguris, and R.J. Celotta, J. Magn. Magn. Mater. **212** (2000) 91.

[15] M.M.J. Bischoff. PhD thesis, University of Nijmegen, The Netherlands, 2002.

[16] T. Michely and G. Comsa, J. Vac. Sci. and Technol. B **9** (1991) 862.

[17] M. Schmid, W. Hebenstreit, P. Varga, and S. Crampin, Phys. Rev. Lett. **76** (1996) 2298.

[18] S. Andrieu, E. Foy, H. Fischer, M. Alnot, F. Chevrier, G. Krill, and M. Piecuch, Phys. Rev. B **58** (1998) 8210.

[19] M.M.J. Bischoff, T.K. Yamada, C.M. Fang, R.A. de Groot and H. van Kempen, Phys. Rev. B **68** (2003) 045422.

[20] V.A. Ukraintsev, Phys. Rev. B **53** (1996) 11176.

[21] T.K. Yamada, M.M.J. Bischoff, G.M.M. Heijnen, T. Mizoguchi, and H. van Kempen, Phys. Rev. Lett. **90** (2003) 056803.

[22] T.K. Yamada, M.M.J. Bischoff, T. Mizoguchi, and H. van Kempen, Surf. Sci. **516** (2002) 179.

[23] J.A. Stroscio, D.T. Pierce, A. Davies, and R.J. Celotta, Phys. Rev. Lett. **75** (1995) 2960.

[24] A. Biedermann, O. Genser, W. Hebenstreit, M. Schmid, J. Redinger, R. Podloucky, and P. Varga, Phys. Rev. Lett. **76** (1996) 4179.

[25] G. Binnig, H. Rohrer, Ch. Gerber, and E. Weibel, Appl. Phys. Lett. **40** (1982) 178.

[26] T. Yamada, J. Fujii, and T. Mizoguchi, Surf. Sci. **479** (2001) 33.

V. MAGNETIC STRUCTURES ON MN/FE(001)

A. SP-STS results

Since Mn films thicker than four layers do not show intermixing and have homogeneous geometric and electronic structures, these films can be used to detect magnetic properties with SP-STM/SP-STS. In this chapter, the observation of a magnetic contrast in the SP-STS maps obtained with Fe-coated W tips on Mn layers (>3 ML) grown on an Fe(001) whisker at 370 K is reported. This magnetic contrast was not observed with clean W tips (see Fig. 24). Therefore, our results give strong evidence that the ferromagnetic Mn(001) sheets couple antiferromagnetically even on a sub-nanometer scale (<0.5 nm).

Figure 28 shows SP-STM/SP-STS measurements on 10 ML Mn grown on an Fe(001)-whisker performed with an Fe-coated W tip. Since the growth of Mn layers on Fe(001) changes at coverages above 3 ML from layer-by-layer to layer-plus-islands, five levels can be exposed at a coverage of 10 ML Mn as shown in Fig. 28(a). From the fourth layer the Fe intermixing in the Mn film can be neglected. At this surface, dI/dV curves were measured with Fe-coated W tips at 75×75 pixels at a set point of $V_S = -0.5$ V, $I = 0.5$ nA. At every pixel an $I(V)$ curve was measured which was numerically differentiated to obtain the dI/dV curve. Numbers in Figs. 28(a) and 28(c) denote the stacking numbers of the Mn layers, which were estimated by a quartz crystal oscillator calibration and Gaussian fits to the fraction of exposed layers on the surface. Figure 28(b) shows averaged dI/dV curves representative of each level. The solid and dotted curves were obtained on the odd and the even number Mn layers. Although the dI/dV curves obtained on the odd and the even Mn layers with clean W tips do not show any differences (see Fig. 24), the dI/dV curves obtained with the Fe-coated W tips show a clear difference above the Fermi energy for the odd and the even Mn layers (Fig. 28(b)). The dI/dV map at +0.2 V in Fig. 28(c) shows a strong dark-bright contrast between the different levels. Clearly, the contrast oscillates with a period of two layers. This oscillating contrast starts from the fourth Mn adlayer (not shown here) [1]. Although the odd layers (>3 ML), i.e., layer "9" and "11", are darker than the even layers ("8", "10", and "12") in the dI/dV map, this is not always the case, i.e., with some Fe-coated tips the odd layers appear darker than the even layers.

We explain the alternating contrast in the dI/dV maps obtained with Fe-coated W tips by the layered antiferromagnetic magnetization of the Mn(001) layers. This explanation is corroborated by the following observations: (i) The alternating contrast in the dI/dV maps has the same onset (>3 ML) and period (two layers) as previous results obtained with other less-local techniques [2–4]. (ii) The contrast is observed with the Fe-coated tips only; it is not observed with clean W tips. (iii) Reversed contrasts are also observed using different Fe-coated W tips. This indicates the random character of the tip magnetization direction. The strength and sign of the contrast (i.e., dark-bright might be reversed) depend strongly on the Fe-coated W tip used which demonstrates the degree of freedom of the tip magnetization direction.

A tentative model of the Mn films on the Fe(001)-whisker is shown in Fig. 28(d). Bright dots denote intermixed Fe. At the surface each Mn layer couples antiferromagnetically with the Mn layer above and below.

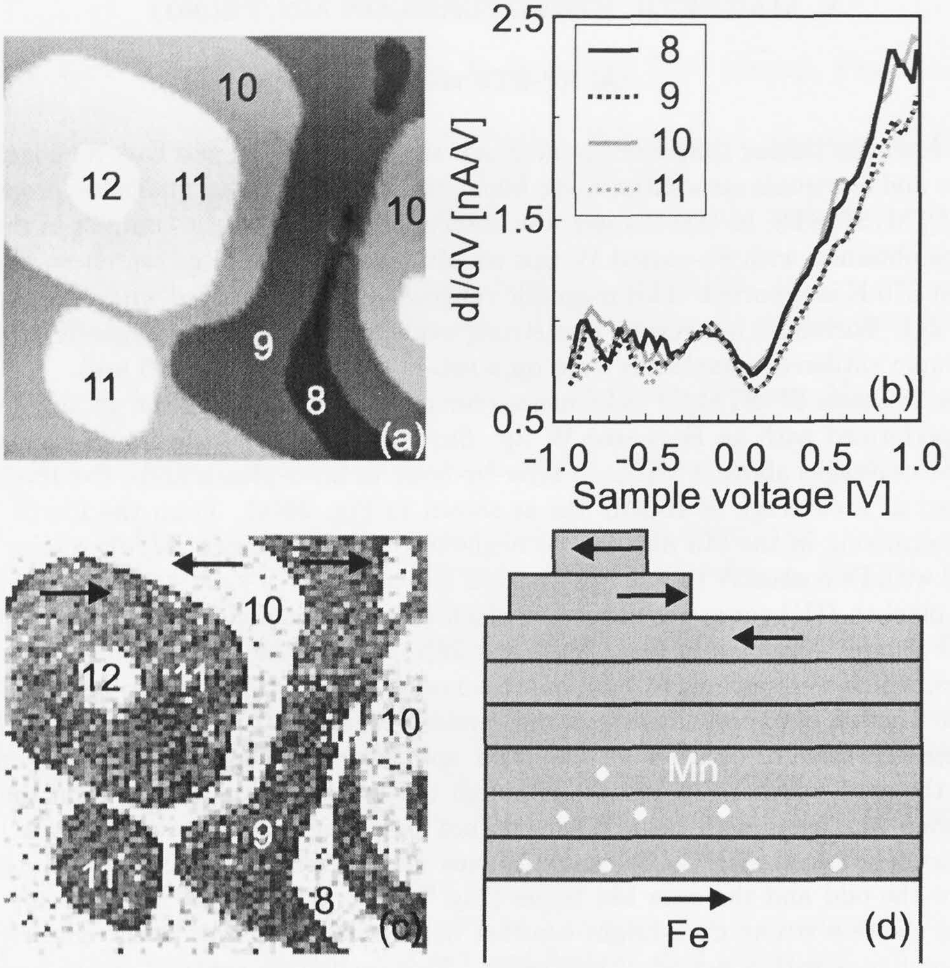

FIG. 28. SP-STM and SP-STS measurements on Fe(001) covered with about 10 ML Mn at 370 K. These measurements were performed with an Fe-coated W tip. (a) is the topographic image which was obtained at $V_S = -0.5$ V, $I = 0.5$ nA. Scan size is 100×100 nm^2. Five layers are exposed. Numbers in (a) and (c) denote the stacking numbers of the Mn layers. (b) shows dI/dV curves as a function of the sample bias voltage obtained on the Mn layers in (a). dI/dV curves obtained on even (odd) Mn layers are shown as solid (dashed) curves, which were numerically obtained from $I(V)$ curves measured at a set point of $V_S = -0.5$ V, $I = 0.5$ nA. (c) shows the dI/dV map at +0.2 V measured at the same area as (a). (d) reveals a model of Mn layers on the Fe(001) whisker. Darker and brighter colors denote Mn and Fe, respectively. The first three Mn layers include intermixed Fe atoms. Arrows denote magnetization directions.

The black and the grey $I(V)$ curves in Fig. 29(a) are obtained with an Fe-coated W tip on the odd and the even Mn layers, respectively, using a set point of $V_S = -0.2$ V, $I = 0.5$ nA. dI/dV and $(dI/dV)/(I/V)$ curves shown in Figs. 29(b) and 29(c), respectively, were numerically obtained from the $I(V)$ curves. Although all spectra show magnetic contrasts, the characteristics of the spectra are different. The $I(V)$ curves increase exponentially as a function of the sample bias voltage and show almost no contrast below the Fermi energy, but the contrast is clearly visible above the Fermi energy. The dI/dV curves are similar to Fig. 28(b) and show a small peak around −0.2 V and steadily increase above the Fermi energy. The magnetic contrast is clearly observed above the Fermi energy. The $(dI/dV)/(I/V)$ curves show a small peak around −0.2 V and a shoulder at +0.2 V. By definition, $(dI/dV)/(I/V)$ at 0 V is 1. Magnetic contrast is observed around the Fermi energy and the curves obtained on the odd and the even layers are crossing at −0.2 V and +0.2 V. From these observations, the dI/dV map seems to be the best to see a strong or clear magnetic contrast. $(dI/dV)/(I/V)$ makes the contrast smaller due to cancellation of the dI/dV and $I(V)$ contrast. When the DOS is spin-polarized below or above the Fermi energy, higher voltages should be chosen to see stronger magnetic contrast in the $I(V)$ map. The highest contrast in $I(V)$ is observed for large voltages (>0.5 V). The reason is that $I(V)$ reflects an integration of the DOS below V. As long as unpolarized states are involved in this integration, the contrast will be reduced.

Figure 29(d-f) shows the asymmetries in $I(V)$ (d), dI/dV (e), and $(dI/dV)/(I/V)$ (f) obtained from (a), (b), and (c), respectively. The asymmetry in $I(V)$ is defined as $A_{I(V)} = (I(V)_{odd} - I(V)_{even})/(I(V)_{odd} + I(V)_{even})$. The asymmetry in dI/dV is defined as $A_{dI/dV} = (dI/dV_{odd} - dI/dV_{even})/(dI/dV_{odd} + dI/dV_{even})$. The asymmetry in $(dI/dV)/(I/V)$ is defined as $A_{(dI/dV)/(I/V)} = ((dI/dV)/(I/V)_{odd} - (dI/dV)/(I/V)_{even})/((dI/dV)/(I/V)_{odd} + (dI/dV)/(I/V)_{even})$. The shape of these asymmetries is similar: A peak or a shoulder above the Fermi energy, near zero below the Fermi energy, and a gradual increase at higher negative voltages. $A_{I(V)}$ and $A_{dI/dV}$ show the highest amplitude of ~20 % above the Fermi energy. $A_{(dI/dV)/(I/V)}$ shows only 5 %.

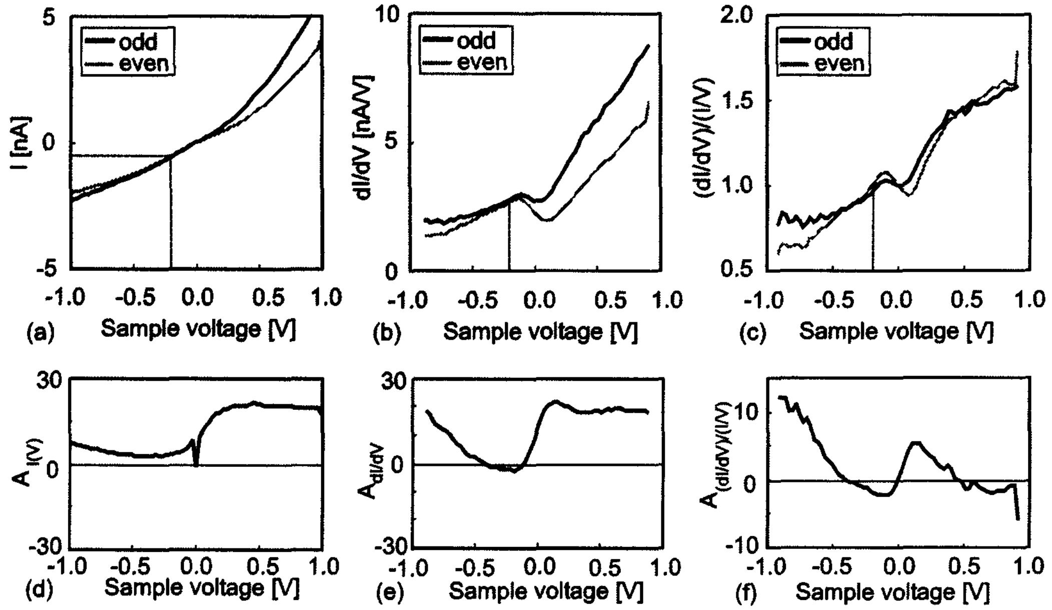

FIG. 29. SP-STS measurements obtained on Mn layers (>3 ML) on Fe(001). Black and grey curves are obtained on the odd and the even Mn layers, respectively. (a) shows the tunneling current (I) as a function of sample bias voltage (V) at a set point of $V_S = -0.2$ V, $I = 0.5$ nA. (b) and (c) show dI/dV and $(dI/dV)/(I/V)$ curves, respectively, obtained numerically from (a). For (c), $(dI/dV)/(I/V)$ at 0 V is 1 by definition. In (a-c), dashed lines denote the set point. (d) shows the asymmetry in $I(V)$ obtained from (a). In (d), a sharp peak at 0 V is caused by 0 nA / 0 nA, which has no physical meaning. (e) shows the asymmetry in dI/dV obtained from (b). (f) shows the asymmetry in $(dI/dV)/(I/V)$ obtained from (c).

SP-STS can be described by following Ukraintsev's method. Now the tip and the sample are assumed to have a peak in "minority" band at and above the Fermi level, respectively (see Fig. 30). The polarization is defined by the difference between the number of electrons in "minority" and "majority" bands integrated up to the Fermi level. When the number of the electrons in "majority" band is higher than that in "minority" band, the polarization direction is defined as positive. With a magnetic sample and a magnetic tip, $(dI/dV)/T$ can be described by modifying the sample and the tip DOS terms in Eq. 15. Since the tip-sample separation is dictated by the feedback loop to keep a constant current, this separation is secondarily influenced by the spin-polarized DOS, and consequently the T is modified. Since it was checked on the Mn layers that the work function is not spin-dependent (see Fig. 32), the work function term in T is not modified. To describe the SP-STS data we include polarization vectors of the sample ($\vec{P_S}$) and the tip ($\vec{P_T}$) as shown in the right-top inset in Fig. 6. The sample polarization vector ($\vec{P_S}$) defines the x-axis. Then, the $\vec{P_S}$ and $\vec{P_T}$ can be described as follows:

$$\begin{aligned} \vec{P_S} &= (P_S,\ 0,\ 0), \\ \vec{P_T} &= (P_T \cos\phi \cos\theta,\ P_T \cos\phi \sin\theta,\ P_T \sin\phi), \end{aligned} \tag{19}$$

where $0 \leq \phi \leq \pi/2$, $|\vec{P}_S| \equiv (\rho_{S\uparrow}-\rho_{S\downarrow})/(\rho_{S\uparrow}+\rho_{S\downarrow})$, and $|\vec{P}_T| \equiv (\rho_{T\uparrow}-\rho_{T\downarrow})/(\rho_{T\uparrow}+\rho_{T\downarrow})$. $\rho_{S\uparrow}$ ($\rho_{T\uparrow}$) and $\rho_{S\downarrow}$ ($\rho_{T\downarrow}$) denote spin-up and spin-down sample (tip) DOS, respectively. Here, the x-y plane is defined as the sample surface. The z axis is perpendicular to the x-y plane. Based on the basic idea of the "spin-valve" [5], spin-polarized tunneling depends on the dot product.

$$\vec{P}_S \cdot \vec{P}_T = P_S P_T \cos\phi \cos\theta. \tag{20}$$

Thus, if $\vec{P}_T$ does not have an x-component, the tunneling current is not spin-polarized.

By following Ukraintsev's theory, dI/dV can be described as $\rho_S(eV) \cdot \rho_T(E_F) \cdot T$ for V>0 and $\rho_T(eV) \cdot \rho_S(E_F) \cdot T$ for V<0. Here, only the DOS and the tip-sample separation can be spin-polarized. Simply, the spin-polarized factor $\vec{P}_S \cdot \vec{P}_T$ is introduced into the DOS and the tip-sample separation terms as follows:

$$\begin{aligned} dI/dV(eV) &= \underbrace{\frac{1}{2}\rho_S(eV)\rho_T(E_F)[1+\vec{P}_S(eV)\cdot\vec{P}_T(E_F)]}_{\boxed{1}} \\ &\cdot \underbrace{\exp\Big[-2\kappa(z_{non}+z_{sp}(\vec{P}_T(E_F)\cdot\vec{P}_S(V_{setpoint})))\Big]}_{\boxed{2}} \; for\ V>0, \end{aligned} \tag{21}$$

$$\begin{aligned} dI/dV(eV) &= \underbrace{\frac{1}{2}\rho_S(E_F)\rho_T(eV)[1+\vec{P}_T(eV)\cdot\vec{P}_S(E_F)]}_{\boxed{1}} \\ &\cdot \underbrace{\exp\Big[-2\kappa(z_{non}+z_{sp}(\vec{P}_S(E_F)\cdot\vec{P}_T(V_{setpoint})))\Big]}_{\boxed{2}} \; for\ V<0, \end{aligned} \tag{22}$$

where κ is $\sqrt{2m(\bar{\Phi}-eV/2)/\hbar^2}$ above the Fermi level and $\sqrt{2m(\bar{\Phi}+eV/2)/\hbar^2}$ below the Fermi level. ρ_S and ρ_T denote the non-spin-dependent sample and tip DOS, respectively. z_{non} denotes the non-spin dependent term in the tip-sample separation. z_{sp} denotes the spin dependent term in the tip-sample separation as a function of $\vec{P}_S(E_F) \cdot \vec{P}_T(V_{setpoint})$. In Eqs.21 and 22, $\boxed{1}$ denotes the non-spin-polarized and the spin-polarized tip and sample DOS. $\boxed{2}$ denotes the tunneling probability including spin-dependency. Experimentally, a spin-dependency in the tip-sample separation was observed [6,7]. The tip-sample separation is set in the constant current mode before starting the spectroscopy measurement [11] . When the tip and the sample polarizations are parallel, the tip retracts from the sample.

---

[11] In a spectroscopy measurement, first in the constant current mode the tip-sample separation is set. The spin-dependency in the tip-sample separation is included at this point. Then, at a constant tip-sample distance, the tunneling current is obtained as a function of the sample bias voltage.

And, when the tip and the sample polarizations are anti-parallel, the tip moves closer to the sample surface. [2] explains these experimental results. However, it must be noted that the spin-dependency in [2] is set by the set point voltage ($V_{setpoint}$) instead of the measuring voltage (V). The spin-dependency of z depends on the integral of the tip and the sample polarization from the Fermi energy to the set point voltage. The polarizations as well as the magnetizations of the tip and the sample are assumed not to be changed during the spectroscopy measurements, i.e. at the measuring voltage and the set point voltage the angle between the tip and the sample polarization is assumed to be the same. Then, the tunnel current at the set point voltage can be described as

$$\begin{aligned} I_{setpoint} = &\int_{E_F}^{V_{setpoint}} \frac{1}{2}\rho_S(V')\rho_T(E_F)[1+\vec{P}_S(V')\cdot\vec{P}_T(E_F)] \\ &\cdot \exp\Big[-2\kappa(z_{non}+z_{sp}(\vec{P}_T(E_F)\cdot\vec{P}_S(V')))\Big]dV' \; for\ V>0. \end{aligned} \tag{23}$$

Since the highest contribution in the integral comes from $\exp\Big[-2\kappa(V_{setpoint})\cdot(z_{non}+z_{sp}(\vec{P}_T(E_F)\cdot\vec{P}_S(V_{setpoint})))\Big]$,

$$\begin{aligned} I_{setpoint} \simeq\ & \frac{1}{2}\rho_S(V_{setpoint})\rho_T(E_F)[1+\vec{P}_S(V_{setpoint})\cdot\vec{P}_T(E_F)] \\ &\cdot \exp\Big[-2\kappa(V_{setpoint})(z_{non}+z_{sp}(\vec{P}_T(E_F)\cdot\vec{P}_S(V_{setpoint})))\Big] \; for\ V>0. \end{aligned} \tag{24}$$

Now, the model shown in Fig. 6 is considered. The tip polarization couples 0 or 180 degrees with the sample polarization. Then, the tunneling current at the set point voltage on the different terraces can be described as

$$\begin{aligned} I^{\uparrow\uparrow}_{setpoint} &\simeq \frac{1}{2}\rho_S\rho_T[1+P_S\cdot P_T]\cdot\exp\Big[-2\kappa(z_{non}+z_{sp}(P_S\cdot P_T))\Big] \\ I^{\uparrow\downarrow}_{setpoint} &\simeq \frac{1}{2}\rho_S\rho_T[1-P_S\cdot P_T]\cdot\exp\Big[-2\kappa(z_{non}-z_{sp}(P_S\cdot P_T))\Big]. \end{aligned} \tag{25}$$

Since $I^{\uparrow\uparrow}_{setpoint} = I^{\uparrow\downarrow}_{setpoint}$,

$$\begin{aligned} \Delta z \equiv z_{sp}(P_T\cdot P_S) &= \frac{1}{4\kappa(V_{setpoint})}\ln\frac{1+P_S(V_{setpoint})\cdot P_T(E_F)}{1-P_S(V_{setpoint})\cdot P_T(E_F)} \; for\ V>0, \\ \Delta z \equiv z_{sp}(P_T\cdot P_S) &= \frac{1}{4\kappa(V_{setpoint})}\ln\frac{1+P_T(V_{setpoint})\cdot P_S(E_F)}{1-P_T(V_{setpoint})\cdot P_S(E_F)} \; for\ V<0, \end{aligned} \tag{26}$$

where, at the set point voltage, $z_{sp}(\vec{P}_S\cdot\vec{P}_T) \equiv \Delta z\cos\theta\cos\phi$ is used. Since experimentally the maximum Δz was obtained around 0.1 Å for the Mn(001), $\Delta z = 0.1$ Å is assumed. Also, it should be noted that when the polarity of the polarization at the set point voltage ($V_{setpoint}$) is different from the polarization of the measuring voltage (V), $z_{sp}(\vec{P}_S\cdot\vec{P}_T)$ changes to $-z_{sp}(\vec{P}_S\cdot\vec{P}_T)$. Then, e.g., Eq.21 changes to $dI/dV(eV) = \frac{1}{2}\rho_S\rho_T[1+\vec{P}_S\vec{P}_T]\cdot exp\Big[-2\kappa(z-z_{sp}(\vec{P}_S\cdot\vec{P}_T))\Big]$.

To understand the DOS term in Eqs.21 and 22 $[\frac{1}{2}\rho_S\rho_T(1+P_SP_T\cos\theta)]$, dI/dV curves were simulated as a function of voltage using this term ($V>0$) (Fig. 30(a)). A 100 %

spin-polarized Gaussian peak in the sample DOS and a 100 % polarization for the tip DOS at the Fermi energy are assumed. Then, when the tip and the sample polarizations are parallel, the Gaussian peak is observed in the dI/dV curve $[\frac{1}{2}\rho_S\rho_T(1+1)]$. When the tip and the sample polarizations are orthogonal, the amplitude of the Gaussian peak decreases $[\frac{1}{2}\rho_S\rho_T(1+0)]$. However, when the tip and the sample polarizations are anti-parallel, the Gaussian peak is completely quenched $[\frac{1}{2}\rho_S\rho_T(1-1)]$.

Figure 30(b-h) shows more practical descriptions of SP-STS measurements and explains different observations in the SP-STS caused by different set point voltages. Here, the tip and the sample magnetizations are assumed to align (anti)parallel, i.e. $\phi = 0°$ and $\theta = 0°$ (180°), then Eqs. 21 and 22 change as follows:

$$dI/dV(eV) = \frac{1}{2}\rho_S(eV)\rho_T(E_F)[1 \pm P_S(eV)P_T(E_F)] \cdot exp\big[-2\kappa(z \pm \Delta z)\big] \quad for\ V > 0, \tag{27}$$

$$dI/dV(eV) = \frac{1}{2}\rho_S(E_F)\rho_T(eV)[1 \pm P_T(eV)P_S(E_F)] \cdot exp\big[-2\kappa(z \pm \Delta z)\big] \quad for\ V < 0. \tag{28}$$

Figure 30(b,c) shows tunneling from the tip DOS at the Fermi level to the unoccupied sample DOS, i.e., a positive bias voltage is applied to the sample. The sample and tip DOS are spin-polarized. The numbers "1", "2", and "3" denote different set point voltages. The configurations of the tip and the sample at "1" (negative voltage) and "2 or 3" (positive voltages) are shown in Figs. 30(d) and 30(e), respectively. Magnetic domains with 180° reversed magnetizations are used as sample. Due to different set point voltages "1" and "2 or 3" and different magnetizations of the sample, four different cases are considered, which are named "A", "B", "C", and "D" as shown in Figs. 30(d) and 30(e). On different magnetic domains the density of the spin-up and spin-down states are reversed. The spin-up and spin-down sample DOS at "1" are the same and there is no difference between spin-up and spin-down sample DOS from 0 eV to the voltage "1" (Fig. 30(b)). The tunneling current is an integral of the dI/dV. Since the integral of the spin-up and spin-down sample DOS below the Fermi level is the same, no difference in the tunneling current is caused between the cases of "A" and "B" in Figs. 30(d) (set point voltage "1"). Thus, the tip-sample separation is the same on the different magnetic domains (Fig. 30(d)). However, at the set point voltage "2", the spin-up sample DOS dominates. Since the tunneling current is an integral of the dI/dV, the difference between spin-up and spin-down DOS from 0 eV to the voltage "2" contributes to the tunneling current. Then, different tunneling currents flow at "C" and "D" at the same tip-sample separation. Due to the constant current mode, the feedback loop varies the tip-sample separation between "C" and "D". For the case of the set point voltage "3", spin-up and spin-down DOS at this voltage are the same. However, the tunneling current is an integral of the DOS from 0 eV to the voltage "3" and a highly spin-polarized DOS is observed around the voltage "2". Thus, at the set point voltage "3", different tip-sample separations on the different magnetic domains are caused by the feedback as well.

Different tip-sample separations have a large influence on the tunneling probability functions. Since the tip-sample separations are the same for the cases "A" and "B", the tunneling probability functions (T_A and T_B) are the same. However, the tip-sample separations are varied for the cases "C" and "D", i.e. different tunneling probability functions (T_C and T_D). The tunneling probability functions shown in Figs. 30(f) and 30(g) are simulated by the following Eq. 29.

$$\begin{aligned} T_A = T_B &= 1.5 \times 10^8 exp(-9.2\sqrt{4+eV/2}) + 1.5 \times 10^8 exp(-9.2\sqrt{4-eV/2}), \\ T_C &= 1.5 \times 10^8 exp(-9.4\sqrt{4+eV/2}) + 1.5 \times 10^8 exp(-9.4\sqrt{4-eV/2}), \\ T_D &= 1.5 \times 10^8 exp(-9.0\sqrt{4+eV/2}) + 1.5 \times 10^8 exp(-9.0\sqrt{4-eV/2}). \end{aligned} \tag{29}$$

An average work function of 4 eV and tip-sample separations of 9.2 Å for the cases "A" and "B", 9.4 Å for case "C", and 9.0 Å for case "D" are used. A proportionality coefficient of 1.5×10^8 (=typical experimentally obtained value) was obtained by a fit to the experimentally obtained dI/dV curves.

dI/dV curves for the cases "A"-"D" are simulated as shown in Figs. 30(h) and 30(i). The sample and the tip DOS shown in Fig. 30(b,c) are used. Polarizations of 50 % for $P_T(E_F)$ and 0 % for $P_S(E_F)$ are assumed. Since the use of the same proportionality coefficient for the positive and the negative voltage sides in T (experimentally the coefficients are different for positive and negative voltages) causes a jump at the Fermi energy, the dI/dV curve of the positive voltage side is offsetted to connect with the dI/dV curve of the negative voltage side .

The dI/dV curve for the case of "A" is shown as the black curve in Fig. 30(h):

$$\begin{aligned} dI/dV(eV) &= \frac{1}{2}\rho_S(eV)\rho_T(E_F)[1 + P_S(eV)P_T(E_F)] \cdot T_A \;\; for\ V > 0, \\ dI/dV(eV) &= \frac{1}{2}\rho_T(eV)\rho_S(E_F)[1 + P_T(eV)P_S(E_F)] \cdot T_A \;\; for\ V < 0. \end{aligned} \tag{30}$$

The dI/dV curve for the case of "B" is shown as the grey curve in Fig. 30(h):

$$\begin{aligned} dI/dV(eV) &= \frac{1}{2}\rho_S(eV)\rho_T(E_F)[1 - P_S(eV)P_T(E_F)] \cdot T_B \;\; for\ V > 0, \\ dI/dV(eV) &= \frac{1}{2}\rho_T(eV)\rho_S(E_F)[1 - P_T(eV)P_S(E_F)] \cdot T_B \;\; for\ V < 0. \end{aligned} \tag{31}$$

The dI/dV curve for the case of "C" is shown as the black curve in Fig. 30(i):

$$\begin{aligned} dI/dV(eV) &= \frac{1}{2}\rho_S(eV)\rho_T(E_F)[1 + P_S(eV)P_T(E_F)] \cdot T_C \;\; for\ V > 0, \\ dI/dV(eV) &= \frac{1}{2}\rho_T(eV)\rho_S(E_F)[1 + P_T(eV)P_S(E_F)] \cdot T_C \;\; for\ V < 0. \end{aligned} \tag{32}$$

The dI/dV curve for the case of "D" is shown as the grey curve in Fig. 30(i):

$$\begin{aligned} dI/dV(eV) &= \frac{1}{2}\rho_S(eV)\rho_T(E_F)[1 - P_S(eV)P_T(E_F)] \cdot T_D \;\; for\ V > 0, \\ dI/dV(eV) &= \frac{1}{2}\rho_T(eV)\rho_S(E_F)[1 - P_T(eV)P_S(E_F)] \cdot T_D \;\; for\ V < 0. \end{aligned} \tag{33}$$

Differences between the black and grey curves in Fig. 30(h) indicate a magnetic contrast in the dI/dV curves. The contrast is only observed above the Fermi level. However, the black and grey curves in Fig. 30(i) show different magnetic contrasts. The magnetic contrast is observed even at negative voltages. This analysis shows that there is a clear influence of the set point voltage on the magnetic contrast observed in the dI/dV spectra.

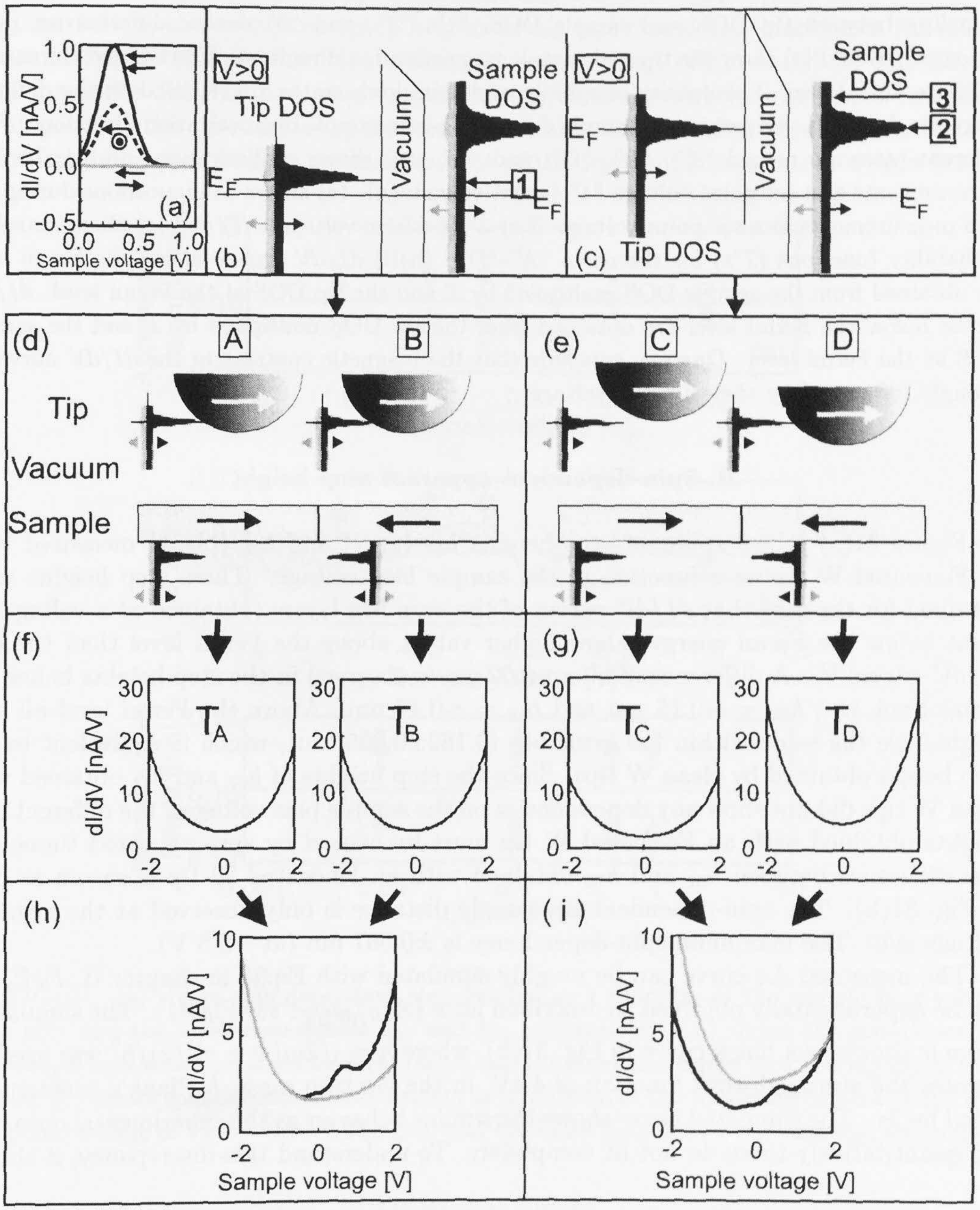

FIG. 30. (a) The dependence of the DOS peak in the dI/dV curve on the polarization directions between the tip and the sample. A 100 % polarized sample DOS ($V > 0$) and a 100 % tip polarization at the Fermi energy are assumed. The black, the grey, and the dashed curves denote the cases that these polarizations are parallel, anti-parallel, and orthogonal, respectively. (b-i) Influence of set point voltage on magnetic contrasts in dI/dV curves. "←" and "→" in DOS models denote spin-down and spin-up DOS, respectively. (b,c) shows a scheme of tunneling between tip DOS and sample DOS. "1", "2", and "3" denote different set point voltages. (d) and (e) show the tip and sample magnetization directions. The tip and the sample DOS are also shown. The density of spin-up and spin-down states are reversed on the different magnetic domains. Arrows in the sample denote in-plane sample magnetization directions. Four different cases are named "A", "B", "C", and "D". (d) shows configurations during the STS measurements at a set point voltage "1" (negative voltage). (e) shows configurations during the STS measurements at a set point voltage "2 or 3" (positive voltage). (f) and (g) show tunneling probability functions (T's) for the cases "A"-"D". (h)(i) dI/dV curves above the Fermi level are obtained from the sample DOS multiplied by T and the tip DOS at the Fermi level. dI/dV curves below the Fermi level are obtained from the tip DOS multiplied by T and the sample DOS at the Fermi level. One can conclude that the magnetic contrast in the dI/dV curves is strongly influenced by the set point voltage.

B. Spin-dependent apparent step height

Figure 31(a) shows apparent step heights h_{67} (grey) and h_{78} (black) measured with an Fe-coated W tip as a function of the sample bias voltage. These step heights were obtained for the case that dI/dV curves of the even Mn layers (obtained at a voltage set point below the Fermi energy) show higher values above the Fermi level than the odd dI/dV curves [12] . A difference of about 0.02 nm is observed in the step heights below the Fermi level, i.e., $h_{67} = \sim 0.15$ nm and $h_{78} = \sim 0.17$ nm. Above the Fermi level all step heights are the same within the error bar (0.162±0.005 nm), which is equivalent to the step height obtained by clean W tips. Since the step heights of h_{67} and h_{78} obtained with clean W tips did not show any dependencies on the sample bias voltages, the different step heights obtained with an Fe-coated W tip must be caused by spin-polarized tunneling. The difference between h_{67} and h_{78} obtained with an Fe-coated W tip is shown as dots in Fig. 31(b). The spin-dependent tip-sample distance is only observed at the negative voltage side. The maximum spin-dependency is ±0.007 nm (at −0.5 V).

The measured Δz curve can be roughly simulated with Eq.26 in chapter II. $P_T P_S(V)$ can be experimentally obtained as described later ($A_{(dI/dV)/T}$: see Fig.41). The simulation curve is shown as a black curve in Fig. 31(b), where $\kappa = \sqrt{2m(\bar{\Phi} \pm eV/2)/\hbar^2}$ was used. $\bar{\Phi}$ denotes the averaged work function of 4 eV, m the electron mass, $\hbar$ Plank's constant divided by 2π. The simulated curve shows the similar behavior as the experimental data, but the quantitatively these do not fit completely. To understand this discrepancy, it should

---

[12] The reason that dI/dV higher at odd layers in Fig. 29 but higher at even layers in Fig. 28(+31) is due to the random tip polarization direction.

be realized that the apparent step heights obtained from Gaussian peaks in the histogram of the STM images already includes an inaccuracy of about ±0.007 nm. Also, the experimentally obtained $A_{(dI/dV)/T}$ only approximately corresponds to $P_T P_S(V)$. Therefore it is difficult to simulate the real spin-dependent tip-sample separation perfectly. At least, one can say that the spin-dependent tip-sample separation has a voltage dependence and the maximum amplitude of Δz is about 0.007 nm.

Figure 31(d) shows apparent step heights of h_{67} (grey) and h_{78} (black) as a function of the tunneling current obtained at the same set point voltage of $V_S = -0.5$ V. The different currents imply different tip-sample separations. When the current was varied two orders of magnitude, the tip-sample separation varies about 0.2 nm. Our results show that the spin-dependent step heights are independent of the tip-sample separation within 0.2 nm.

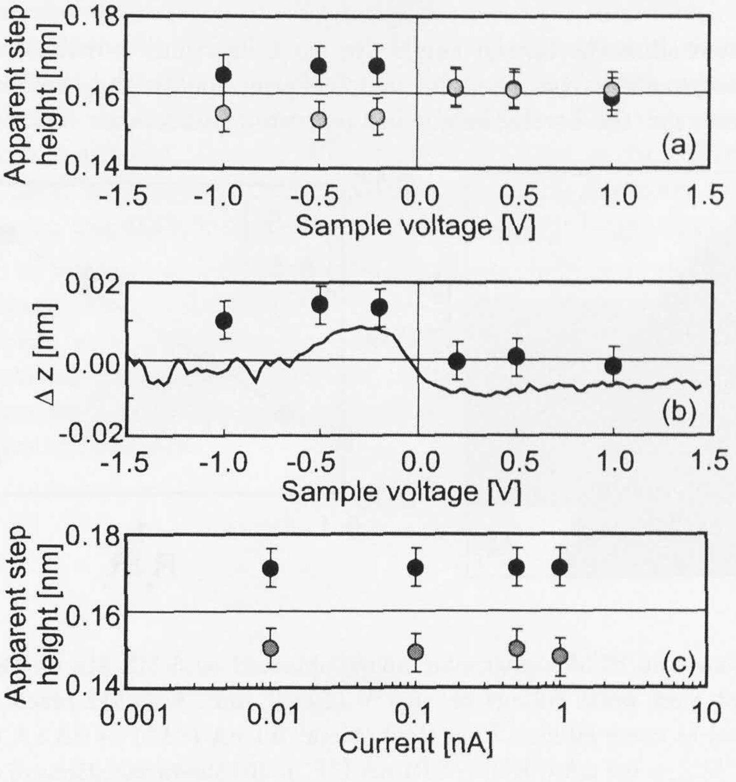

FIG. 31. (a) shows spin-dependent step heights as a function of the sample bias voltage. The grey and the black dots denote h_{67} and h_{78}, respectively. (b) shows the spin-dependent tip-sample separation obtained from (a) (dots) and the simulated curve by following Eq.26 (solid curve). (c) shows spin-dependent step heights as a function of the tunneling current at the same set point voltage of $V_S = -0.5$ V. The grey and the black dots denote h_{67} and h_{78}, respectively.

C. Barrier height

The averaged barrier height ($\bar{\Phi}$) between the tip and the sample was measured with an Fe-coated W tip to check the spin-dependency in the barrier height (Fig. 32). In the same way as described in Fig. 26, the current set point was varied from 0.01 nA to 1 nA during the scanning, while the same voltage set point was used. Figure 32(a) shows an STM image obtained with an Fe-coated W tip on the fifth and the sixth Mn layer. At about every 80 lines the current set point was varied, which explains the different grey scales (each area of 80 lines are marked "A"-"F"). The variation of the tip-sample separation was obtained from the height differences between "A"-"F". The height differences were obtained by measuring distances between Gaussian peaks in the histogram of the Fig. 32(a) (which has been first correctly plane fitted). From the experimentally obtained height differences, the barrier heights of the Mn layers are deduced. The variations of the tip-sample separation as a function of the ratio of R_a/R_b obtained from Fig. 32(a) are shown in Fig. 32(b). The points are fitted to a line. Its slope is proportional to $\bar{\Phi}$. Figure 32(b) shows the same slope for the fifth and the sixth Mn layer, i.e. no spin-dependency in the barrier height is observed.

This is expected since the barrier height (or work function) is defined as the energy required to extract one electron from the sample Fermi energy and the Fermi energy is not spin-dependent, i.e. the barrier height has no spin-dependence.

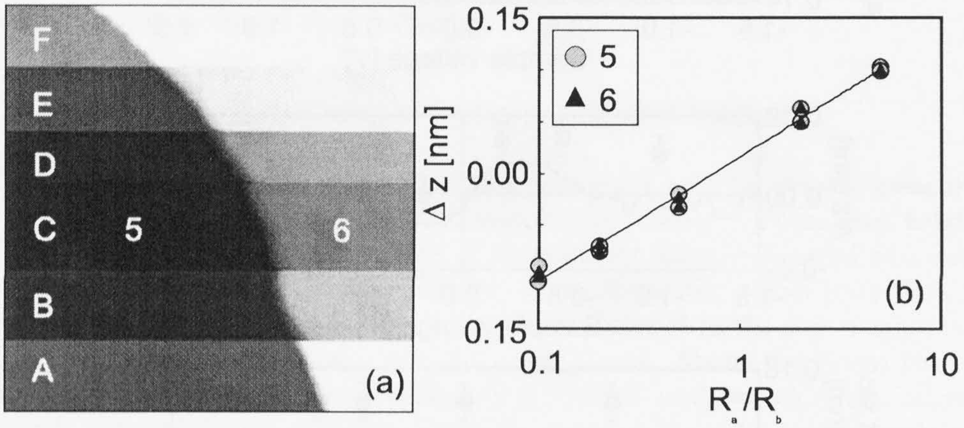

FIG. 32. (a) shows an STM topographic image obtained on 5 ML Mn on Fe(001) with an Fe-coated W tip at a set point voltage of −0.5 V (40×40 nm^2, 512×512 pixels). The current set point was varied at every 80 lines from the bottom: 0.1 nA ("A") → 0.5 nA ("B") → 1 nA ("C") → 0.5 nA ("D") → 0.1 nA ("E") → 0.01 nA ("F"). (b) shows variations of the tip-sample separation obtained from (a) as a function of resistance ratio. From the slope, the averaged barrier height is obtained. No spin dependence is observed, since barrier heights obtained from the fifth and the sixth Mn layer are equal.

D. Atomic-scale magnetic resolution

To check the magnetic resolution of our setup a Mn surface area which includes a hidden Fe step was used. Figure 33(a) shows a SP-STM topographic image obtained with an Fe-coated W tip on the Fe(001) covered by 7 ML Mn at a set point of $V_S = -0.6$ V, $I = 0.5$ nA (70×70 nm^2). A hidden Fe step is running between the arrows in Fig. 33(a).

Figure 33(b) reveals an atomically resolved STM image at a hidden Fe step obtained with a special tip on the surface of 2.5 ML Mn on Fe(001). At the center of the image from bottom to top a hidden Fe step is running. A height difference (~0.02 nm) but no difference in the in-plane lattice constant is observed. Although a step with a 1 ML height (0.165 nm) quenches the DOS peaks due to a broken symmetry (e.g. Fig. 23(b)), the step with a 0.02 nm height does not quench the DOS peaks. Using the W tip no difference was observed in the spectroscopy at the hidden Fe step. However, the Fe-coated W tip detects a change of the magnetic contrast in the spectroscopy map. A dI/dV map at +0.2 V measured at the same area as Fig. 33(a) shows a magnetic contrast across the hidden Fe step (Fig. 33(c)), which directly shows that the Mn magnetization reverses across the hidden Fe step. This also reveals that the hidden Fe step position is an atomic-scale magnetic domain wall. At this area, across the hidden Fe step, an averaged line profile in the dI/dV map was measured (Fig. 33(d)), which was fitted to $c\ \tanh[(x - x_o)/w/2] + b$, where w is defined as the width of the variation of the contrast, x_o denotes the step position and b and c are fitting parameters. Then, w = 0.4 nm was obtained. Thus, magnetic resolution in SP-STS is close to the atomic scale. This value corresponds to the highest magnetic resolution of my SP-STS results. A model of the hidden Fe step area is shown in Fig. 33(e) with experimentally obtained interlayer distances (Fig. 27).

A magnetic tip was made by using a W tip with a radius larger than 300 nm. The lateral resolution of this tip can be estimated as $\Delta x = \sqrt{(2\text{Å})(R + d)} = \sqrt{2(3000 + 10)\text{Å}^2} \approx$ 8 nm. Surprisingly, our results showed a 20 times higher resolution. This is likely caused by an Fe particle with a size smaller than 1 nm sticking out of the tip apex (due to roughness of the tip surface). For example, when one atom is sticking out from the tip apex, more than 90 % of electrons tunnel from this atom. Thus, the local tip radius can become a radius of the atom.

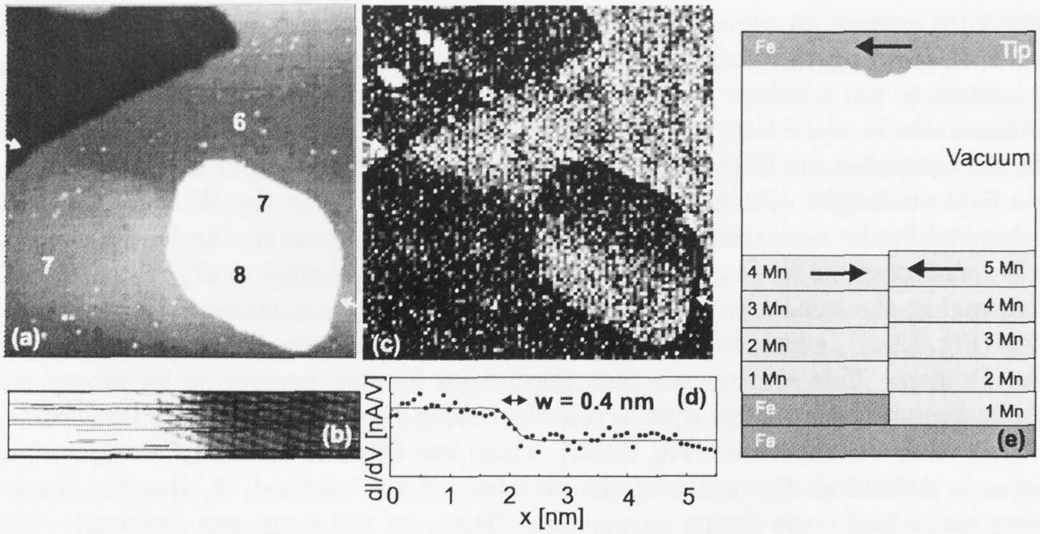

FIG. 33. (a) shows a topographic image obtained with an Fe-coated W tip on 7 ML Mn on Fe(001) ($70 \times 70 \mathrm{nm}^2$, $V_S = -0.6$ V, $I = 0.5$ nA). The numbers denote the thickness of the Mn layers. Two white arrows denote a hidden Fe step. (b) shows an atomically resolved STM image obtained with a special tip on the surface of 2.5 ML Mn on Fe(001) which includes a hidden Fe step. The hidden Fe step is observed at the center of this image. The step height is only 0.02 nm. No difference in the in-plane lattice constant is observed. (c) shows a dI/dV map at +0.2 V obtained at the same area as (a). A magnetic contrast is observed across the Fe hidden step. (d) shows an averaged line profile obtained from the boxed area in (c). This profile is fitted to $c\ \tanh[(x - x_o)/w/2] + b$, where w is defined as the width of the variation of the contrast. $w =$ 0.4 nm was obtained. (e) A tentative model is shown with experimentally obtained interlayer distances on real scale. At the hidden Fe step opposite in-plane magnetizations of Mn layers encounter. Arrows denote magnetization directions.

E. SP-STM on the first Mn(001) layer

A study of a thin antiferromagnetic metal film on a ferromagnetic metal is one of the most important issues to understand the fundamental magnetism. Especially, as an interesting and ideal model, many calculations of magnetic structures for a pure 1 ML Mn on Fe(001) have been reported. As regarding these calculations, Mn atoms form ordered c(2×2) or p(2×2) magnetic structures, which were found to be energetically the most stable [8].

Figures 34(a) and 34(b) reveal SP-STM images of 1.2 ML Mn grown on the Fe(001) whisker at 310 K obtained by Fe-coated W tips. To obtain atomically resolved images the tip scanned at a low resistance set point, which causes a strong tip-sample interaction resulting in scratch-noise in the topographic images (specially near the steps). By a comparison with the atomically resolved image obtained by a clean W tip (Fig. 20) dark spots at lattice sites (black arrows in Figs. 34(a) and 34(b)) can be identified as intermixed Fe atoms and dark spots at hollow sites (white arrows in Figs. 34(a) and 34(b)) as contaminants. Although, to avoid intermixing, the temperature during Mn deposition was 60 K lower than the usual temperature (370 K), intermixed Fe atoms were still observed with a concentration of about 6 %. Nearest neighbor Mn atoms of the intermixed Fe atoms are observed brighter (circles in Figs. 34(a) and 34(b)). Since the intermixed Fe atoms and contaminant have different electronic structures we cannot investigate the magnetic structure near these dark spots. However, no clear ordered magnetic structures such as p(2×2) or c(2×2) were observed, i.e. our SP-STM results did not show any clear magnetic structures in contradiction to the reported calculations. Possibly, the measurement temperature (room temperature) is higher than the Neel temperature of the magnetic ordering. Furthermore, the intermixed Fe atoms may destroy a potential magnetic ordering.

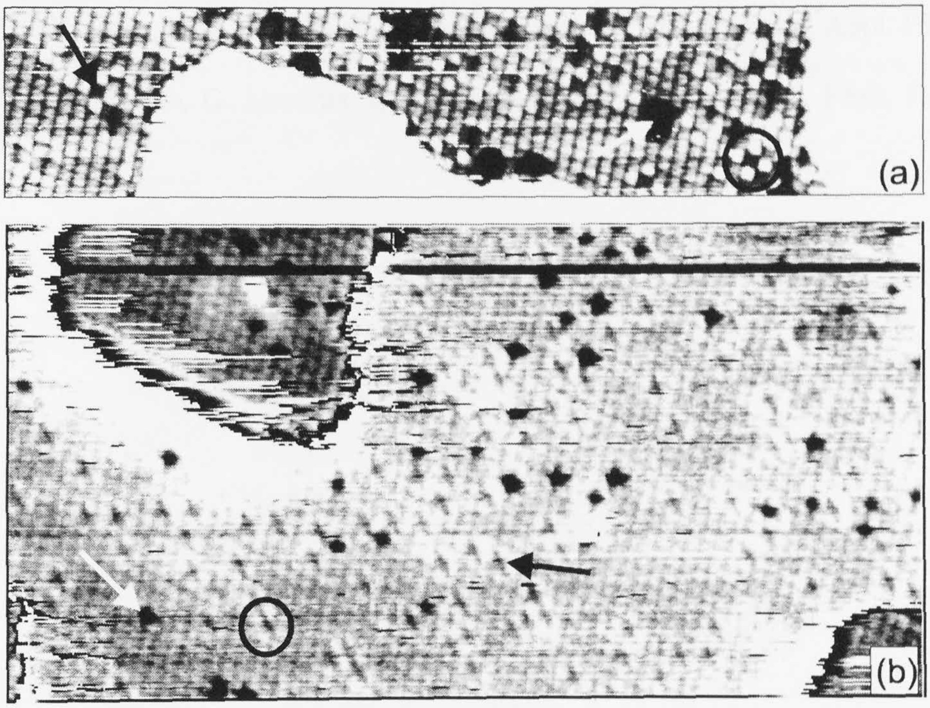

FIG. 34. Atomically and chemically resolved SP-STM images obtained with Fe-coated W tips on the first Mn layer on Fe(001) at 310 K. (a) and (b) were obtained on different days. Both images show p(1×1) lattice atoms and dark spots. The dark spots at hollow (white arrows) and atomic sites (black arrows) are identified as contaminants and intermixed Fe atoms, respectively. (a)20×4.1 nm^2, $V_S = -0.003$ V, $I = 6.6$ nA (b)20×10 nm^2, $V_S = -0.004$ V, $I = 36$ nA. Circles denote the four bright atoms around one intermixed Fe atom.

F. Conclusion

A magnetic contrast was obtained with Fe-coated W tips between ultrathin bct Mn films (>3 ML) grown on Fe(001) whiskers by SP-STS. This result directly showed that one Mn atomic-layer (bigger than 1 nm) has an in-plane magnetization and couples antiferromagnetically with the Mn layers below and above. Magnetic contrast was observed in $I(V)$, dI/dV and $(dI/dV)/(I/V)$ curves. $I(V)$ and dI/dV show a much higher magnetic contrast (15-20 %) than $(dI/dV)/(I/V)$ (~5 %) above the Fermi energy. Spin-dependent step heights were obtained by SP-STM, which showed a voltage dependence but no tip-sample separation dependence within ±0.007 nm. Spin-dependent barrier heights were never observed. Using an area on Mn layers grown on a hidden Fe step our SP-STS was found to resolve magnetic structures with a resolution of 0.4 nm. By SP-STM we could not detect ordered magnetic structures on the first Mn layer, whereas calculations suggested.

REFERENCES

[1] T.K. Yamada, M.M.J. Bischoff, T. Mizoguchi, and H. van Kempen, Appl. Phys. Lett. **82** (2003) 1437.

[2] S. Andrieu, M. Finazzi, Ph. Bauer, H. Fischer, P. Lefevre, A. Traverse, K. Hricovini, G. Krill, and M. Piecuch, Phys. Rev. B **57** (1998) 1985.

[3] D.A. Tulchinsky, D.T. Pierce, A.D. Davies, J.A. Stroscio, J. Unguris, and R.J. Celotta, J. Magn. Magn. Mater. **212** (2000) 91.

[4] T.G. Walker and H. Hopster, Phys. Rev. B **48** (1993) 3563.

[5] J.C.S. Kools, IEEE Trans. Mag. **32** (1996) 3165.

[6] R. Wiesendanger, H.J. Güntherodt, G. Güntherodt, R.J. Gambino, and R. Ruf, Phys. Rev. Lett. **65** (1990) 247.

[7] T.K. Yamada, M.M.J. Bischoff, T. Mizoguchi, and H. van Kempen, Appl. Phys. Lett. **82** (2003) 1437.

[8] O. Elmouhssine, G. Moraïtis, C. Demangeat, and J.C. Parledas, Phys. Rev. B **55** (1997) R7410.

VI. ORIGIN OF THE MAGNETIC CONTRAST IN SP-STS

A. Spin-polarized $(dI/dV)/T$

To be useful as a reliable technique, it is of utmost importance to understand the origin of the magnetic contrast in SP-STS images. Although it was already reported that this magnetic contrast is related to the spin-polarized peak in spectroscopy [2], this relation is not straightforward due to the influence of the tunneling probability. Kleiber *et al.* obtained the highest contrast in the dI/dV maps obtained on Cr(001) close to the surface state energy of −0.02 V but commented on a contrast inversion inherent to the closed-loop constant current mode which was used [1]. In a more recent publication, it was reported that the highest contrast is obtained around ±0.25 V [2].

To obtain the spin-dependent DOS peaks without the influence of the tunneling probability the normalization technique proposed by Ukraintsev was used. Figures 35(a) and 35(b) show $(dI/dV)/T$ curves averaged over 30 single curves measured on Mn films thicker than three layers with a clean W tip and an Fe-coated W tip, respectively. dI/dV curves were obtained within a large voltage range from −2 V to +3 V. Normalized dI/dV curves measured with the clean W tip show two peaks: a strong peak around +0.8 V and a weak peak around −0.5 V (see also Fig. 25). In Fig. 35(b), normalized dI/dV curves measured on even layers (grey curve) and odd layers (black curve) show two peaks at the same energies as those obtained with the clean W tips. However, now the amplitude of both peaks oscillates with a period of two layers. The curves measured on even and odd layers cross around the Fermi level. In the approximation of ref. [3], $(dI/dV)/T$ at positive (negative) voltages is proportional to the sample (tip) DOS multiplied by the tip (sample) DOS at the Fermi level [4]. Thus, the peaks at +0.8 V and −0.5 V are found to be spin-dependent, which causes magnetic contrast in the SP-STS maps.

According to the theory the obtained $(dI/dV)/T$ shows the sample (tip) DOS at the contact point, i.e. when the tip-sample separation is zero. However, it should be noted that s, p, d and f-state electrons have different decay factors. Since dI/dV represents a sum of wave functions including all decay factors, dI/dV corresponds to the DOS at the tip position if the tip has no special DOS features (i.e. s-state, otherwise the tip states will be convoluted as well). The DOS changes as the distance from the surface increases. Usually, as the distance increases, contours of constant state-density tend to smooth out. According to ref. [5] a +0.2 V peak on Fe(001) in dI/dV becomes smaller as the distance increases. T represents roughly the average of all these decays since T includes only one decay factor ("b" in Eq. 17). One T cannot get rid of the z dependence completely, and $(dI/dV)/T$ represents a sum of wave functions squared (including their own decay factors) divided by an average decay factor, i.e. $(dI/dV)/T = (\psi_s\psi_t \exp(-(\kappa_s + \kappa_t)z) + \psi_p\psi_t \exp(-(\kappa_p + \kappa_t)z) + \psi_d\psi_t \exp(-(\kappa_d + \kappa_t)z) + \cdots) \,/\, \exp(-2\kappa_{ave}z_{ave})$, where ψ_s, ψ_p, and ψ_d denote the wave functions of the sample s, p, and d states, respectively, and ψ_t the wave function of the tip. (Only one tip state is assumed.) If only one tip state and only one sample state contribute to the tunneling, $(dI/dV)/T$ represents the surface sample DOS(V) times tip DOS(E_F).

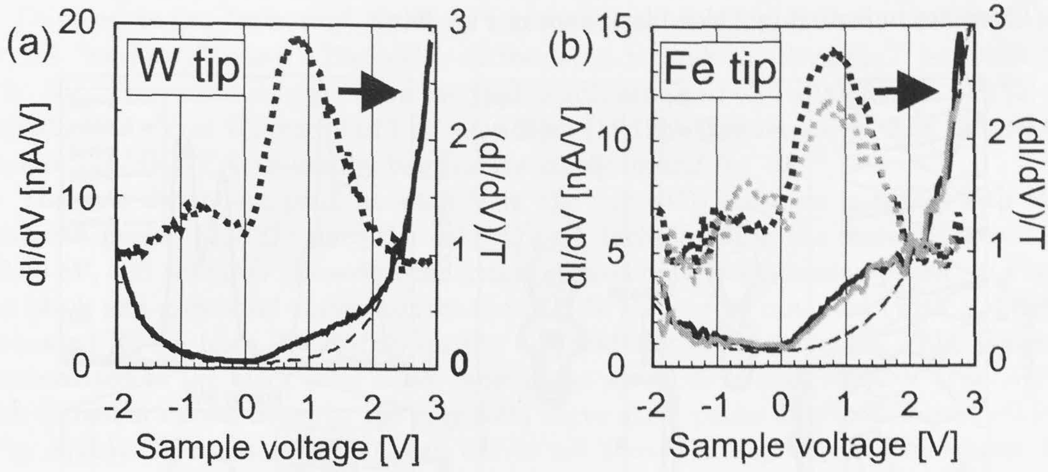

FIG. 35. (a) and (b) show dI/dV curves normalized by the voltage-dependent tunneling probability functions, which were obtained with a clean W tip and an Fe-coated W tip, respectively, on Mn films thicker than three layers. Solid and dotted curves are the dI/dV and the $(dI/dV)/T$ curves, respectively. Tunneling probability functions (dashed curves) were obtained by a fit to the dI/dV curves. In (b), black and grey curves are representative of the odd and the even layer, respectively.

B. Band structure calculations

3*d* metals with a bcc structure such as Fe or Cr have a localized *d* surface state on the (001) surface. On the other hand, Mn, which is between Fe and Cr in the periodic table, has a complicated structure in bulk. An interesting point is whether an artificial bct Mn(001) films also shows d_{z^2} surface states. To determine the nature of the spin-dependent peaks in the $(dI/dV)/T$ curves (Fig. 35(b)), band structure calculations were carried out by Heijnen of the theoretical physics department (Electronic Structure of Materials) of the University of Nijmegen using the Vienna Ab initio Simulation Program (VASP) [6,7]. It is based on spin density functional theory and the projector augmented wave (PAW) method [8,9] with non-local corrections to the exchange and correlation taken into account by a generalized gradient approximation (GGA). An eight layer slab with the experimental values for the in-plane (2.87 Å) and out-of-plane (2×1.64 Å) lattice constants was used. Furthermore, an antiferromagnetically stacking of the Mn(001) layers was used [10].

Peaks are found above the Fermi level in the "minority" band of the surface DOS [13]. To confirm if these peaks are caused by surface states which protrude far enough into the

---

[13] Here, "minority" and "majority" are defined by the numbers of the spin-up and the spin-down states below the Fermi energy.

vacuum to be detected by the STM tip, bands with the d_{z^2} character at $\overline{\Gamma}$ are selected [5]. These are indicated by thick black lines in Fig. 36(a).

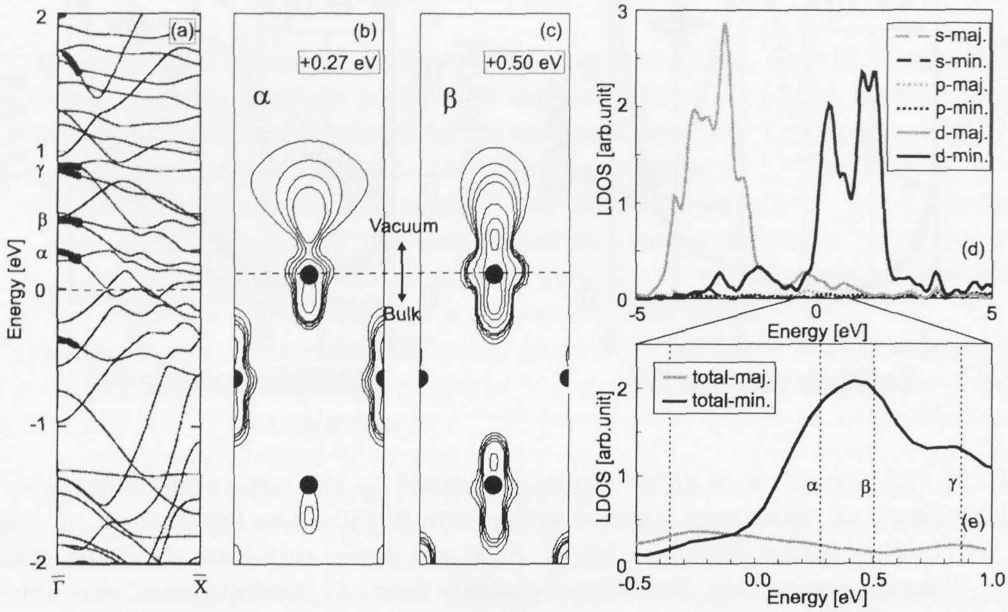

FIG. 36. (a) Band structure of an eight-layer Mn(001) slab. The plot shows both "majority" and "minority" bands, which are equivalent for this even-layered antiferromagnetically ordered slab. The magnetization for each layer is defined by the difference in integrated local DOS of the "majority" and "minority" bands. Thick black lines indicate d_{z^2}-like states around $\bar{\Gamma}$; the dashed line the Fermi level. α, β, and γ could contribute to the experimentally observed +0.8 V peak. (b) and (c) show the isocharge density distributions of the α and the β state at $\bar{\Gamma}$ in a (110) plane. Dots and dashed lines indicate atom positions and the boundary between vacuum and bulk, respectively. (d) shows the local density of states (LDOS) of the bct-Mn(001) surface. The minority and the majority LDOS of s, p, and d-state are shown in an energy range between -5 V and $+5$ V. (e) shows the total minority and majority LDOS in a smaller energy range between -0.5 V and $+1.0$ V.

Three bands are possible candidates for the experimentally observed empty state $(dI/dV)/T$ peak: band α at 0.27 eV, β at 0.50 eV, and γ at 0.87 eV above the Fermi level. Our calculations show the DOS at the Mn(001) surface. dI/dV shows the sample DOS at the tip position and $(dI/dV)/T$ shows the sample surface DOS and the tip surface DOS if there would be only one decay factor. To check the distribution of each state in the vacuum the surface charge density distribution was analyzed. A plot of the distribution of these three bands shows that the last one has a stronger decay into the vacuum. The first two show surface state like behavior and their charge densities are plotted in Figs. 36(b) and 36(c), i.e. the decay factor for the states α and β is similar, but different from the decay factor of the state γ. From the charge density maps we can estimate that the states α and β are surface states since they exist only at the surface layer. The state γ is identified as a surface resonance since this state exists not only at the surface layer but also slightly spreads into the bulk layer.

Opposed to the "minority" band, no surface states were found above the Fermi level for the "majority" band. The width of the +0.8 V peak in $(dI/dV)/T$ is about 1 V (Fig. 35). This width is larger than the peak width obtained on Fe(001) (0.13 eV) [5] and Cr(001) (0.2 eV at RT and 0.015 eV at 4.2 K) [11,12]. One reason is that the +0.8 V peak in $(dI/dV)/T$ is caused by two surface states: α and β.

The spin-dependent peak at +0.8 V in the $(dI/dV)/T$ curves is fitted with three Gaussian peaks (Fig. 37) since the +0.8 V peak includes three d_{z^2} states at +0.27 eV, +0.50 eV, and +0.87 eV. However, the fitting showed only two Gaussian peaks. In Fig. 37 the black and grey solid curves denote the $(dI/dV)/T$ curves obtained (with a different Fe-coated W tip from Fig. 35(b)) on the odd and the even Mn layers. The Gaussian curves fitted to the black solid curve show peaks at +0.49 V and +0.92 V (Fig. 37(a)). The Gaussian curves fitted to the grey solid curve show peaks at +0.47 V and +0.94 V (Fig. 37(b)). The obtained Gaussian curves are shown in Fig. 37(c). This shows that both peaks are spin-dependent. The peak around +0.48 V likely comprises the states α and β. This peak shows a polarization of 19 % [14] . On the other hand, the peak around +0.93 V likely comprises the state γ. This state has a strong decay into the vacuum. This peak shows a polarization of 10 %. Then, the polarization of the states α and β is likely higher than the polarization of the state γ. Since the state γ a the different decay factor compared to the states α and β, the $(dI/dV)/T$ (using only one T) may not exclude the tip-sample separation dependence completely for the all states α, β, and γ. This may cause the different polarization.

Below the Fermi level a weak d_{z^2} state is found at −0.37 eV in the "majority" band: its charge density does not show a strong vacuum contribution. Nevertheless, since the weak peak around −0.5 V in the $(dI/dV)/T$ curve is reproducibly observed with various tips (see Figs. 35(b) and 37), we think it is a real feature of the Mn(001) electronic structure. Therefore, we found that three states in the "minority" band contribute to the peak at +0.8 V in the $(dI/dV)/T$ curves, while one surface state in the "majority" band contributes to the peak at −0.5 V. Thus, the artificial Mn(001) also shows highly polarized surface states similar to Cr and Fe.

---

[14] This polarization of the Gaussians corresponds to $P_T(E_F)P_S(V)$.

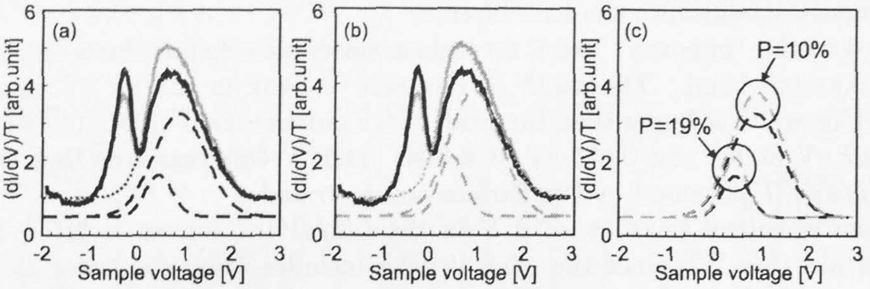

FIG. 37. The +0.8 V peak in the experimentally obtained $(dI/dV)/T$ curves on the odd (black solid curve) and the even (grey solid curve) Mn layers is fitted with two Gaussian peaks. (a) The peak at +0.8 V in the $(dI/dV)/T$ obtained on the odd Mn layer is fitted with two Gaussian curves. The fitted curve and the obtained Gaussians are shown as a dotted curve and dashed curves, respectively. (b) The peak at +0.8 V in the $(dI/dV)/T$ obtained on the even Mn layer is fitted with two Gaussian curves. The fitted curve and the obtained Gaussians are shown as a dotted curve and dashed curves, respectively. (c) The obtained Gaussians in (a,b) are shown. Two spin-dependent peaks are observed.

C. Conclusion

By normalizing dI/dV curves with the fitted tunneling probability function with offsetted Gaussian curves, we found two spin-dependent peaks at +0.8 V and −0.5 V on bct Mn(001) surface (>3 ML). Band structure calculations showed that two d_{z^2} surface states and a d_{z^2} surface resonance in the "minority" band above the Fermi energy contribute to the +0.8 V spin-polarized peak. Although bcc-Fe(001) and bcc-Cr(001) are known to have a highly spin-polarized d surface state, here it was found that, the artificial bct-Mn(001) has the similar states.

REFERENCES

[1] M. Kleiber, M. Bode, R. Ravlić, and R. Wiesendanger, Phys. Rev. Lett. **85** (2000) 4606.

[2] M. Kleiber, M. Bode, R. Ravlić, N. Tezuka, R. Wiesendanger, J. Magn. Magn. Mater. **240** (2002) 64.

[3] V.A. Ukraintsev, Phys. Rev. B **53** (1996) 11176.

[4] The different amplitudes of the $(dI/dV)/T$ curve in Fig. 35(a) and the average of the even and odd $(dI/dV)/T$ curves in Fig. 35(b) is related to the different Fermi level DOS of the Fe-coated tip and the W tip.

[5] J.A. Stroscio, D.T. Pierce, A. Davies, R.J. Celotta, and M. Weinert, Phys. Rev. Lett. **75** (1995) 2960.

[6] G. Kresse and J. Hafner, Phys. Rev. B **47** (1993) 558; **49** (1994) 14251.

[7] G. Kresse and J. Furthmüller, Phys. Rev. B **54** (1996) 11169.

[8] P.E. Blöchel, Phys. Rev. B **50** (1994) 17953.

[9] G. Kresse and D. Joubert, Phys. Rev. B **59** (1999) 1758.

[10] D.A. Tulchinsky, D.T. Pierce, A.D. Davies, J.A. Stroscio, J. Unguris, and R.J. Celotta, J. Magn. Magn. Mater. **212** (2000) 91.

[11] M. Kleiber, M. Bode, R. Ravlić, and R. Wiesendanger, Phys. Rev. Lett. **85** (2000) 4606.

[12] O.Yu. Kolesnychenko, R. de Kort, M.I. Katsnelson, A.I. Lichtenstein and H. van Kempen, Nature **415** (2002) 507.

VII. HOW TO GET QUANTITATIVE INFORMATION FROM SP-STS

Various methods for extracting quantitative information, about the sample polarization from SP-STS, were reported [1,2]. However, these methods include a certain ambiguity. For example, when extracting the sample polarization from the SP-STS results one encounters the problem that for every set point voltage the tip-sample distance (and so the tunneling probability) is different for the even and odd Mn layers. This is due to the SP part of the tunnel current which has different bias voltage dependencies for even and odd layers.

A. Asymmetry in $I(V)$

Figures 38(a) and 38(b) show $I(V)$ curves obtained on negative and positive voltage set points, respectively. The black and grey curves were obtained on the odd and the even Mn layers, respectively. $I(V)$ curves obtained on the odd and the even Mn layers at a negative voltage set point show differences above the Fermi energy (Fig. 38(a)), while $I(V)$ curves obtained at a positive voltage set point show differences below the Fermi energy (Fig. 38(b)). These differences can be explained by Fig. 30: the tunneling between a SP tip and different sample magnetic domains indirectly causes different tip-sample separations, and consequently different tunneling probabilities. Figures 38(c) shows the asymmetry of the $I(V)$ curves ($A_{I(V)}$), which is defined as $A_{I(V)} = [I(V)_{odd} - I(V)_{even}]/[I(V)_{odd} + I(V)_{even}]$, where $I(V)_{odd}$ and $I(V)_{even}$ are $I(V)$ curves obtained on the odd and the even Mn layers, respectively. The solid curve obtained from Fig. 38(a) (negative voltage set point) shows an about 20 % asymmetry above the Fermi level and almost no asymmetry below the Fermi level. The dashed curve obtained from Fig. 38(b) (positive voltage set point) shows an about 20 % below the Fermi level and almost no asymmetry above the Fermi level. Thus, $A_{I(V)}$ is strongly influenced by the voltage set point and quantitative information cannot be straight forwardly obtained from $A_{I(V)}$.

Wulfhekel *et al.* obtained the tunnel magnetoresistance by measuring $A_{I(V)}$ [3]. However, their case is different. The magnetization of the soft-magnetic material tip is switched by 40 kHz magnetic fields to detect the sample magnetization. This frequency is higher than the cutoff of the tunneling feedback loop. Thus, the obtained $I(V)$ does not include a spin-dependent tip-sample separation dependence. The obtained $A_{I(V)}$ resembles our $A_{(dI/dV)/T}$. Also, Wulfhekel *et al.* measured magnetic structures on Mn layers on Fe(001)-whisker with a ring tip [4] and their $A_{I(V)}$ showed the same feature as our $A_{(dI/dV)/T}$, while the amplitude is 10 times smaller [15] .

---

[15] The difference seems to be caused by large different tip-sample separations. (With our setup the tip-sample separation is around 0.9 nm (see chapter IV)). Also, a different tip polarization could have an influence.

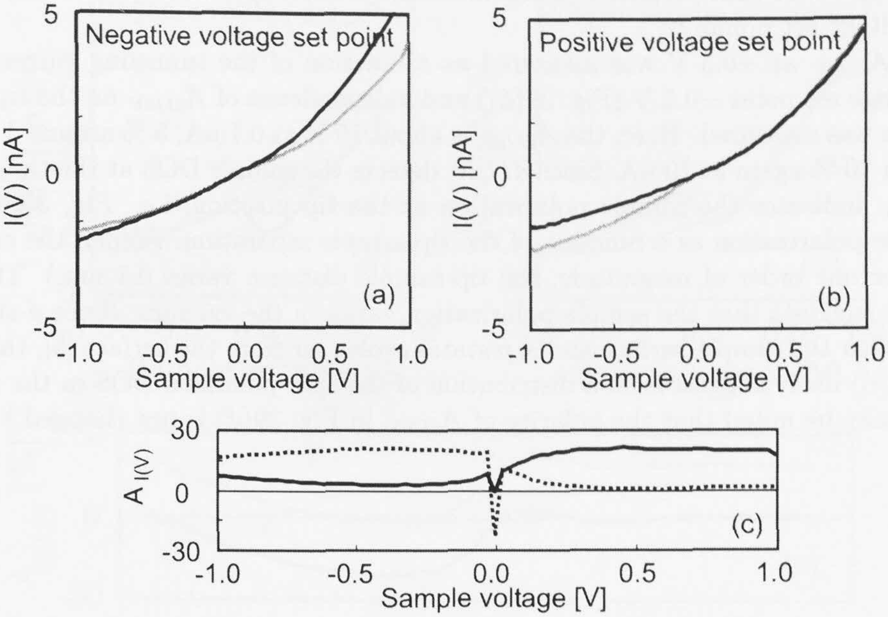

FIG. 38. (a) and (b) show $I(V)$ measurements with an Fe-coated W tip at negative- ($V_S = -0.5$ V, $I = 0.5$ nA) and positive-voltage set point ($V_S = +0.5$ V, $I = 0.5$ nA), respectively, representative of the even (grey curve) and the odd layers (black curve) (>3 ML). (c) shows the asymmetry in the $I(V)$ curves. Solid and dotted curves are obtained from (a) and (b), respectively. In (c), sharp peaks at 0 V are caused by 0nA/0nA, which has no physical meaning.

B. Asymmetry in dI/dV

Figures 39(a) and 39(b) show dI/dV curves measured on the even and the odd layers (>3 ML) at negative- ($V_S = -0.5$ V) and positive-voltage set point ($V_S = +0.5$ V). The dI/dV curves measured at the positive-voltage set point are clearly different from the ones measured at the negative-voltage set point. Figure 39(c) shows the asymmetry in the dI/dV curves of Figs. 39(a) and 39(b), which is defined as $A_{dI/dV} = [(dI/dV)_{even} - (dI/dV)_{odd}]/[(dI/dV)_{even} + (dI/dV)_{odd}]$, where $(dI/dV)_{even}$ and $(dI/dV)_{odd}$ are dI/dV curves obtained on the even and the odd layers. $A_{dI/dV}$ also shows similar results as $A_{I(V)}$. It is clearly influenced by the set point. Since the odd and the even Mn layers have different in-plane magnetization directions, dI/dV would show a peak only on the odd (or even) layers if the tip has a 100 % polarization, i.e. the magnetic tip only detects spin-up or spin-down DOS. However, due to the closed feedback during the STS measurements, the tip moves backward and forward on different terraces since one terrace has a spin-up DOS but the other does not. Consequently, the tip-sample separation varies on different terraces, which has a strong influence on the contrast in SP-STS images. Thus, quantitative information from the $A_{dI/dV}$ is complicated and not straightforward to interpret since distance/voltage dependencies are convoluted. Although Wiesendanger *et al.* obtained the sample polarization by using $A_{dI/dV}$ which showed a good agreement with the results of spin-polarized photoemission spectroscopy, this applies only for well chosen voltage set points [2].

Also, $A_{dI/dV}$ at +0.3 V was measured as a function of the tunneling current at the same voltage set point −0.2 V (Fig. 39(d)) and a dependence of $A_{dI/dV}$ on the tip-sample separation was measured. Here, the $A_{dI/dV}$ is about 15 % at 0.1 nA, 5 % around 1 nA, and more than 10 % again at 10 nA. Since dI/dV detects the sample DOS at the tip position, the $A_{dI/dV}$ indicates the sample polarization at the tip position, i.e. Fig. 39(d) shows the sample polarization as a function of the tip-sample separation. (When the current is varied over one order of magnitude, the tip-sample distance varies 0.1 nm.) Therefore, this result suggests that the sample polarization varies in the vacuum. Since *d*-states are localized near the sample surface and s, p-states evolve far from the surface [5], the results in Fig. 39(d) likely suggest such a distribution of the spin-polarized DOS in the vacuum. (Also, it may be noted that the polarity of $A_{dI/dV}$ in Fig. 39(d) is not changed.)

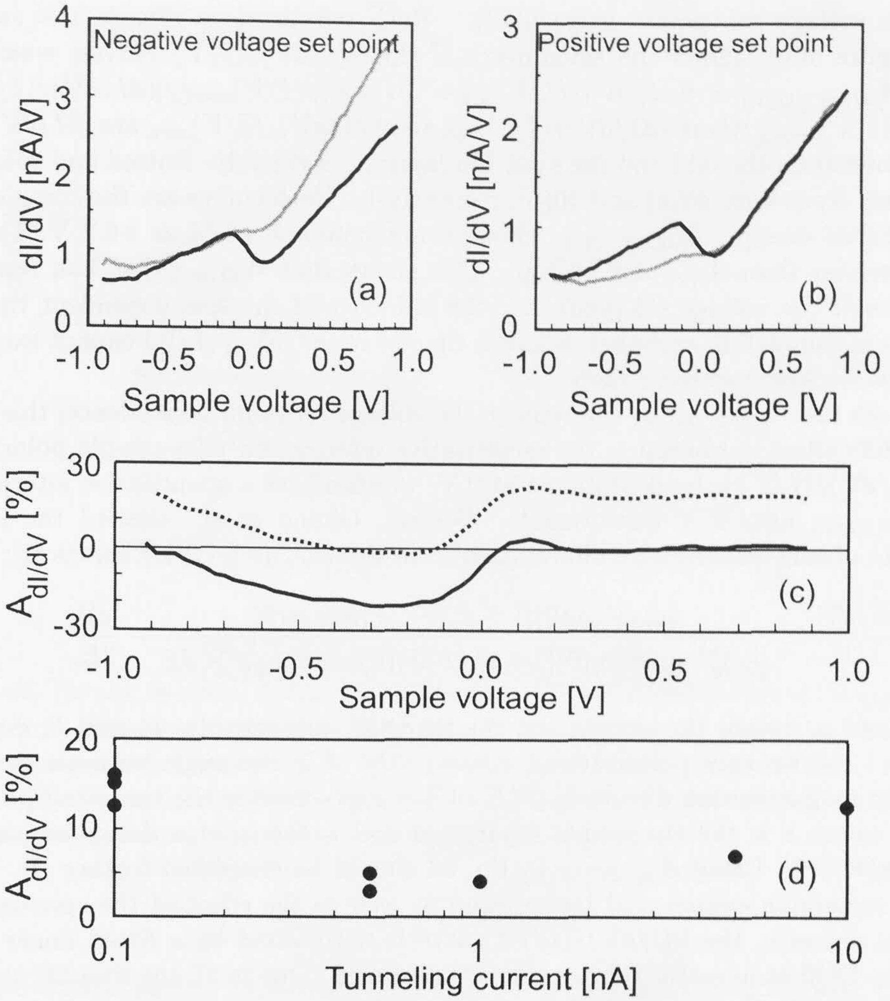

FIG. 39. (a) and (b) show dI/dV measurements obtained with an Fe-coated W tip at negative- ($V_S = -0.5$ V, $I = 0.5$ nA) and positive-voltage set point ($V_S = +0.5$ V, $I = 0.5$ nA), respectively, representative of the even (grey curve) and the odd layers (black curve) (>3 ML). (c) shows the asymmetry in the dI/dV curves. Dotted and solid curves are obtained from (a) and (b), respectively. (d) Dependence of the contrast at +0.3 V in the dI/dV curves on the current set point at the same set point voltage of −0.2 V.

C. Asymmetry in $(dI/dV)/(I/V)$

To solve the problems which we encountered for $A_{I(V)}$ and $A_{dI/dV}$, normalizing dI/dV by I/V was used by Okuno *et al.* [1].

The $(dI/dV)/(I/V)$ normalization cannot exclude the exponential background completely [6]. This gives rise to a shift of the peak energy position [7], which becomes larger at higher voltages. In Figs. 40(a) and 40(b), the peak even disappears in the background.

Figures 40(a) and 40(b) show $(dI/dV)/(I/V)$ curves obtained at a negative and a positive voltage set point, respectively. Both curves show almost the same features. Figure 40(c) shows the asymmetry of the $(dI/dV)/(I/V)$ curves, which is defined as $A_{(dI/dV)/(I/V)} = [(dI/dV)/(I/V)_{odd} - (dI/dV)/(I/V)_{even}]/[(dI/dV)/(I/V)_{odd} + (dI/dV)/(I/V)_{even}]$, where $(dI/dV)/(I/V)_{odd}$ and $(dI/dV)/(I/V)_{even}$ are $(dI/dV)/(I/V)$ curves obtained on the odd and the even Mn layers, respectively. Dotted and solid curves are obtained from Figs. 40(a) and 40(b), respectively. Both curves are the complete same near the Fermi energy. $A_{(dI/dV)/(I/V)}$ shows a maximum of +5 % at +0.2 V. This value is much smaller than $A_{I(V)}$ and $A_{dI/dV}$. This shows that $A_{(dI/dV)/(I/V)}$ can remove the dependence of the voltage set point, i.e. the influence of the spin-dependent tip-sample separation is completely excluded, whereas the use of $(dI/dV)/(I/V)$ cannot exclude the exponential background completely.

Although the $A_{(dI/dV)/(I/V)}$ can remove the voltage set point dependence, this method still has difficulties in obtaining the quantitative information (the sample polarization). First, $(dI/dV)/(I/V)$ is by definition 1 at 0 V, which makes a quantitative interpretation of $A_{(dI/dV)/(I/V)}$ near 0 V questionable. Second, Okuno *et al.* showed the following equation to obtain quantitative information from the $(dI/dV)/(I/V)$ curves [1]:

$$\frac{dI/dV}{I/V} \cong \frac{\rho_s(eV)\rho_t(0)[1 + P_s(eV)P_t(0)\cos\theta]}{\frac{1}{eV}\int_0^{eV} \rho_s(E)\rho_t(0)[1 + P_s(E)P_t(0)\cos\theta]\frac{T(E,eV)}{T(eV,eV)}dE} - \frac{eV}{2E_\kappa}, \qquad (34)$$

where ρ_s and ρ_t denote the sample and the tip DOS, respectively. P_s and P_t denote the sample and the tip spin polarizations, respectively. θ is the angle between the sample and the tip magnetization direction. $T(E, eV) = exp(-2\kappa z)$ is the tunneling probability function, where z is the tip-sample separation and κ the inverse decay length. E_κ is $(\hbar^2/2m)(\kappa(V)/z)$. Using $A_{(dI/dV)/(I/V)}$ Eq. 34 should be simplified further [1]. To subtract the remaining exponential background as well as the effect of the spin-dependent tip-sample distance, the $(dI/dV)/(I/V)$ curve is normalized by a fitted linear line. A uniform tip DOS at negative voltage side was assumed. Due to all the simplifications and assumptions made, the obtained P_s is not very reliable.

Thus, one can conclude that with this method it is not straightforward to get quantitative information from SP-STS. However, with this method it is possible to remove the voltage set point dependence.

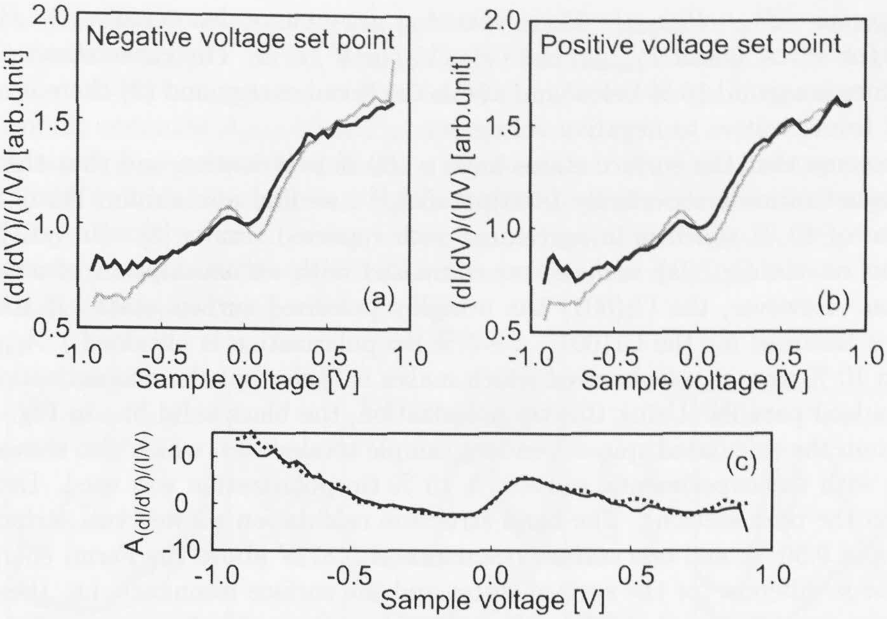

FIG. 40. (a) and (b) show $(dI/dV)/(I/V)$ measurements obtained with an Fe-coated W tip representative of the even (grey curve) and the odd Mn layers (black curve) (>3 ML). (a) and (b) were obtained at a negative- ($V_S = -0.5$ V, $I = 0.5$ nA) and a positive-voltage set point ($V_S = +0.5$ V, $I = 0.5$ nA), respectively. (c) shows the asymmetry in the $(dI/dV)/(I/V)$ curves. Dotted and solid curves are obtained from (a) and (b), respectively.

D. Asymmetry in $(dI/dV)/T$

To recover the sample DOS from the dI/dV curve, the normalization with the tunneling probability function (T) is the best way (see chapter II). The asymmetry of $(dI/dV)/T$ curves is defined as $A_{(dI/dV)/T} = [(dI/dV)/T_{odd} - (dI/dV)/T_{even}]/[(dI/dV)/T_{odd} + (dI/dV)/T_{even}]$, where $(dI/dV)/T_{odd}$ and $(dI/dV)/T_{even}$ denote the $(dI/dV)/T$ curve obtained on the odd and the even Mn layers, respectively. Then, $A_{(dI/dV)/T} = P_{tip}(E_F) \cdot P_{sample}(V)$ for V>0 and $P_{sample}(E_F) \cdot P_{tip}(V)$ for V<0 (see also Eqs. 15, 37, and 38).

Figures 41(a)-(c) show dI/dV curves (solid curves), the fitted tunneling probability functions (dashed curves), and the $(dI/dV)/T$ curves (dotted curves). Black and grey curves are obtained on the odd and the even Mn layers, respectively. Figures 41(a) and 41(b) were obtained by the same Fe-coated W tip. Figure 41(c) was obtained by a different Fe-coated W tip. Figures 41(a) and (c) were obtained at a negative voltage set point ($V_S = -0.5$ V). Figure 41(b) was obtained at a positive voltage set point ($V_S = +0.5$ V). All $(dI/dV)/T$ curves show a clear spin-dependent peak at +0.8 V.

The asymmetries in Fig. 41(d) are obtained from the $(dI/dV)/T$ curves in Fig. 41(c). Changes in the fitting parameters produce errors in the asymmetries of ±2 %. The shape of the curve is similar to $A_{dI/dV}$ and the $A_{(dI/dV)/(I/V)}$. Since the $A_{(dI/dV)/T}$ was obtained form the dI/dV curves showing the highest magnetic contrast (~15-20 %), the tip and sample polarizations are believed to be (anti-)parallel, i.e. $P_{tip} \cdot P_{sample} \cos\theta =$

$P_{tip} \cdot P_{sample}$ (or $-P_{tip} \cdot P_{sample}$). Then, this $A_{(dI/dV)/T}$ curve denotes directly $P_{tip}(E_F) \cdot P_{sample}(V) for\ V > 0$ and $P_{sample}(E_F) \cdot P_{tip}(V) for\ V < 0$. The curve shows that: (1) the maximum is around 10 % below and above the Fermi energy and (2) there is a change of polarity from positive to negative voltages.

If we assume that the surface states have a 100 % polarization and that the tip and sample magnetization are perfectly (anti)parallel [16] , we find a minimum Fermi level tip polarization of 10 % which is in agreement with reported results [8]. (In ref. [8] 17 % polarization on the Cr(001) surface was estimated with an assumption of a 44 % tip polarization. However, the Cr(001) has a highly polarized surface state. If 100 % polarization is assumed for the Cr(001), a ~7 % tip polarization is obtained.) $A_{(dI/dV)/T}$'s larger than 10 % were never observed which makes it likely that the magnetization directions are indeed parallel. Using this tip polarization, the black solid line in Fig. 41(d) is obtained from the calculated spin-dependent sample total-states, which also shows a good agreement with the experimental curves (A 15 % tip polarization was used. Details are discussed in the next section). The band structure calculation showed two surface states at 0.27 V and 0.50 V, and one surface resonance at 0.87 V above the Fermi energy. The decay factor is different for the surface states and the surface resonance, i.e. these states have different tunneling probabilities (T's). The $A_{(dI/dV)/T}$ uses the average of these T's. However, the $A_{(dI/dV)/T}$ shows the same values as the calculated curve between the Fermi energy and +1 V. In this case the influence of the different decay factors is not detected.

Figure 41(e) shows three $A_{(dI/dV)/T}$ curves obtained from the $(dI/dV)/T$ curves in Figs. 41(a-c), i.e. $(dI/dV)/T$ curves obtained at the negative and positive voltage set points as well as curves obtained by different Fe-coated W tips were used. The three $A_{(dI/dV)/T}$ curves in Fig. 41(e) are similar at positive voltages (+10 %). These show that: (1) The exponential background is completely removed. (2) $A_{(dI/dV)/T}$ above the Fermi energy is independent of set points. (3) Reproducible $A_{(dI/dV)/T}$ values are observed with different Fe-coated tips at the positive voltage side (Fig. 41(d)). Scattering of $A_{(dI/dV)/T}$ at the negative voltage side may be a contribution of the tip DOS [6].

It was found that, on the Mn(001) surface, $P_{tip}(E_F) \cdot P_{Mn}(V)$ is 0.1. By following the discussion around Eqs. 21 and 22, using this $P_{tip}(E_F) \cdot P_{Mn}(V) = 0.1$, we can calculate the dI/dV at +0.5 V measured at the negative ($V_S = -0.5$ V) and positive ($V_S = +0.5$ V) voltage set points as follows:

$$dI/dV(+0.5V) = dI/dV_o(1 + P_S(+0.5V)P_T(E_F))\exp(2\kappa\Delta z(V_{setpoint} = -0.5V)), \quad (35)$$

$$dI/dV(+0.5V) = dI/dV_o(1 + P_S(+0.5V)P_T(E_F))\exp(-2\kappa\Delta z(V_{setpoint} = +0.5V)), \quad (36)$$

where $P_S(+0.5V)P_T(E_F) = (dI/dV)/T(+0.5V) = 0.1$. Since the polarity of $P_SP_T = (dI/dV)/T$ changes below and above the Fermi energy, the polarity of the Δz changes dependent on the set point voltage. $\Delta z = 0.1$ Å is used. Then, in Eq.35, $(1 + P_S(+0.5V)P_T(E_F))\exp(2\kappa\Delta z(V_{setpoint} = -0.5V)) = 1.1\exp(0.1) \approx 1.2$. In the same way, in Eq.36, $(1 + P_S(+0.5V)P_T(E_F))\exp(-2\kappa\Delta z(V_{setpoint} = -0.5V)) = 1.1\exp(-0.1) \approx 1.0$.

---

[16] Figures 41(a)-(c) are $(dI/dV)/T$ curves showing the maximum magnetic contrast.

Thus, $dI/dV(+0.5V)$ obtained at the positive voltage set point is the same as dI/dV_o (non-spin-polarized dI/dV term), whereas $dI/dV(+0.5V)$ obtained at the negative voltage set point shows a magnetic contrast of 20 %. This is in good agreement with the experimentally obtained $A_{dI/dV}$ (see Fig. 39(c)).

To obtain $A_{(dI/dV)/T}$ usually it needs a measurement of a spectroscopy curve up to a higher voltage (>2 V). This causes a higher possibility to include spike-like noise. In fact, the $A_{(dI/dV)/T}$ curves are more noisy than $A_{I(V)}$, $A_{dI/dV}$, and $A_{(dI/dV)/(I/V)}$ curves. If it is not necessary to obtain the quantitative information, i.e. only qualitative information, $A_{I(V)}$, $A_{dI/dV}$ or $A_{(dI/dV)/(I/V)}$ will be sufficient.

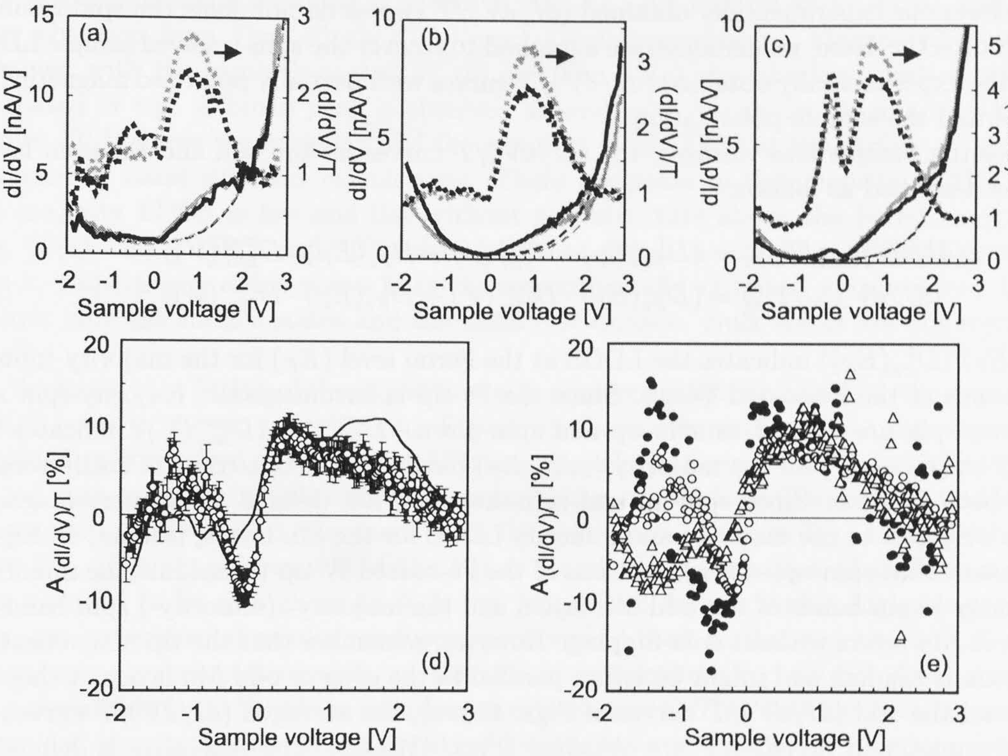

FIG. 41. (a)(b)(c): dI/dV curves (solid curves, averaged over 30 single curves) normalized by voltage-dependent tunneling probability functions (T) were obtained with Fe-coated W tips on Mn films thicker than three layers. Solid and dotted curves are the dI/dV and the $(dI/dV)/T$ curves, respectively. Black and grey curves are representative of the odd and the even layers, respectively. T (dashed curves) were obtained by a fit to the background of the dI/dV curves. $(dI/dV)/T$ curves are shown as dotted curves. (a) and (b) were obtained by the same Fe-coated W tip. (c) was obtained by a different Fe-coated W tip. (a) and (c) were obtained at a negative voltage set point ($V_S = -0.5$ V, $I = 0.5$ nA). (b) was obtained at a positive voltage set point ($V_S = +0.5$ V, $I = 0.5$ nA). (d) gives the asymmetry of the $(dI/dV)/T$ curves obtained on the even and the odd Mn layers as a function of the sample bias voltage. The black solid curve is obtained from the calculated spin-resolved DOS. (e) Black dots, triangles, and white dots were obtained from (a), (b), and (c), respectively.

E. Experimentally obtained sample surface spin-resolved LDOS and polarization

Although the spin-resolved sample LDOS can be obtained by spin-polarized (inverse) photoelectron spectroscopy, the space resolution of this technique is limited by the electron beam diameter, e.g. with SPLEEM, ~10 nm magnetic resolution was confirmed [9]. On the contrary, the use of SP-STS can recover the spin-resolved sample DOS at a subnanometer scale (~0.4 nm). This resolution was confirmed in the current range between 0.1 nA and 20 nA. If the tip has a polarization of 100 %, the tip can detect only spin-up or spin-down DOS, i.e., the normalized $(dI/dV)/T$ curves directly show the spin-resolved LDOS (see Eq. 27). However, we could not make such a highly spin-polarized tip. Therefore, our experimentally obtained $(dI/dV)/T$ curves do not show the spin-resolved LDOS directly. Here, we demonstrate a method to recover the spin-resolved sample LDOS from the experimentally obtained $(dI/dV)/T$ curves with partially polarized magnetic tips and obtain the sample polarization.

For positive sample bias voltages, the $(dI/dV)/T$ curves for the odd and the even layers can be described as follows:

$$\begin{aligned}(dI/dV)_{even}/T_{even} &= (D^{\uparrow}_{Fe}(E_F)\cdot D^{min}_{Mn}(V) + D^{\downarrow}_{Fe}(E_F)\cdot D^{maj}_{Mn}(V))\\ (dI/dV)_{odd}/T_{odd} &= (D^{\uparrow}_{Fe}(E_F)\cdot D^{maj}_{Mn}(V) + D^{\downarrow}_{Fe}(E_F)\cdot D^{min}_{Mn}(V))\ .\end{aligned} \tag{37}$$

$D^{\uparrow}_{Fe}(E_F)$ ($D^{\downarrow}_{Fe}(E_F)$) indicates the LDOS at the Fermi level (E_F) for the majority (minority) bands of the Fe-coated W tip. Since the Fe tip is ferromagnetic, majority-spin and minority-spin are defined as spin-up and spin-down. $D^{maj}_{Mn}(V)$ ($D^{min}_{Mn}(V)$) indicates the LDOS at ($E_F + eV$) for the majority (minority) bands of the sublattices of antiferromagnetic bct Mn films. Since spin-up and spin-down are not defined for antiferromagnetic slabs, we prefer to use majority and minority LDOS for the Mn layers, instead. In Eq. 37 we assume that spin-up(-down) electrons of the Fe-coated W tip tunnel into the minority-(majority-) spin bands of the odd Mn layers and the majority- (minority-) spin bands of the even Mn layers without spin-flipping. However, remember that the tip magnetization direction is random and might be either parallel to the even or odd Mn layers. Using the even and the odd $(dI/dV)/T$ curves of Figs. 41(a-c), the averaged $(dI/dV)/T$ curve and the asymmetry in $(dI/dV)/T$ are obtained (Figs. 41(d,e)). The $A_{(dI/dV)/T}$ is defined as follows:

$$\begin{aligned}A_{(dI/dV)/T} &= \frac{(dI/dV)_{even}/T_{even} - (dI/dV)_{odd}/T_{odd}}{(dI/dV)_{even}/T_{even} + (dI/dV)_{odd}/T_{odd}}\\ &= \frac{D^{\uparrow}_{Fe} - D^{\downarrow}_{Fe}}{D^{\uparrow}_{Fe} + D^{\downarrow}_{Fe}}\cdot\frac{D^{min}_{Mn} - D^{maj}_{Mn}}{D^{min}_{Mn} + D^{maj}_{Mn}}\\ &= P_T(E_F)\cdot P_S(E_F + eV),\quad \text{where } V > 0.\end{aligned} \tag{38}$$

$(dI/dV)_{even}/T_{even}$ and $(dI/dV)_{odd}/T_{odd}$ are $(dI/dV)/T$ curves obtained on the even and the odd layers, respectively, $P_T(E_F)$ the tip polarization at E_F, $P_S(E_F + eV)$ the sample polarization at $(E_F + eV)$. $A_{(dI/dV)/T}$ shows a maximum value of about 10 % around the peak energy and reaches 0 % above +2 V (Figs. 41(d,e)). Using Eqs. 37 and 38 the spin-resolved LDOS of Mn(001) can be experimentally obtained as follows:

$$D_{Mn}^{maj} = \frac{1}{c}(1 - \frac{A_{(dI/dV)/T}}{P_T})[(dI/dV)/T]_{ave}$$
$$D_{Mn}^{min} = \frac{1}{c}(1 + \frac{A_{(dI/dV)/T}}{P_T})[(dI/dV)/T]_{ave}, \tag{39}$$

where $[(dI/dV)/T]_{ave}$ is the average of $(dI/dV)_{odd}/T_{odd}$ and $(dI/dV)_{even}/T_{even}$. c is the sum of $D_{Fe}^{\uparrow}$ and $D_{Fe}^{\downarrow}$. Then we realized that the tip polarization is the most important factor to recover the sample spin-resolved LDOS. From a comparison with the band structure calculations, we tried to find the tip polarization of our partially polarized tip.

By following Eq. 39, the majority (grey) and the minority (black) LDOS of Mn(001) can be experimentally obtained as shown in Fig. 42(a-c). Figures 42(a), 42(b), and 42(c) were obtained from Figs. 41(a), 41(b), and 41(c), respectively. Figures 42(a,b) were obtained with the same Fe-coated W tip and Fig. 42(c) was obtained with a different Fe-coated W tip. A broad peak is observed around +0.8 V only in the minority LDOS. Figure 42(d) shows the majority and the minority local LDOS at the surface of Mn(001) obtained by band structure calculations. There are peaks in the minority LDOS, while the majority LDOS is low and flat without any structure above the Fermi energy. In Fig. 42(c), "SS", "SR", and "B" refer to surface states, a surface resonance, and bulk states, respectively. This shows that the experimentally obtained spin-resolved LDOS recover only the surface states and the surface resonance. Bulk states are not recovered at all.

We found that fitting of the experimentally observed majority LDOS to the calculated LDOS leads to the tip polarization. Figure 43 shows the results of the experimentally obtained spin-resolved LDOS from different tip polarizations. The experimentally obtained spin-resolved LDOS with a tip polarization of 18±5 % (Figs. 43(b) and 43(c)) show qualitatively a good agreement with the calculated LDOS in Fig. 42(d). Although, from Fig. 43, a tip polarization of 18±5 % is found, the polarization of an Fe-coated tip was assumed to be as high as 44 % in ref. [8]. When we use such a high tip polarization, our experimental results produce a pronounced peak in the majority LDOS which is qualitatively inconsistent with our theoretical calculation (Fig. 43(d)). Also, this high tip polarization (~40 %) likely includes uncertainties: (1) This high tip polarization was concluded from tunneling measurements of Fe/Al_2O_3/super-conductor junctions [10], but the barrier materials greatly influence the measured spin polarization [11]. (2) The spin polarization of Cr(001) was deduced to be 17 % by assuming about 40 % polarization for the Fe-coated tip [8] whereas Cr(001) has highly spin-polarized *d* surface states [12]. (See also appendix.)

Therefore, experimentally the Mn(001) surface polarization: $P_{Mn} = A_{(dI/dV)/T}/P_{tip}(E_F)$ at +0.8 V is obtained 10%/(18±5%) = 60±16 %.

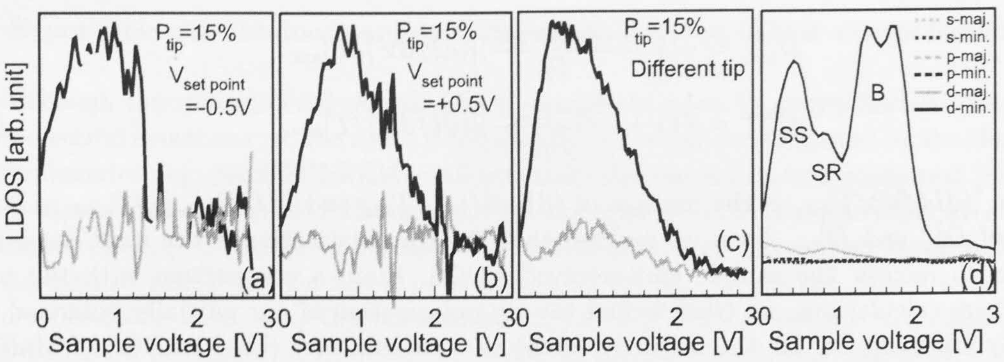

FIG. 42. (a-c) shows the majority (grey) and minority (black) LDOS of Mn(001) obtained from experimentally obtained $(dI/dV)/T$ curves in Fig. 41(a-c). (d) shows the majority (grey) and minority (black) LDOS of Mn(001) obtained by band structure calculations. "SS", "SR", and "B" denote surface states, a surface resonance, and bulk states, respectively.

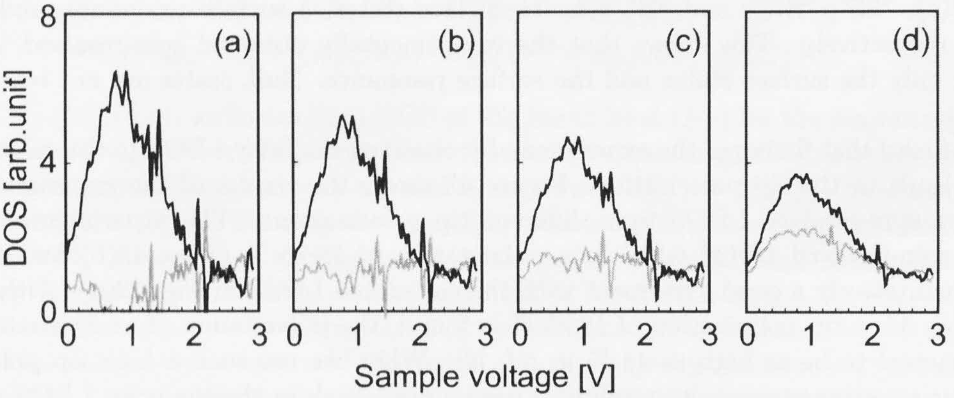

FIG. 43. The majority (grey) and minority (black) LDOS of Mn(001) obtained by experimentally obtained $(dI/dV)/T$ curves are shown. (a), (b), (c), and (d) are obtained with a tip polarization at the Fermi level of 10 %, 15 %, 20 % and 44 %, respectively.

F. Conclusion

We investigated some methods to obtain quantitative information (sample polarization) from SP-STS.

Although asymmetries in $I(V)$ and dI/dV showed a maximum value of 20 %, these strongly depend on the voltage set point and cannot be easily interpreted. Although the asymmetry in $(dI/dV)/(I/V)$ can remove the voltage set point dependence, the exponential background in dI/dV cannot be excluded and $(dI/dV)/(I/V)$ is 1 by definition at the Fermi energy. Thus, the use of $(dI/dV)/(I/V)$ to obtain the sample polarization is complicated. The asymmetry in $(dI/dV)/T$ did not show a dependence on the voltage set point and excludes completely the exponential background in dI/dV. The asymmetry in $(dI/dV)/T$ directly shows the sample polarization ($P_S(V)$) multiplied by the tip polarization at the Fermi energy ($P_T(E_F)$) for $V > 0$, and $P_S(E_F)P_T(V)$ for $V < 0$. The use of $(dI/dV)/T$ is considered to be the most reliable method to obtain quantitative information (sample polarization).

We also demonstrated how to obtain the spin-resolved LDOS from the experimentally obtained $(dI/dV)/T$ curves with partially polarized magnetic tips. We found that the tip polarization plays a major role in obtaining the spin-resolved LDOS. By fitting to the calculated LDOS we estimated a 18±5 % tip polarization.

Therefore, using experimentally obtained $(dI/dV)/T$, $A_{(dI/dV)/T}$, and spin-resolved LDOS, we obtained a 60±16 % polarization on the Mn(001) surface.

REFERENCES

[1] S.N. Okuno, T. Kishi, and K. Tanaka, Phys. Rev. Lett. **88** (2002) 066803.

[2] R. Wiesendanger, M. Bode, and M. Getalaff, Appl. Phys. Lett. **75** (1999) 124.

[3] H. F. Ding, W. Wulfhekel, J. Henk, P. Bruno, and J. Kirschner Phys. Rev. Lett. **90**, 116603 (2003)

[4] U. Schlickum, W. Wulfhekel, J. Kirschner, Appl. Phys. Lett. **83** (2003) 2016, as well as private communication with W. Wulfhekel in July 2003.

[5] S.F. Alvarado, Phys. Rev. Lett. **75** (1995) 513.

[6] V.A. Ukraintsev, Phys. Rev. B **53** (1996) 11176.

[7] M.M.J. Bischoff, T.K. Yamada, C.M. Fang, R.A. de Groot, and H. van Kempen, Phys. Rev. B **67** (2003) 045422.

[8] M. Kleiber, M. Bode, R. Ravlić, and R. Wiesendanger, Phys. Rev. Lett. **85** (2000) 4606.

[9] R. Ramchal, A. Schmid, M. Farle, and H. Poppa, abstract, the 18th International Colloquium on Magnetic Films and Surfaces, 2003.

[10] P.M. Tedrow and R. Meservey, Phys. Rev. B **7** (1973) 318.

[11] Private communication with R.A. de Groot.

[12] J.A. Stroscio, D.T. Pierce, A. Davies, R.J. Celotta, and M. Weinert: Phys. Rev. Lett. **75** (1995) 2960.

VIII. SEMPA MEASUREMENTS FOR THE FE-COATED W TIP

As discussed in the previous section, obviously, it is important to know the tip polarization quantitatively to get the sample polarization from experimentally obtained SP-STS results. To find the tip polarization other techniques are needed such as spin-resolved photoemission spectroscopy (SP-PES) or scanning electron microscopy with polarization analyzer (SEMPA). Here, SEMPA was chosen since SEMPA can directly resolve the tip apex visually [1,2]. During SEMPA measurements the polarization analyzer (here I used a home-made Mott detector) detects polarization of the secondary electrons (<50 eV) which are generated by a SEM primary beam. These electrons include information of the near sample surface. Usually the polarization of the secondaries reflects the polarization of the sample below the Fermi energy.

A. Experimental

SEMPA measurements were performed in UHV ($\sim 2 \times 10^{-10}$ mbar) at RT with a homemade compact Mott detector with an acceleration voltage of 15 kV [3]. Typically, much higher acceleration voltages (e.g. 50-100 kV) are used for Mott detectors [1,2,4]. Then, the size of the detector becomes bigger. By using a 15 kV acceleration voltage, we made a compact Mott detector. In the Mott detector the electrons are accelerated to 15 kV and scattered by a high-atomic-number target such as Au film (100 nm thickness). This scattering is spin-dependent because of the spin-orbit interaction [5]. The Mott detector was installed into a UHV chamber with a combined Auger - SEM setup (JEOL-JAMP30). Figure 44(a) shows pictures of our SEMPA setup. The primary electron beam is coming from the top ("1") and hits the sample ("2"). The secondary electrons from the sample were detected by a Mott detector ("3"). Figure 44(b) shows the sample holder inside the UHV chamber, where spaces between the sample holder ("7"), the SEM beam gun ("5"), and the Mott detector ("6") are within 1 cm. The unpolarized primary electron beam voltage of 5 kV was used since, in our setup, the obtained polarization saturates at the primary beam voltage higher than 1 kV, while the yield of the secondary electrons has the maximum at the primary beam voltage at 0.65 kV. Although a typical beam current of 1 nA was used for SEM measurements, the current was increased to 1 μA during SEMPA measurements to increase the number of the secondary electrons. The distance between the top of the Mott detector and the specimen was about 1 cm. The Sherman function (S) and the figure of merit (Q) amounted to 0.11 and $\sim 2 \times 10^{-6}$, respectively [3]. The Sherman function determines the relation between measured asymmetry and the degree of polarization of the electrons. To obtain the Sherman function of our setup we used a known spin-polarized electron beam from (Cs, O)/p-GaAs(001). Then, we obtained $S = 0.11 \pm 0.01$ for 0-100 eV electrons. The figure of merit is defined as $Q = S^2 \cdot I/I_o$, where I_o denotes the current from the electrons coming to the Au target inside the Mott detector and I denotes the current detected by the four channeltrons (see Fig. 45).

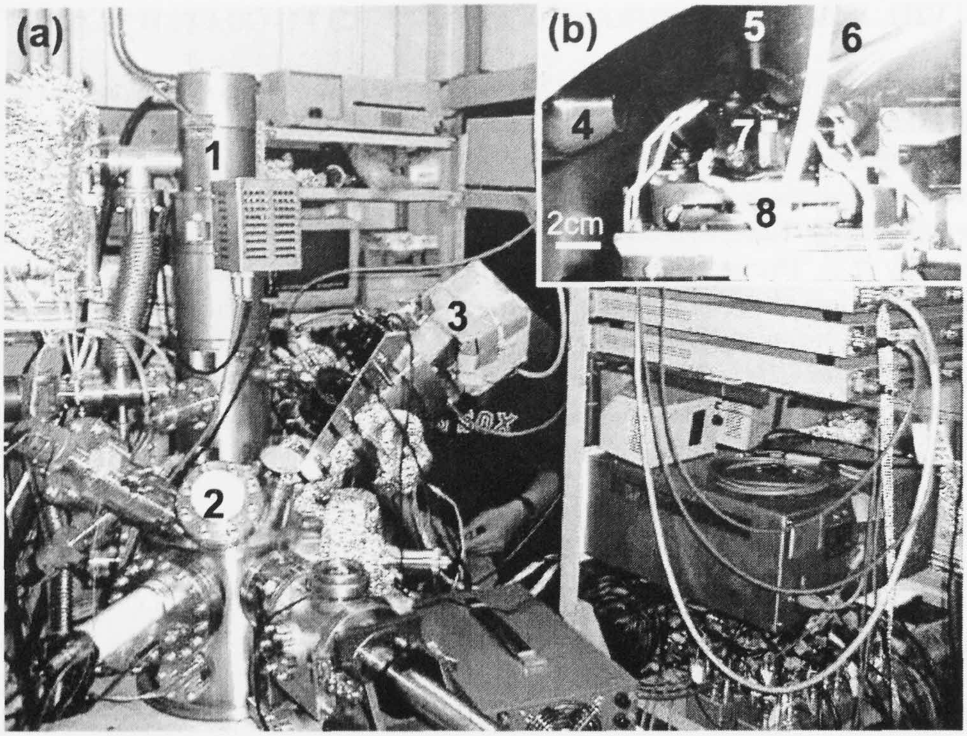

FIG. 44. (a) Our UHV-SEMPA setup: 1. the SEM primary electron beam gun, 2. the UHV chamber equipped with an Ar^+ sputter gun, an Auger analyzer, an evaporator, and a transfer-rod, 3. the home-made Mott detector. (b) The setup inside the UHV chamber: 4. the Auger analyzer, 5. the SEM electron beam gun, 6. the Mott detector, 7. the sample holder, and 8. the sample stage, which can move the sample holder along the x, y, and z axis.

Secondary electrons scattered at the sample surface were accelerated to a Au target in the Mott detector by electrostatic lenses as shown in Fig. 45. The electrons scattered at the Au target were counted by four channeltrons located along the x-axis and y-axis shown in Fig. 45. The asymmetry in the detected channeltron currents reflects the polarization along the directions of the two channeltrons.

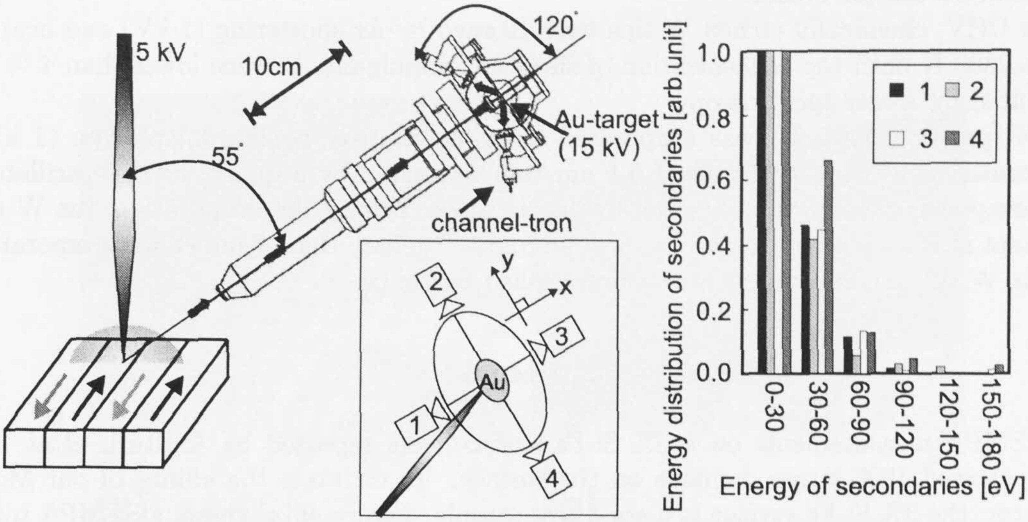

FIG. 45. A sketch of our home-made Mott detector.

Figure 45 shows the energy distribution of the detected secondary electrons. Since channeltrons ("1"-"4") detect mainly electrons within an energy range of 0-60 eV [6], the total polarization of these low energy secondary electrons was measured. Such low energy secondary electrons are surface sensitive and have an information depth of 0.4-0.5 nm [7]. The sample polarization was obtained as follows:

$$\begin{aligned} P_x &= \frac{1}{S} \cdot \frac{N_3 - N_1}{N_3 + N_1} \\ P_y &= \frac{1}{S} \cdot \frac{N_4 - N_2}{N_4 + N_2} \end{aligned} \qquad (40)$$

where P_x and P_y denote sample polarization along x-axis and y-axis, respectively. N_1, N_2, N_3, and N_4 denote numbers of electrons detected by each channeltron sketched in Fig 45. The scan area was selected by SEM before SEMPA measurements. At the selected area, the secondary electrons were typically counted at 60×60 pixels. The typical acquisition time of one SEMPA image was 30 minutes, i.e. 0.5 sec/pixel. Each pixel of the SEMPA image is composed of counts detected at a rate of 30,000-200,000 counts/second, which statistic error is given by $\sqrt{N}/N$=0.2-0.6 %. In order to obtain the polarization with a smaller statistic error, more than ten million counts were obtained at some positions by fixing the primary beam (spot-mode measurement). Then, the statistic error decreases to 0.03 %. (The diameter of the primary beam is smaller than 100 nm.) During this measurement the current density is more than 10^9 electrons/(nm^2·second).

Auger electron spectroscopy (AES) measurements were performed as follows; (i) An SEM image was obtained. (ii) The primary beam was moved to the particular position of the image within an accuracy of the beam instability. (iii) An Auger spectrum at the beam position was measured.

All SEMPA and AES measurements were performed for only one side of the tip. The

the SEM Ta sample holder.

In UHV, chemically etched W tips were cleaned by Ar sputtering (1 kV) and heated up to 2300 K until the concentration of surface contaminants became lower than 4 % as measured by Auger spectroscopy.

Fe (purity 99.995 %) was evaporated from an electron bombardment-type (1 kV) evaporator at a deposition rate of 0.1 nm/min estimated by a quartz crystal oscillator. The evaporation beam was directed to the tip apex. During the evaporation, the W tip was kept at RT and the pressure was around 5×10^{-10} mbar. Here, 7 nm Fe was evaporated on the W tip. An external field was not applied to the tip.

B. Results

SEMPA measurements on a 3% Si-Fe surface were reported by Anilturk *et al.* [8]. They showed 180° stripe domains on the surface. To estimate the ability of our Mott detector, the 3% Si-Fe surface is a good test sample. Figure 46(a) shows a SEMPA total count image, which reveals topographic information, obtained on the 3 % Si-Fe(001) single crystal surface (magnetic easy axis is <100>). This surface was chemically etched to remove the oxide layers and then cleaned in UHV by Ar^+ sputtering and annealing up to 1070 K (10 min.). Figure 46(b) shows a SEMPA (P_x) image, in which magnetic contrast is observed. Both images were obtained simultaneously by our homemade Mott detector. The total count image shows a flat surface. The SEMPA (P_x) image in Fig. 46(b) shows supplementary magnetic domains [9]. The contrast (bright-dark) corresponds to a polarization of 13.5 % which is in agreement with previous results [8] (Here, the polarization slightly varies at different places by ±0.5 % due to the influence of the roughness on the sample surface as is shown in Fig. 46(a).).

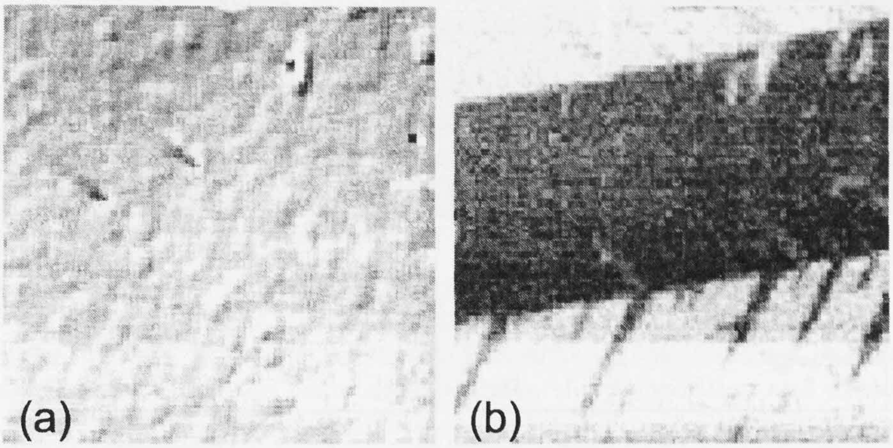

FIG. 46. SEMPA images obtained on a 3% Si-Fe(001) single crystal. The scan size is 300×300 μm^2. (a) and (b) were simultaneously obtained. Both images consist of 60×60 pixels. The total intensity image (a) shows a flat surface. (b) shows the magnitude of the in-plane x-component polarization. Magnetic domains can be recognized. The contrast in (b) corresponds to a polarization of 13.5 ± 0.5 %.

The highest magnetic resolution which was ever achieved in SEMPA is 5 nm (Kohashi and Koike [10]). However, the resolution of our SEMPA setup could not achieve this scale. The reasons are instability of the SEM electron beam and vibration of the sample, which both limit the resolution of our SEM [17] . A typical magnetic resolution of our SEMPA can be estimated from the averaged line profile of the SEMPA images obtained on a magnetic domain wall. Magnetic contrasts varied within 3.3 μm for the x-axis and 1.6 μm for the y-axis (see Fig. 47). The resolution could be highly improved by using more stable electronics and using a more stable sample stage.

---

[17] There are several kinds of the SEM electron beam sources [11]: (1) a W-wire thermal emitter, (2) a W-wire thermal emitter + LaB_6 to lower the work function, (3) W-tip field emission, and (4) W+ZrO_2-tip field emission and thermal emitter ($\sim$1 μm radius). ZrO_2 lowers the work function as well as prevents oxidization (so called Schottky emission). Therefore, the tip can have larger radius and is consequently more stable in performance. The use of the W-tip increases the resolution. Our setup uses the second one.

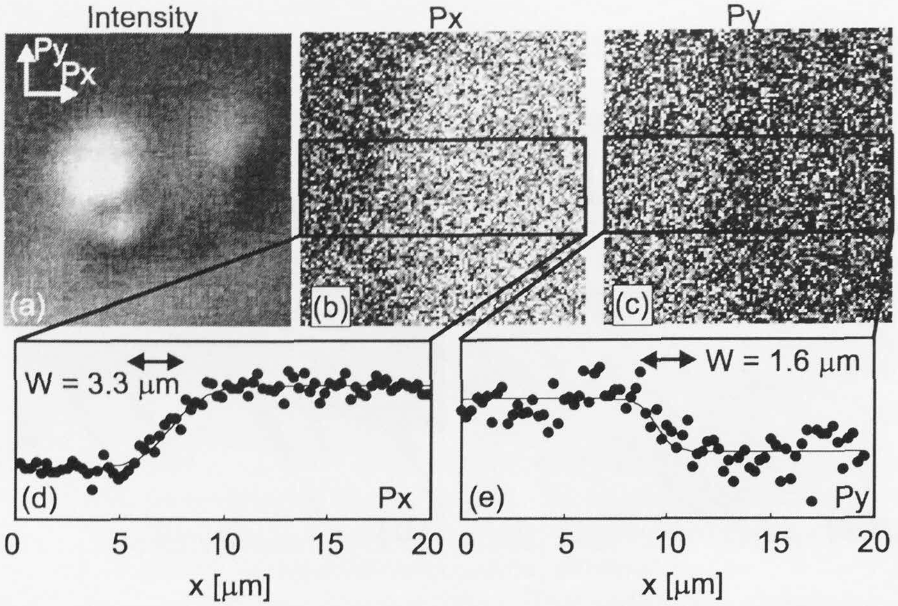

FIG. 47. SEMPA measurements obtained on the 3 % Si-Fe(001) single crystal surface. (a) shows an intensity image, which size is 20×20 μ^2. (b),(c) show SEMPA images obtained at the same area as (a). A magnetic domain wall is running from bottom to top. (b) and (c) show the x- and the y-axis component of the magnetization, respectively. (d) and (e) show averaged line profiles obtained from the boxed areas in (b) and (c), respectively. Obtained line profiles were fitted to $a \cdot \tanh \frac{x-x_o}{w/2}$, where w was defined as a magnetic domain wall width. x_o denotes the center of the domain wall and a and b are fitting parameters. The domain walls in (d) and (e) are 3.3 μm and 1.6 μm wide, respectively.

Figure 48(a) shows a SEM image obtained on the tip apex. At the boxed area in Fig. 48(a), SEMPA measurements were performed. Figures 48(b), 48(d), and 48(e) were obtained on a W tip while Figs. 48(c), 48(f), and 48(g) were obtained on an Fe-coated W tip. First, SEMPA measurements on the W tip were performed. Second, without any movements of the tip, a 7 nm Fe film was deposited at room temperature on the W tip from the tip-apex direction. Third, SEMPA measurements on the Fe-coated W tip were performed. Figures 48(b) and 48(c), which are intensity images, were performed at the same area before and after Fe deposition. In the intensity image, the grey scale ranges between 100,000 (bright) and 15,000 (dark) counts.

Figures 48(d) and 48(f) are P_x images. Figures 48(e) and 48(g) are P_y images. The polarization image obtained from the Fe-coated W tip includes two components: polarization caused by the Fe films on the W tip and polarization caused by the shape of the tip. Different angles of the tip surface cause different trajectories of the secondary electrons from each sample position to the Au target and, consequently, the W tip also shows polarization. In order to obtain the polarization of the Fe-coated W tip, the influence by the shape must be removed by subtracting the W tip asymmetry from the Fe-coated tip asymmetry.

Figures 48(h) shows the distribution of the polarization direction obtained from $\theta = \tan^{-1}(\mathrm{P_y}/\mathrm{P_x})$. The upper and bottom parts of the tip are brighter ($\sim 35^\circ$) and darker ($\sim 90^\circ$), respectively, in Fig. 48(h), which indicates variation of the magnetization directions of the Fe film on the W tip. These images show no magnetic domains with a size larger than 1 μm.

Spot-mode measurements, which lead to more than ten million counts, were performed at the positions marked "A", "B", "C", and "D" in Fig. 48(b) before and after the Fe evaporation to get the tip polarization precisely. The polarization of the Fe-coated W tip was obtained by subtracting $[P_x]_W$ and $[P_y]_W$ from $[P_x]_{Fe}$ and $[P_y]_{Fe}$, respectively. The absolute value of the polarization ($|\vec{P}|$) was obtained from $\sqrt{(P_x)^2 + (P_y)^2}$. Figure 48(i) shows $|\vec{P}|$ at the four positions marked in Fig. 48(a). Each data has a statistic error below 0.45 % [18] . $|\vec{P}|$ is 20±5 % at all positions in spite of the fact that the conditions of the substrate are different at various positions. The error ±5 % is caused by instability of the primary beam. When the beam slightly shifts, the polarization also changes due to different geometry at the different position on the tip. This error is much bigger than the statistical error.

---

[18] The statistic error in $|\vec{P}|$ was obtained as follows. Each counted number included the error of $\sqrt{N}$. The error in the asymmetry of the numbers ($A_{ij} = (N_i - N_j)/(N_i + N_j)$) can be described as $\Delta A_{ij}^W = \sqrt{(\frac{\partial A_{ij}^W}{\partial N_i}\sqrt{N_i})^2 + (\frac{\partial A_{ij}^W}{\partial N_j}\sqrt{N_j})^2}$ as well as $\Delta A_{ij}^{Fe} = \sqrt{(\frac{\partial A_{ij}^{Fe}}{\partial N_i}\sqrt{N_i})^2 + (\frac{\partial A_{ij}^{Fe}}{\partial N_j}\sqrt{N_j})^2}$. Then, to obtain the polarization of the tip, I subtracted P_W from P_{Fe} (c.f. $P = A/S$). $P_{ij} = P_{ij}^{Fe} - P_{ij}^W$. The error of P_{ij} can be described as $\Delta P_{ij} = \sqrt{(\frac{\partial P_{ij}}{\partial P_{ij}^{Fe}}\Delta A_{ij}^{Fe})^2 + (\frac{\partial P_{ij}}{\partial P_{ij}^W}\Delta A_{ij}^W)^2} = \sqrt{(\Delta A_{ij}^{Fe})^2 + (\Delta A_{ij}^W)^2}$.

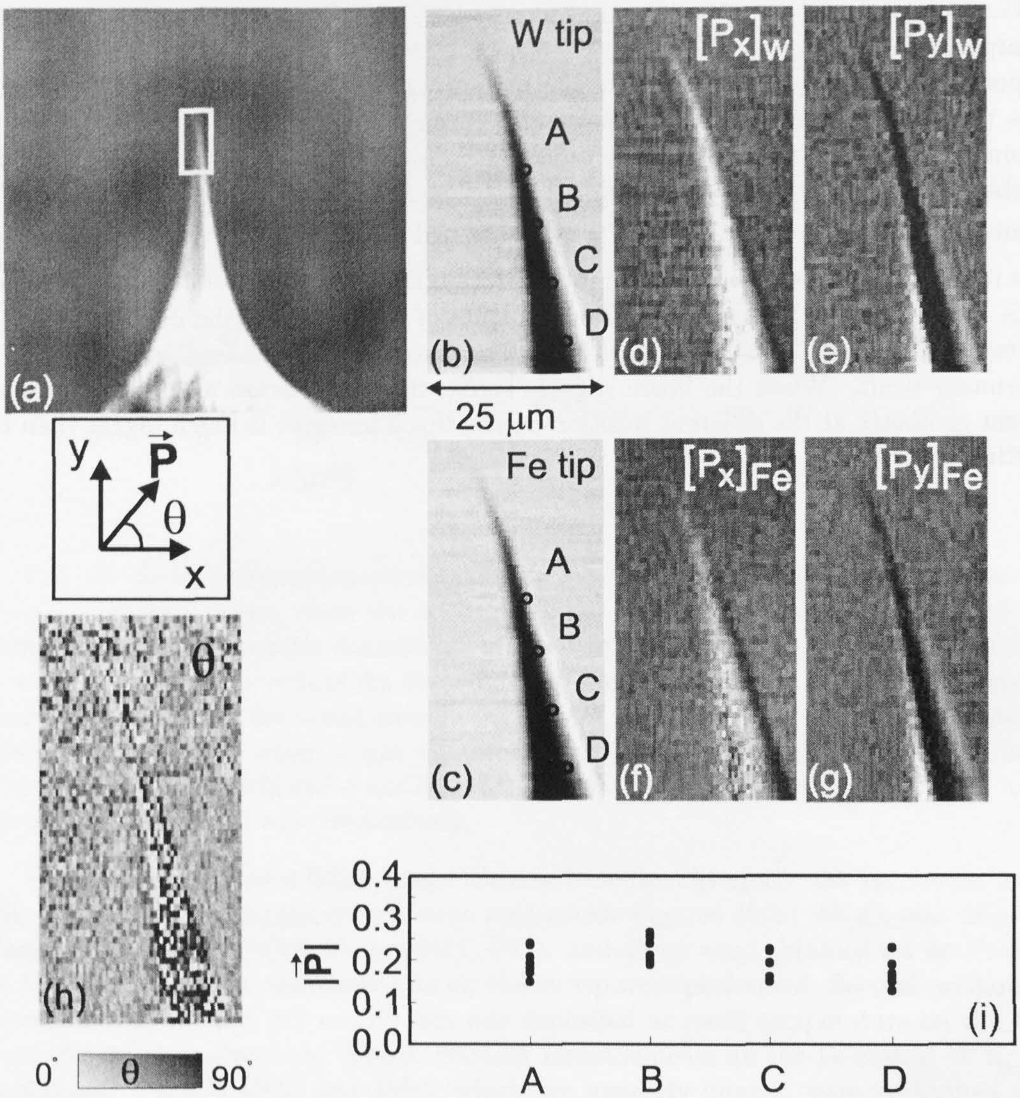

FIG. 48. (a) shows a SEM image obtained on the tip apex (333×333 μm^2, 0.65 nm/pixel.). (b) and (c) show intensity images (25×50 μm^2: 60×60 pixels) of the same W tip before and after deposition of Fe, respectively. (d) and (e) show P_x and P_y images, respectively, obtained on the W tip. (f) and (g) show P_x and P_y images, respectively, obtained on the W tip covered by Fe. (h) shows the magnetization direction of the Fe-coated W tip, which was obtained from $\theta = \tan^{-1}(P_y/P_x)$, where P_x was obtained by subtracting Fig. 48(d) from Fig. 48(f) and P_y was obtained by subtracting Fig. 48(e) from Fig. 48(g). In (h), the grey scale corresponds to the angle θ. (i) shows the absolute values of the polarization obtained at positions "A-D". At each position more than five measurements were repeated. The obtained data scatters around 20 %.

Figures 49(a) and 49(b) show Auger spectra obtained at the positions "A" on the W tip (Fig. 48(a)) and the Fe-coated W tip (Fig. 48(b)), respectively. After the cleaning process, the oxygen peak is still visible. My cleaning process cannot remove the contaminants from the W tip completely. After ~7 nm Fe evaporation, the W peaks disappeared (Fig. 49(b)). Figure 49(c) shows Auger peak-to-peak height ratios for W(1738eV)/Fe(703eV) and O(512eV)/Fe(703eV) as a function of distance from the tip apex. At the positions "A" and "B" in Fig. 48(b), the W peak (1738eV) was not observed, but the W peak was observed at about 30 μm from the tip apex (filled circles in Fig. 49(c)). The Fe coverage seems to decrease away from the tip apex.

An oxygen peak was observed at all positions (empty circles in Fig. 49(c)). Already after Fe deposition the ratio O/Fe is about 0.1-0.4. From literature it is known that when 5 L of oxygen is dosed on the Fe surface at room temperature, Auger spectra show the ratio O/Fe = 0.3. Then, the Fe surface is covered by 1/2 ML of oxygen (below 3 L, oxygen is dissociatively chemisorbed while above the 3 L oxygen is incorporated in the selvedge) [12,13]. This indicates that at least half of the surface of the Fe-coated W tip was already covered by oxygen. The oxygen impurity was likely caused by a lot of degassing during the annealing of the tip or the Fe growth. Angle and spin resolving photoelectron spectroscopy measurements showed that the oxygen atoms on Fe(110) films on W(001) form an FeO layer. This FeO layer is antiferromagnetic [14]. Also, spin-polarized metastable deexcitation spectroscopy studies showed that oxidization on Fe(110) does not influence the polarization for dosages below 2 L (1 L = 10^{-6} Torr s), whereas the polarization inverses for dosages larger than 4 L [15].

Thus, the obtained polarization could be different from the polarization of the clean Fe-coated W tip. Also, it might be that the obtained polarization is influenced by the different roughness of the W surface and the Fe films.

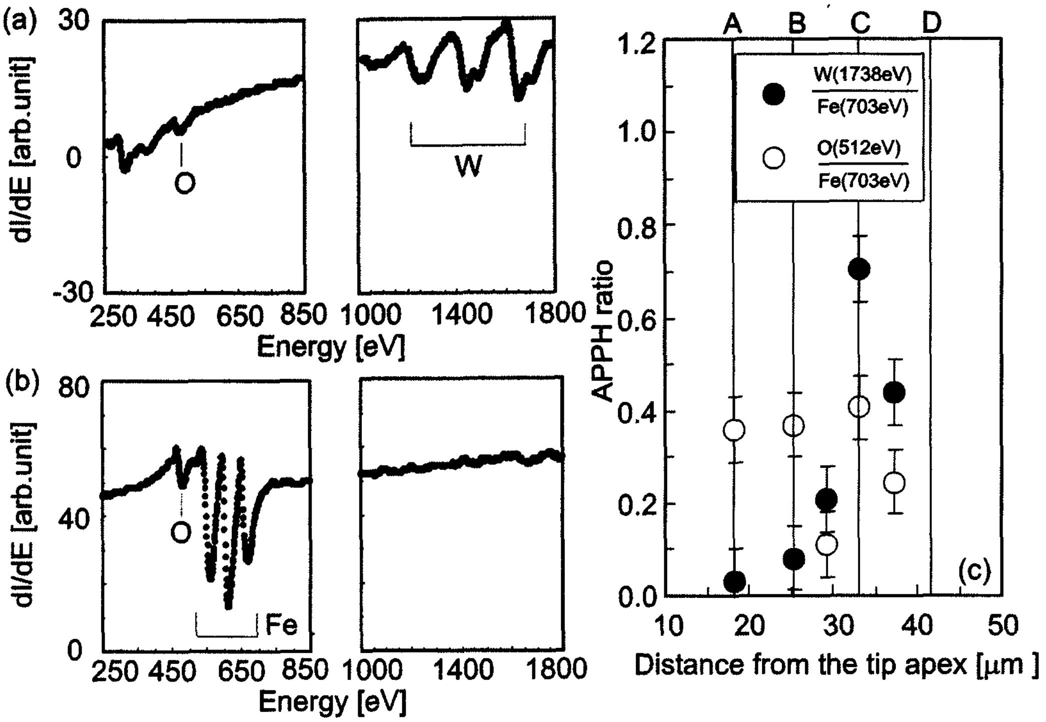

FIG. 49. (a) and (b) show differential Auger intensity curves as a function of the energy. (a) was obtained at the position "A" in Fig. 48(b) after the cleaning process. (b) was obtained at the position "A" in Fig. 48(c) (Fe-coated W tip). (c) shows Auger peak-to-peak height ratio as a function of distance from the tip apex. Filled and empty circles denote W(1738eV)/Fe(703eV) and O(512eV)/Fe(703eV), respectively, which were obtained on the Fe-coated W tip at positions "A"-"D".

C. Discussions

Measurements of the polarization of secondary electrons is useful for studying the surface polarization [3,16–25]. There are typically two kinds of secondary electrons which are generated by either optical pumping (elastic scattering) or high-energy electrons (inelastic scattering). For both cases, the polarization of secondary electrons with low kinetic energies is enhanced. Koike *et al.* showed the dependence of the primary electron beam energy on the secondaries polarization for Fe(110) and claimed that the spin asymmetry of the inelastic mean free path ($A_\lambda(V)$) plays a major role, i.e., the polarization of low-energy electrons is strongly enhanced by $A_\lambda(V)$ [25]. Since our Mott detector mainly detects electrons in the range of 5-50 eV, the total polarization obtained by our Mott detector seems to be about 5 % enhanced by $A_\lambda(V)$ [24], while other results showed that only electrons below 4 eV are enhanced [22].

It is difficult to estimate the absolute polarization value from the Fe-coated W tip without switching the tip magnetization. My obtained polarization value without the influence of the tip shape is about 20±5 %. By substituting the influence of $A_\lambda(V)$, this value decreases to 15±5 %, which value is much less than the 29 % reported for the Fe(110) surface [25].

Another difficulty of the SEMPA measurement of the Fe-coated W tip is that the tip has a curved surface instead of a flat surface. The curvatures on the sample lead to apparent asymmetries. Thus, usually SEMPA measurements were only performed on very flat samples (e.g. [26]). Although SEMPA studies on a curved surface was reported for a magnetic-force-microscopy Fe tip, no clear information was obtained due to the high geometry-induced asymmetry [4]. In ref. [2], to exclude this effect, a double sided detector was used. One side was covered by a high atomic-number-material (gold) and the other side was covered by a low atomic-number-material (carbon). The carbon side is not sensitive to spin scattering, but it is sensitive to the geometry-induced scattering asymmetry. By subtracting the asymmetry measured on the carbon detector from the asymmetry measured on the gold detector, the real spin asymmetry can be deduced. In this study, we excluded the geometry-induced scattering asymmetry by subtracting the signal from the pure W tip from the signal from the Fe-coated W tip. However, if the surface roughness varies after the Fe deposition, the Fe/W tip gives more geometry-induced asymmetries.

Variation of the polarization directions on the Fe-coated W tip (Fig. 48(h)) may be caused by different Fe coverages as shown by the Auger spectra (Fig. 49(c)). Since studies of Fe films grown on W(110) at RT showed that the magnetic in-plane easy axis of the Fe films switches from $[1\bar{1}0]$ to [001] above an Fe thickness of ~6.5 nm [16,27–29], the Fe films on the W tip may also show the similar characteristics.

D. Conclusion

The polarization of the Fe-coated W tip (only one-side) was studied by SEMPA and Auger spectroscopy in UHV at RT. The polarization of the Fe-coated W tip near the tip apex was estimated to be 15±5 %. However, care must be taken in the interpretation of this result, since half of the tip surface was covered with oxygen and the geometry of the Fe film might lead to an apparent polarization signal. The tip magnetization direction was observed to vary close to the tip apex, which may be caused by different Fe coverages.

REFERENCES

[1] K. Koike and K. Hayakawa, Jap. J. Appl. Phys. **23** (1984) L187.

[2] M.R. Scheinfein, J. Unguris, M.H. Kelley, D.T. Pierce, and R.J. Celotta, Rev. Sci. Instrum. **61** (1990) 2501.

[3] Y. Oshima, T. Yamada, J. Fujii, and T. Mizoguchi, Trans. Magn. Soc. Japan. **1** (2001) 16.

[4] R. Allenspach, IBM J. Res. Develop. **44** (2000) 553.

[5] J. Kessler, *PolarizedElectrons*, Springer, Berlin, 1985.

[6] Numbers of electrons were counted by applying negative voltages to the entrance of channeltrons (the constant acceleration voltage to the channeltrons).

[7] D.L. Abraham and H. Hopster, Phys. Rev. Lett. **58** (1987) 1352.

[8] O.S. Anilturk and A.R. Koymen, J. Magn. Magn. Mater. **213** (2000) 281.

[9] A. Hubert and R. Schäfer, *Magnetic domains: The analysis of magnetic microstructures*, (Springer Verlag, 1998).

[10] T. Kohashi and K.Koike, Jpn. J. Appl. Phys. **40** (2001) L1264.

[11] Private communication with Dr. M.M.J. Bischoff.

[12] G.W. Simmons and D.J. Dwyer, Surf. Sci. **48** (1975) 373.

[13] Y. Sakisaka, T. Miyano, and M. Onchi, Phys. Rev. B **30** (1984) 6849.

[14] M. Getzlaff, J. Bansmann, and G. Schonhense, J. Magn. Magn. Mater. **192** (1999) 458.

[15] M. Getzlaff, D. Egert, P. Rappolt, M. Wilhelm, H. Steidl, G.Baum, and W. Raith, J. Magn. Magn. Mater. **140-144** (1995) 727.

[16] R. Kurzawa, K.-P. Kämper, W. Schmitt, and G. Güntherodt, Solid. State. Commu. **60** (1986) 777.

[17] M. Getzlaff and G. Schönhense, Surf. Sci. **331-333** (1995) 213.

[18] M. Getzlaff, J. Bansmann, and G. Schönhense, J. Magn. Magn. Mater. **140-144** (1995) 669.

[19] M. Getzlaff, J. Bansmann, and G. Schönhense, Solid. State. Commu. **87** (1993) 467.

[20] E. Kisker, R. Clauberg, and W. Gudat, Rev. Sci. Instrum. **53** (1982) 1137.

[21] J. Manska, M. Dirska, G. Lubinski, M. Schleberger, A. Närmann, and R. Hoekstra, J. Magn. Magn. Mater. **168** (1997) 249.

[22] D.R. Penn, S.P. Apell, and S.M. Girvin, Phys. Rev. Lett. **55** (1985) 518.

[23] E. Kisker, W. Gudat, and K. Schröder, Solid. State. Commu. **44** (1982) 591.

[24] H. Hopster, J. Electr. Spectr. Relat. Phen. **98-99** (1999) 17.

[25] K. Koike and J. Kirschner, J. Phys. D: Appl. Phys. **25** (1992) 1139.

[26] J. Unguris, R.J. Celotta, D.A. Tulchinsky, and D.T. Pierce, J. Magn. Magn. Mater. **198-199** (1999) 396.

[27] D. Sander, A. Enders, C. Schmidthals, D. Reuter, and J. Kirschner, Surf. Sci. **402-404** (1998) 351.

[28] H.J. Elmers and U. Gradmann, Appl. Phys. A **51** (1990) 255.

[29] H.J. Elmers and U. Gradmann, J. Appl. Phys. **64** (1988) 5328.

IX. CONCLUSIONS

Understanding of magnetism on an atomic scale is important from technological and scientific points of view. The use of STM/STS with magnetic tips can resolve magnetic structure on such scale. SP-STM/SP-STS technique was carefully studied during my PhD. And, we succeeded to detect spin-polarized tunneling current. All STM/STS as well as SP-STM/SP-STS measurements were performed in UHV at RT. In this thesis, we found the most reliable and simple method to obtain quantitative information from experimentally obtained SP-STS.

Although an Fe-coated W tip was already used as a SP-STM/SP-STS tip, details of the preparation of the tip depend on each laboratory. Thus, first, we have to find our original preparation method in our setup. Although it took a lot of efforts, finally we found our original method, i.e. tungsten tips with a radius larger than 200 nm coated by 2-10 nm iron films at RT in UHV detect spin-polarized current reproducibly without an application of external magnetic field. We prepared more than 50 different Fe-coated W tips and measured spin-dependency in SP-STS. In this thesis, the SP-STS data which show the highest magnetic contrast are used, which were believed that the tip and the sample magnetization directions are parallel.

As an magnetic sample we chose manganese (001) films grown on Fe(001) at 370 K. The growth, intermixing, geometric, and electronic structure were studied. Then, we used manganese layers thicker than fourth layer to investigate the magnetic structure since these layers consist of pure manganese and have the same geometry and the same electronic structure. On this sample surface, we found that (1) the manganese (001) layers (larger than 1 nm diameter) couples antiferromagnetically with the layers below and above and (2) a spin-dependent LDOS peak above the Fermi energy, which were found to be contributed by highly-polarized two d_{z^2} surface states and one d_{z^2} surface resonance state. Also, the highest lateral magnetic resolution (~0.4 nm) in SP-STS was confirmed.

Then, using our manganese sample and Fe-coated W tips, we found a new method to find quantitative values from experimentally obtained SP-STS, i.e. $(dI/dV)/T$ curves and the asymmetry in $(dI/dV)/T$ were used. Although it was already reported several methods to obtain quantitative values from SP-STS data, we showed these methods include an influence of the spin-dependent tip-sample separation and complications to deduce quantitative values. By recovering spin-resolved sample LDOS, we found that SP-STS detects only surface states and surface resonance states. Bulk states were not detected. This experimentally obtained spin-resolved sample LDOS showed that our tip polarization at the Fermi energy is 18±5 %. Then, experimentally, we obtained that the Mn(001) surface has a 60±16 % polarization at the spin-dependent LDOS peak energy ($P_{Mn}(eV) = A_{(dI/dV)/T}(eV)/P_{tip}(E_F)$).

X. PUBLICATIONS

1. *STM, STS, and Local Work Function Study of Cs/p-GaAs(110),*
T. Yamada, J. Fujii, T. Mizoguchi,
Surface Science, 2001, **479**, 33-42

2. *Photoemission and STM, STS Study of Cs/p-GaAs(110),*
T. Yamada, J. Fujii, T. Mizoguchi,
CP570, SPIN2000, 14th International Spin Physics Symposium (proceeding) 2001, 908-911

3. *Polarization of Secondary Electrons from Clean and Oxygen-Chemisorbed Ni(110),*
Y. Oshima, T. Yamada, J. Fujii, and T. Mizoguchi,
Transactions of the Magnetics Society of Japan, 2001, **1**, 16-21

4. *Direct observation of surface alloying and interface roughening: Growth of Au on Fe(001),*
M.M.J. Bischoff, T. Yamada, A.J. Quinn, R.G.P. van der Kraan, and H. van Kempen,
Physical Review Letters, 2001, **87**, 246102

5. *Scanning tunneling microscopy and spectroscopy study on the submonolayer growth of Mn on Fe(001),*
M.M.J. Bischoff, T. Yamada, A.J. Quinn, and H. van Kempen,
Surface Science, 2002, **501**, 155-167

6. *STM and STS study of ultrathin Mn layers on Fe(001),*
T.K. Yamada, M.M.J. Bischoff, T. Mizoguchi, and H. van Kempen,
Surface Science, 2002, **516**, 179-190

7. *Observation of spin-polarized surface states on ultrathin bct Mn(001) films by spin-polarized scanning tunneling spectroscopy,*
T.K. Yamada, M.M.J. Bischoff, G.M.M. Heijnen, T. Mizoguchi, and H. van Kempen,
Physical Review Letters, 2003, **90**, 056803

8. *Origin of magnetic contrast in spin-polarized scanning tunneling spectroscopy: experiments on ultra-thin Mn films,*
Toyo K. YAMADA, Maarten M.J. BISCHOFF, George M.M. HEIJNEN,Tadashi MIZOGUCHI , and Herman VAN KEMPEN,
Japanese Journal of Applied Physics, 2003, **42**, 4688-4691.

9. *Use of voltage pulses to detect spin-polarized tunneling,*
T.K. Yamada, M.M.J. Bischoff, T. Mizoguchi, and H. van Kempen,
Applied Physics Letters, 2003, **82**, 1437-1439 (Cover image).

10. *Analysis of the short-range order of the Au/Fe(001) surface alloy,*

M.M.J. Bischoff, T.K. Yamada, and H. van Kempen,
Physical Review B, 2003, **67**, 165403.

11. *Local electronic structure of Fe(001) surfaces studied by scanning tunneling spectroscopy*,
M.M.J. Bischoff, T.K. Yamada, C.M. Fang, R.A. de Groot and H. van Kempen,
Physical Review B, 2003, **68**, 045422.

12. *Data evaluation for spin-polarized scanning tunneling spectroscopy measurements*,
T.K. Yamada, A.L. Vazquez de Parga, M.M.J. Bischoff, T. Mizoguchi, and H. van Kempen,
proceeding for the 12th International Conference on Scanning Tunneling Microscopy/Spectroscopy and Related Techniques (STM'03), AIP Conf. Proc. 2003, **696**, 608-614.

13. *Scanning Tunneling Spectroscopy Study of Surface States of 3d Metals: Chemical Identification, Magnetic Contrast and Orbital Kondo Resonance State*,
M.M.J. Bischoff, C.M. Fang, R.A. de Groot, G.M.M. Heijnen, M.I. Katsnelson, O.Yu. Kolesnychenko, R. de Kort, A.I. Lichtenstein, A.J. Quinn, A.L. Vazqeuz de Parga, T.K. Yamada and H. van Kempen,
Acta Physica Polonica A, 2003, **104**, 231-243.

14. *Atomic scale magnetic domain wall: Mn layers on hidden Fe steps*,
T.K. Yamada, A.L. Vazquez de Parga, M.M.J. Bischoff, T. Mizoguchi, and H. van Kempen,
in preparation.

15. *Study of Fe/Mn/Fe(001) multilayers by means of scanning tunneling microscopy/spectroscopy*,
T.K. Yamada, A.L. Vazquez de Parga, M.M.J. Bischoff, T. Mizoguchi, and H. van Kempen,
Surf. Sci., in press.

16. *Magnetism of Fe/Mn/Fe(001) multilayers by means of spin-polarized scanning tunneling spectroscopy*
T.K. Yamada, A.L. Vazquez de Parga, M.M.J. Bischoff, T. Mizoguchi, and H. van Kempen,
in preparation.

17. *Magnetism of Mn layers grown on a hidden Fe screw dislocation: The Tower of Babel*,
T.K. Yamada, A.L. Vazquez de Parga, M.M.J. Bischoff, T. Mizoguchi, and H. van Kempen,
in preparation.

18. *Intermixing, geometric, electronic, and magnetic structures at the interface of*

noble/magnetic-metal films: c(2×2)-AuMn-alloy/Mn(001) by means of STM, STS, and spin-polarized STS,
T.K. Yamada, A.L. Vazquez de Parga, M.M.J. Bischoff, T. Mizoguchi, and H. van Kempen,
in preparation.

XI. CAREER AND DEGREE

Period		Degree
01.04.1988-31.03.1991	Gakushuin Junior High school	
01.04.1991-31.03.1994	Gakushuin High school	
01.04.1994-31.03.1998	Faculty of Science, Gakushuin University	Bachelor 1998
01.04.1998-31.03.2000	Faculty of Science, Gakushuin University Graduate school	Master 2000
01.04.2000-31.03.2003	Faculty of Science, Gakushuin University Graduate school	PhD 2004
01.06.2001-31.03.2004	Solid State Physics 2, NSRIM, University of Nijmegen	PhD 2004

Appendix: Nano-meter scale magnetic domains on Fe(001)-whisker

Figure 50(a) shows an STM image obtained on the Fe(001) surface with an Fe-coated W tip at a set point of $V_S = -0.5$ V, $I = 0.5$ nA (300×300 nm^2). Many steps are observed. Figure 50(b) shows an enlarged image (20×20 nm^2) from Fig. 50(a). Dark spots are observed on the terrace, which concentration is 1 %. Since these dark spots sit at four-fold hollow sites and dI/dV curves of the dark spots show a shift of the +0.2 V peak, these spots are identified as oxygen atoms (Auger spectra showed only oxygen impurities (<1 %) on the surface). All Fe(001) terraces shows the same concentration of oxygen impurities. Here, the step shows a unique structure, which is known to be caused by contaminants [M.M.J. Bischoff, PhD thesis, University of Nijmegen, The Netherlands, 2002, (http://www-evsf2.sci.kun.nl/Doctorate.htm)]. Figure 50(c) shows an $I(V)$ map at +0.2 V obtained with an Fe-coated W tip at the same area as Fig. 50(a) at a set point of $V_S = -0.5$ V, $I = 0.5$ nA. (Here, we used the $I(V)$ map since the steps make a much higher contrast in the dI/dV map.) Four different grey scales are observed, which are marked "1-4" in Figs. 50(a) and 50(c). Since the steps and the contamination-induced structure do not show peaks or shoulders in the spectroscopy, the area "4" appears dark in Fig. 50(b). However, we never observed the contrasts between the Fe(001) terraces ("1-3") with clean W tips. We believe that the contrast between "1-3" are real magnetic contrasts, i.e. close to a step-bunched area many magnetic domains are found to the Fe(001) surface. The areas "1" and "3" show the lowest and the highest contrast on the Fe(001), respectively, which are assumed 180° magnetic domains. dI/dV curves obtained at the areas "1", "3", and "4" are shown in Fig. 50(d). The curve "4" shows a different electronic structure. Since the clean Fe(001) surface has a d_{z^2} surface state at +0.17 eV [see e.g. M.M.J. Bischoff *et al.*, Phys. Rev. B **68** (2003) 045422], curves "1-3" show a peak around +0.2 V. To recover the peak energy position and to remove a spin-dependent tip-sample separation dependence, the dI/dV curves were normalized by fitted tunneling probability functions (T). The $(dI/dV)/T$ curves show a spin-dependent peak at +0.17 V (Fig. 50(e)). By calculating the asymmetry from these $(dI/dV)/T$ curves we can estimate the tip polarization since the Fe(001) surface state is known to be highly polarized. The asymmetry shows a maximum about 20 % at +0.17 V (Fig. 50(f)). Simply, if we assume a 100 % polarization for the Fe(001) surface state, we obtain a 20 % tip polarization at the Fermi level by following Eq. 37. This is close to the value of 18±5 % estimated previously.

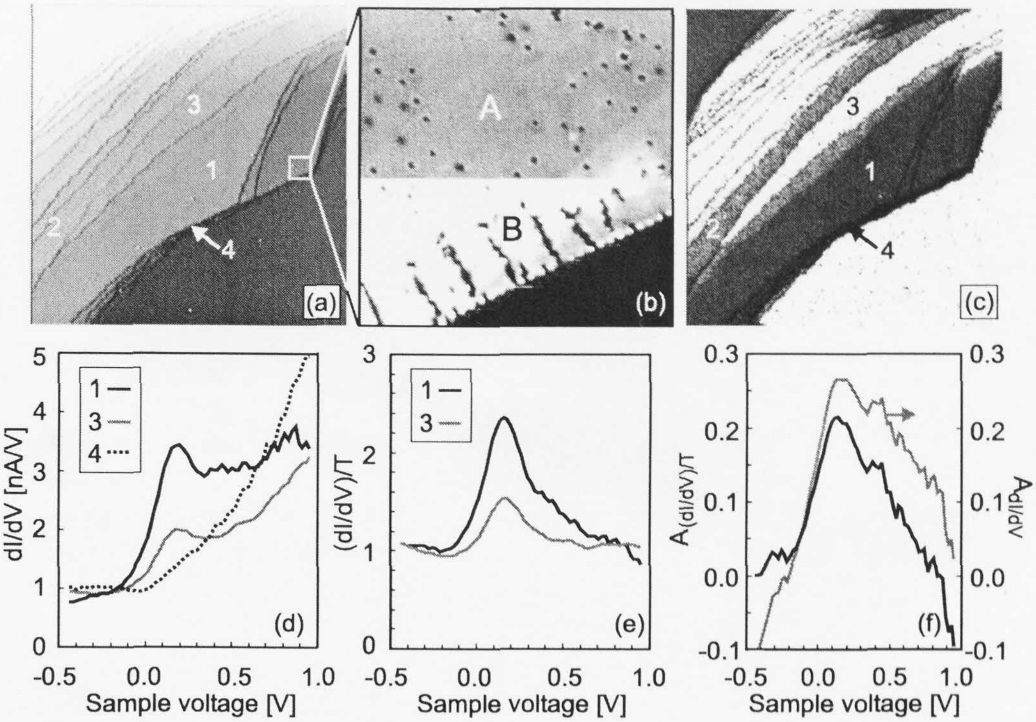

FIG. 50. SP-STM and SP-STS results obtained on the Fe(001)-whisker surface with a magnetic tip. (a) shows an STM image ($V_S = -0.5$ V, $I = 0.5$ nA, 300×300 nm^2). In this area many steps are observed. (b) shows an atomically and chemically resolved STM image obtained on the boxed area in (a) ($V_S = -0.3$ V, $I = 0.2$ nA, 20×20 nm^2). (c) shows a $I(V)$ map at +0.2 V obtained at the same area as (a). Four different grey scales are observed ("1"-"4"). (d) shows dI/dV curves obtained on the area "1" (grey curve), "3" (black curve), and "4" (dashed curve). (e) shows $(dI/dV)/T$ curves obtained at "1" (grey curve) and "3" (black curve). (f) shows an asymmetry of the $(dI/dV)/T$ curves in (e) (black curve) and an asymmetry of the (dI/dV) curves in (d) (grey curve). A maximum value of 0.2 was obtained at +0.17 V for $A_{(dI/dV)/T}$.